# Investigation of Magnetic Interactions in Topological Insulators

by

Mingda Li

B.S., Tsinghua University (2009)

Submitted to the Department of Nuclear Science and Engineering
in partial fulfillment of the requirements for the degree of

Doctor of Philosophy in Nuclear Science and Engineering

at the

MASSACHUSETTS INSTITUTE OF TECHNOLOGY

June 2015



Author .....
Department of Nuclear Science and Engineering
May 1, 2015

Certified by .....
Ju Li
Professor of Nuclear Science and Engineering
Professor of Materials Science and Engineering
Thesis Supervisor

Certified by .....
Paola Cappellaro
Associate Professor of Nuclear Science and Engineering
Thesis Reader

Accepted by .....
Mujid S. Kazimi
TEPCO Professor of Nuclear Engineering
Chair, Department Committee on Graduate Theses

# Investigation of Magnetic Interactions in Topological Insulators

by

Mingda Li

Submitted to the Department of Nuclear Science and Engineering
on May 1, 2015, in partial fulfillment of the
requirements for the degree of
Doctor of Philosophy in Nuclear Science and Engineering

## Abstract

Topological insulators are a category of phases in condensed matter with inverted conduction and valence bands, which is protected by time reversal symmetry. As a result, the bulk keeps insulating while the surface supports an exotic high-mobility spin-polarized electronic states. Introducing magnetism into topological insulators will break the surface time reversal symmetry and alter the spin texture at the surface, and is an essential step to bring topological insulators towards the observation of new quantum states and for device applications.

This thesis is a comprehensive study of magnetic interactions in topological insulators, from both experimental and theoretical perspective. Generically, there are two approaches to bring TI magnetic, the proximity effect and the conventional transitional metal ion doping. In the proximity effect, a layer of magnetic insulator is in proximally contact with a topological insulator, which forms a heterostructure and introduces magnetic exchange with the topological insulator states; while in the transitional metal ion doping, the magnetic dopants will induce magnetic order inside topological insulators. The main content and contribution of this thesis are five-fold. First and foremost, this thesis provides conclusive experimental evidence to demonstrate a long-predicted new type of magnetism, the "Van Vleck ferromagnetism" in magnetic topological insulator Vanadium doped $Sb_2Te_3$. Compared with the traditional RKKY magnetism in diluted magnetic semiconductors which needs undesired free carriers to mediate the magnetism, such magnetism has an carrier-free origin and solves the dark current issue for spintronics applications, such as quantum anomalous Hall effect. Secondly, this thesis provides conclusive experimental evidence to demonstrate the magnetic proximity effect at topological insulator / ferromagnetic insulator interface, where magnetism is penetrated into the side of topological insulator. The main obstacle for this study is the inter-diffusion of magnetic ions to topological insulator, causing false positive signal. This is conquered through experimental means which is capable to resolve the layer-dependent compositional contrast as well as magnetization simultaneously. Thirdly, this thesis discusses a theoretical proposal to show that how to resolve the particular electronic state of topological

insulator participating in the proximity effect. The determination of the magnetized electronic state of topological insulator turns out to be highly difficult for conventional experiments. We utilize the indirect interlayer exchange coupling, i.e. the magnetic coupling between two magnetic layers when a topological insulator is sandwiched in between, to demonstrate the possibility to resolve electronic state in a direct manner. The fourth point, this thesis also discusses a theoretical model to describe a plasmonic device based on topological insulator / superconductor hybrid structure, which has much low energy dissipation compared with metallic plasmon device and might be used to detect Majorana Fermions, an yet-to-be-confirmed particle as building block for quantum computation. Last but not least, combining the merits of high-Curie temperature of magnetic doping and the uniformity of magnetic proximity effect, we also report an enhanced proximity effect based on proximity induced coupling in magnetically doped topological insulator hybrid heterostructure.

Thesis Supervisor: Ju Li
Title: Professor of Nuclear Science and Engineering
Professor of Materials Science and Engineering

Thesis Reader: Paola Cappellaro
Title: Associate Professor of Nuclear Science and Engineering

# Acknowledgments

First and foremost, I would like to express my most sincere gratitude to my thesis advisor, Prof. Ju Li, for giving me an amazingly favorable environment and providing me all kinds of support, mentally and financially, to work on this important project. Prof. Li is great not only because of his deep scientific insights, but also because of his integrity and upright, standing up for me during my few most difficult moments. Prof. Li sharpens my critical thinking and shapes my path and approach for scientific career, which I'll benefit for life long.

I am greatly indebted to all my thesis committee members: Dr. Jagadeesh Moodera, Dr. Yimei Zhu, Prof. Gang Chen, Prof. Liang Fu, Prof. Mehran Kardar and Prof. Paola Cappellaro for their guidance and critical evaluations to my work. In particular, Dr. Jagadeesh Moodera helped me all way along by continuously providing high-quality samples to support my experiments, and it was always delightful discussing with him, as he is like a source of knowledge spring. Dr. Yimei Zhu provided me long term support of the precious experimental resources. I hardly remember how many times I traveled to Brookhaven National Lab by 1am bus, working hard for few days but came back Boston for little progress. It was Dr. Zhu's consistent encouragement and suggestions which guided me to the right track and allowed me acquire beautiful data eventually.

I'm very grateful for all my collaborators, who have provided me pleasant experience of cooperation, without which the work can never be achieved on my own. They are Mr. Wenping Cui from Boston College, Dr. Zuyang Dai from Tsinghua University, Mr. Zhe Wang, Dr. Cuizu Chang and Dr. Ferhat Katmis from MIT, Dr. Lijun Wu and Dr. Jing Tao from Brookhaven National Lab, Dr. Brian Kirby and Dr. Yun Liu from NIST, Dr. Lauter, Dr. Artur Glavic, Dr. Haile Ambaye from ORNL, Dr. Ahmet Alatas, Dr. Bogdan Leu, Dr. Ayman Said, Dr. Ercan Alp, Dr. Michael Hu, Dr. Hua Zhou and Dr. Suzanne G.E. te Velthuis from Argonne National Lab, Prof. Donald Heiman, Ms. Michelle Jamer and Dr. Badih Assaf from Northeastern University, Prof. Moses Chan and Dr. Weiwei Zhao from Penn State University, Prof.

Zhifeng Ren and Dr. Weishu Liu from Houston University.

In addition, I want to thank those people who taught me the essential elements to build up my current scientific understanding. Among them, Dr. Yong Zhang, Prof. Silvija Gradecak, Dr. Shiahn Chen and Dr. Libby Shaw for Microscopies, Dr. Scott Speakman from whom I inherited almost all my knowledge of X-Ray, Prof. Gang Chen and Prof. Karl Berggren for nice introduction of Nanoscience, Prof. Sow-Hsin Chen, Dr. Cheng-Si Tsao, Prof. Xiangqiang Chu, Dr. Yun Liu and Dr. Eugene Mamontov for Neutron and X-Ray Scattering, Prof. Hong Liu, Prof. Roman Jackiw and Prof. Washington Taylor for amazing lectures in Quantum Field Theory, and Prof. Patrick Lee, Prof. Mehran Kardar and Prof. Xiaogang Wen for bringing me into the world of Condensed Matter.

I'm grateful for the strong supports from our NSE department. I'd like to thank Prof. Richard Lester and Prof. Jacopo Buongiorno for the financial support, Prof. Paola Cappellaro, Prof. Linn Hobbs, Prof. Ju Li, Prof. Ian Hutchinson, Prof. Dennis Whyte and Prof Areg Danagoulian and Prof. Bilge Yildiz for the Teaching Assistantship, Ms. Clare Egan, Ms. Rachel Batista, Ms. Heather Barry and Mr. Peter Brenton for solving various administrative problems, and special thanks to Prof. Sidney Yip for the consistent care and encouragement.

I also want to thank a few of my colleagues and group members who have brought me numerous happy memories during my PhD years. They are Mr. Degang Xie, Dr. Suzhi Li, Dr. Yu-Chieh Lo, Dr. Akio Ishii, Mr. Sina Ardakani, Mr. Wenbin Li, Mr. Yang Yang, Dr. Wei-Shan Chiang, Mr. Pei-si Le and Mr. Zhe Wang.

Last but not least, I want to thank all my families supporting me for the decision to pursue a doctorate. In particular, I dedicate this thesis to my beloved wife, Mrs. M. Li, who tells me what life is, and chooses to live a happy life with me together ever after.

# Contents

# List of Figures

# List of Tables

# Chapter 1

# Introduction

## 1.1 Topological Insulators

Topological insulators (TIs), literally speaking, are types of phases which carry certain topological number ("topological"), together with the existence of an energy gap ("insulators"). Based on this literal definition, the Integer Quantum Hall Effect (IQHE), which carries a TKNN topological number (or first Chern number) together with a gap from Landau level [1, 2], or the Quantum Spin Hall (QSH) phase [3], or in the usual sense $Bi_2Se_3$ family of 3D strong topological insulator [4], all fall into the definition of topological insulators, but belong to different categories.

In this regards, a natural questions to ask is that "How many different types of topological insulators are there in nature?" To answer this question, we need to find a decent way to classify the different types of TIs. One widely-adopted way of classification is based on the spatial dimension $d$ as well as three fundamental discrete symmetries[5, 1]: the Time Reversal Symmetry (TRS), Particle-Hole Symmetry (PHS) and Chiral Symmetry (CS). As a result, the different type of TIs are well classified with distinct discrete symmetry properties. Moreover, it simultaneously classifies the topological superconductors as well in addition to TIs. It tends out that there are in total 10 classes of symmetries, which are listed in Table. 1.1 (reproduced from [5, 1]).

In this table, there are three categories, the Wigner-Dyson (W-D, standard), the

| Category | Class | Description | Symmetry | $d$=1 | $d$=2 | $d$=3 |
|---|---|---|---|---|---|---|
| **W-D** | **A** | Unitary | 0, 0, 0 | 0 | $\mathbb{Z}$ | 0 |
| | **AI** | Orthogonal | +1, 0, 0 | 0 | 0 | 0 |
| | **AII** | Symplectic | -1, 0, 0 | 0 | $\mathbb{Z}_2$ | $\mathbb{Z}_2$ |
| **Chiral** | **AIII** | C-unitary | 0, 0, +1 | $\mathbb{Z}$ | 0 | $\mathbb{Z}$ |
| | **BDI** | C-orthogonal | +1,+1,+1 | $\mathbb{Z}$ | 0 | 0 |
| | **CII** | C-symplectic | -1,-1,+1 | $\mathbb{Z}$ | 0 | $\mathbb{Z}_2$ |
| **BdG** | **D** | SC | 0, +1, 0 | $\mathbb{Z}_2$ | $\mathbb{Z}$ | 0 |
| | **C** | Singlet SC | 0, -1, 0 | 0 | $\mathbb{Z}$ | 0 |
| | **DIII** | SC + TRS | -1,+1,+1 | $\mathbb{Z}_2$ | $\mathbb{Z}_2$ | $\mathbb{Z}$ |
| | **CI** | Singlet SC+TRS | +1,-1,+1 | 0 | 0 | $\mathbb{Z}$ |

Table 1.1: The 10 symmetry classes labeling the topological insulators and superconductors. The 3 numbers of symmetry correspond to Time Reversal Symmetry, Particle-Hole Symmetry and Chiral Symmetry, respectively. $d$ is the spatial dimensionality.

Chiral and the Bogoliubov-de Gennes (BdG). The 3 numbers in the "Symmetry" column correspond to the TRS, PHS and CS, respectively. When TRS=0, it means no time-reversal symmetry, while when TRS=+1, it corresponds to integer spin particles, when TRS=-1, it corresponds to half-odd integer spin particles. Similar definition holds for PHS, where PHS=0 means no particle-hole symmetry. A combination of PHS and TRS gives the chiral symmetry, i.e. CS = PHS $\cdot$ TRS. Besides, this table is indeed periodic to dimension with periodicity 8, i.e. dimension $d$ and $d+8$ share the same symmetry category. For practical purpose, we only plot the spatial dimension $d$=1, 2 and 3.

As a few examples of the results from such classification, the IQHE belongs to $d = 2$ class **A**, the QSH belongs to the $d = 2$ class **AII**, while the topological insulator corresponds to the $d = 3$ class **AII**. In addition, the chiral p-wave superconductor belongs to $d = 2$ class **D**, the $d + id$ superconductor belongs to the $d = 2$ class **C**, while the Helium-3 B phase belongs to the $d = 3$ class **DIII** [1, 6, 7, 8].

The above discussion could be regarded as a definition of TI in the broad sense. The TIs in the narrow sense only refer to class **AII** in 2D and 3D (in some situations only referring to 3D in particular), which carries a $\mathbb{Z}_2$ topological invariant. This is so since a large category of realistic materials in the rhombohedral $Bi_2Se_3$ family have

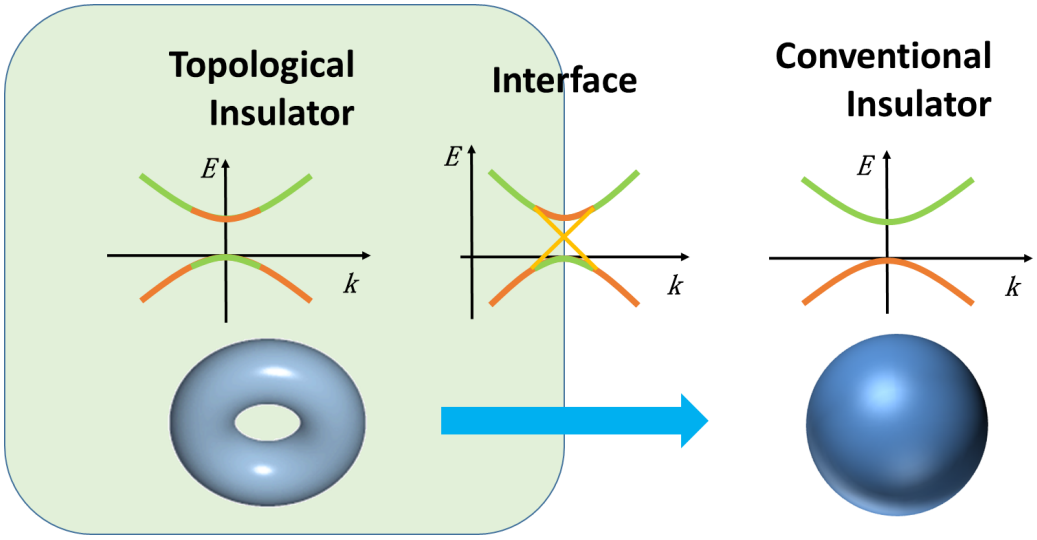


Figure 1-1: Illustration of TI. Comparing with conventional insulator which has the valence (green) and conduction (orange) bands, the bands in TI are inverted. These two insulators carry different magnitude of topological invariant (torus vs sphere). At the boundary, quantum phase transition occurs, where the gap is closed and a gapless surface state emerges.

been proposed and experimentally discovered in recent years [4, 9, 10, 11, 12], contrary with other categories of TIs with very few realization or only theoretical proposals exist. Moreover, such category of TIs have extraordinary electronic properties. For instance, it allows high-mobility Dirac surface electrons on its surface, enabling the possibility for low-dissipation electronic and spintronic device applications [13, 14, 15, 16, 17, 11]. When hybridizing with superconductor structures, the proximity effect might also lead to Majorana zero modes bound to the ends or defects, which could be applied for error-tolerated quantum computation [18, 19, 20, 21, 22].

The classification of TI from the discrete symmetry perspective is very helpful for us to clarify the similarities and differences of different topological phases as a broader definition of TI. However, without observable signature, merely symmetry perspective is not quite helpful to define a TI and demonstrate its striking properties. To gain a visible picture that what a TI really means, we could follow two basic principles. On the one hand, the conduction and valence bands need to be inverted. This can be achieved when the mass of the quasiparticle switches sign, and is a prerequisite for

the existence of gapless boundary states. On the other hand, it requires a symmetry existing to project the boundary state, otherwise the boundary state will not be robust to external perturbation, such as surface passivation. Based on these principles, the desired TI we are interested in can be illustrated as 1-1.

In reality, in the most commonly met $Bi_2Se_3$ family TI, such band inversion is achieved through strong spin-orbit coupling, while the protection of the surface state is realized through Time Reversal Symmetry, which is also the feature coming from the **AII** class with spatial dimension d=3. The corresponding topological number is $\mathbb{Z}_2 = 1$ topological invariant. From now on, the term "Topological Insulator" in this thesis only refers to the $Bi_2Se_3$ family TI, mainly composed of narrow bandgap semiconductors $Bi_2Se_3$, $Bi_2Te_3$ and $Sb_2Te_3$, and the derivate and hybrid structure based on these building blocks. This family of TI have a series of very promising electronic properties, and also obeys the definition of TI when people usually refer to.

## 1.2 Magnetic Proximity Effect and Diluted Magnetic Insulators

The breaking of TRS in TI, which opens up a gap to the helical Dirac surface states in a three-dimensional strong TI, has been shown to be of central importance for both fundamental aspects [23, 24, 25, 26, 27, 28, 1, 29] and device applications [24, 28, 1, 30, 31, 15, 17] in TI studies. For instance the topological magnetoelectric effect [1], which enables the possibility of electric-field controlled spin transistor [15, 32], requires an opening of surface band gap as a prerequisite to reach "off" state, otherwise the gapless surface state would lead to a leakage current and very low on/off ratio. Another promising example is the realization of quantum anomalous Hall effect [33, 34, 35, 36], where gapped surface states are accompanied with backscattering-protected dissipationless edge transport channels without external magnetic field. This opens up the possibility for developing next generation low-dissipation spintronic

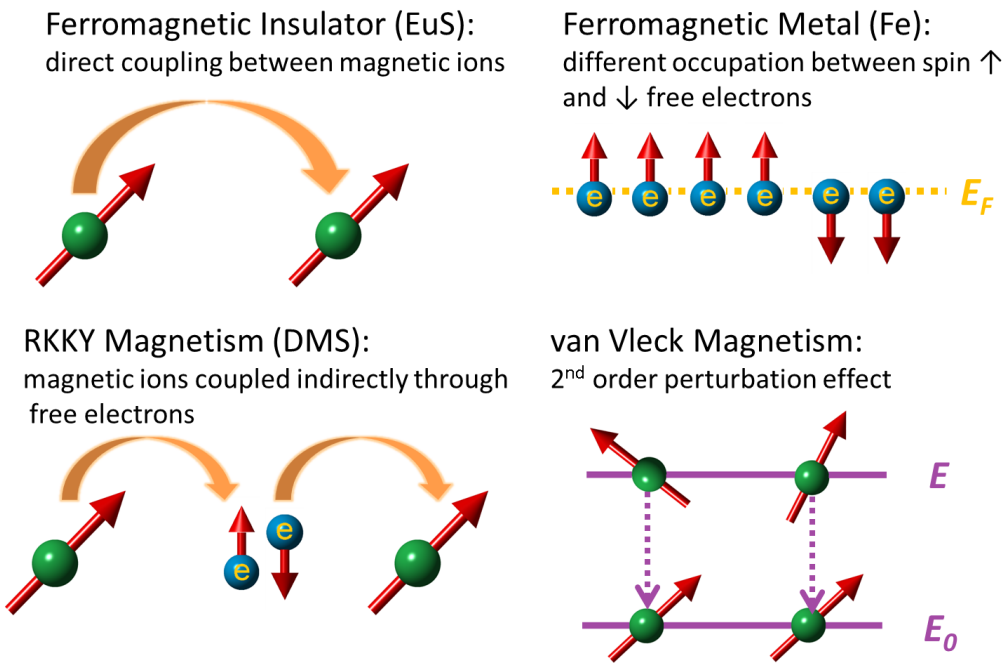


Figure 1-2: Two ways to create magnetic TI: the magnetic proximity effect (a) and transitional metal ion doping (b). In magnetic proximity effect (a), one magnetic layer (in this case, EuS) is in proximity with the layer of TI (in this case, $Bi_2Te_3$ or $Sb_2Te_3$), making TI undergo proximity exchange coupling. In magnetic doping (b), the transitional metal ion (in this case, Cr or V) are doped into TI.

devices. Moreover, domain-wall Majorana bound states are predicted at the TI/FMI interface where magnetization switches sign, which could be applied in error-tolerant topological quantum computation [28, 1, 37]. All the examples above require a gap-opening of the surface states of TI.

Briefly speaking, there are four common types of magnetism, as shown in Fig. 1-2. The first type deals with magnetic insulator, for instance the commonly met magnetite $Fe_3O_4$ or EuS which is studied extensively in this thesis. The second type is magnetic metal, such as Fe or Co. The third type of magnetism happens in diluted magnetic semiconductor (DMS), where magnetic order emerges when the magnetic ions are coupling through the free quasiparticles. The last mechanism is the Van Vleck magnetism, where it is a purely quantum mechanical second-order perturbation effect.

In general, there are two approaches to break the TRS and open up the gap: magnetic proximity effect [30, 34, 38, 39, 40, 41, 42, 43] and magnetic doping [33, 34,

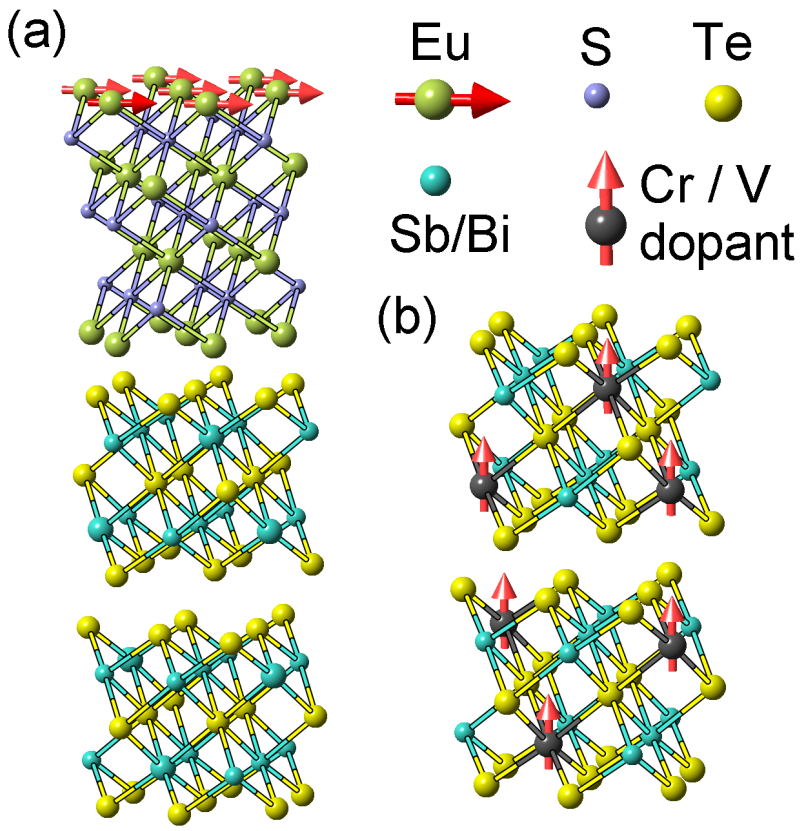


Figure 1-3: Two ways to create magnetic TI: the magnetic proximity effect (a) and transitional metal ion doping (b). In magnetic proximity effect (a), one magnetic layer (in this case, EuS) is in proximity with the layer of TI (in this case, $Bi_2Te_3$ or $Sb_2Te_3$), making TI undergo proximity exchange coupling. In magnetic doping (b), the transitional metal ion (in this case, Cr or V) are doped into TI.

| | Proximity Effect | TM Ion Doping |
|---|---|---|
| Curie Temperature | Low(20K), but for a reason | High(100K) |
| QAHE Realization | ✗not yet | ✓ , 30mK |
| Uniformity | Good | OK; localization |
| Magnetization | Interface | Whole sample |
| Coupling | exchange coupling with f-electron | RKKY / Van Vleck |

Figure 1-4: Comparison between the proximity and the transitional metal ion doping method; both are studied in this thesis.

35, 44] (Fig. 1-3). In magnetic proximity effect (Fig. 1-3(a)), a magnetic layer, usually magnetic insulator (MI) is epitaxially grown on top of TI, making the TI experience exchange coupling; while for the magnetic doping (Fig. 1-3(b)), transitional metal ions are doped inside TI, which forms a magnetic order, meanwhile the TI becomes a Diluted Magnetic Semiconductor (DMS). The former proximity effect is related to the mechanism in first row in Fig. 1-2, while the latter magnetic doping, it is related with the mechanism in the second row. The comparison between these two methods is summarized in Fig. 1-4. From the point of view to bring the surface state of TI magnetic, the two approaches are the same. However, ideally speaking, compared with the doping method, the advantages of the latter include better controllability of the electronic states, uniformly distributed band gap in space, and preservation of the TI's original crystalline structure, etc. Unfortunately, in practice, the magnetic doping method, at least up to now shows better electronic performance [33, 45], mainly thanks to the realization of Quantum Anomalous Hall Effect (QAHE). In any sense, a comprehensive understanding of the interfacial magnetic structure between TI and MI becomes essential for observing QAHE using proximity effect, and push TI for device applications.

## 1.3 Thesis Outline

This thesis is a comprehensive study of the novel experimental phenomena, theoretical methodologies and device applications related with the magnetic TIs. In this thesis, Chapter 2 will begin with an observation of magnetic proximity effect at topological insulator/ferromagnetic(FMI) interface, using depth and element resolved Polarized Neutron Reflectometry (PNR). After exclusion of interdiffusive magnetism, we are able to provide direct evidence of the proximity effect at TI-magnetic heterostructure, and demonstrate a series of interesting features. Most prominently, we observed a temperature-independent proximity magnetism far above Curie temperature, which is identified as a result of topological magnetoelectric effect. To further enhance such proximity effect, we report the magnetic TI / FMI hybrid structure, where proximity effect could be enhanced unprecedentedly strong. These observations answer a few important questions that how to utilize proximity effect for low-dissipation, high-speed spintronic devices at elevated temperature.

In Chapter 3, to further understand the interfacial magnetic structure involved in the proximity effect, we theoretically investigate the interlayer exchange coupling of two ferromagnetic insulators (FMIs) separated by a TI thin film, and demonstrate that the particular electronic states of the TI contributing to the proximity effect can be directly identified through the coupling behavior between two FMIs, together with a tunability of the coupling constant. Such an FMI/TI/FMI structure not only serves as a platform to clarify the magnetic structure of the FMI/TI interface, but also provides insights in designing the magnetic storage devices with ultrafast response.

The complementary approach to proximity effect is the conventional transitional metal ion doping. In traditional diluted magnetic semiconductors (DMS), the dominant magnetic coupling mechanism is the Ruderman-Kittel-Kasuya-Yosida (RKKY) interaction. However, such RKKY interaction is highly undesired for TI's applications. A promising alternate coupling mechanism is van Vleck-type magnetism.

In Chapter 4, through state-of-art low temperature electron energy loss spectroscopy (EELS), we demonstrate that the long range ferromagnetic (FM) order in

Vanadium (V)-doped TI has the nature of van Vleck-type magnetism. The positions and the relative amplitudes of two core-level peaks ($L_3$ and $L_2$) of the V EELS spectrum show unambiguous change when the sample is cooled from room temperature to $T = 10K$. Magnetotransport and comparison of the measured and simulated EELS spectra confirm that these changes originate from onset of FM order. Crystal field analysis indicates that in V-doped $Sb_2Te_3$, partially filled core states contribute to the FM order. Since van Vleck magnetism is a result of summation effect of all states, this magnetization of core level verifies the van Vleck-type FM in a direct manner. This study paves the way to utilize transitional metal ion dopants for applications such as quantum anomalous Hall effect and building blocks for TI-based integrated electronics.

To demonstrate one possibility of TI for device application, in Chapter 5, we theoretically investigate the surface plasmon polariton (SPP) at the interface between a TI and a layered superconductor/magnetic insulator structure, within the random phase approximation. The tunability of the SPP through electronic doping can be enhanced when the magnetic permeability of the layered structure becomes higher. When the interface is gapped by superconductivity or perpendicular magnetism, the SPP dispersion is further distorted, accompanied by a shift of group velocity and penetration depth. Such a shift of the SPP reaches a maximum when the magnitude of the Fermi level approaches the gap value, and may lead to observable effects. The tunable SPP at the interface between layered-superconductor and magnetic materials in proximity to the TI surface may provide new insight in the detection of Majorana fermions.

# Chapter 2

# Magnetic Proximity Effect at Topological Insulator/Ferromagnetic Insulator Interface

## 2.1 Introduction

Magnetic proximity effect in topological insulator (TI) is an effect where the TI states near the interface are magnetized through exchange coupling with magnetic layers in close proximity [17, 40, 29, 27, 1, 28, 38]. It provides a controlled approach to open up the bandgap of the Dirac surface states of TI uniformly, and leads to a number of promising applications, including the quantum anomalous Hall effect [27, 28, 13, 36, 46, 35], electrically controlled spintronics devices with ultrafast response [17, 40, 47, 14, 30, 48], and serves as a basis for error-tolerated topological quantum computation at the domain wall [27, 1, 28]. Despite of the thriving theoretical studies to discuss the properties of the proximity effect [40, 29, 27, 28, 25, 23], most of the experimental evidences are yet to be straightforward. For instance, magneto-optical Kerr effect (MOKE) [30] only measures the total Faraday angle without depth resolution, hence proximity effect using MOKE has to be confirmed indirectly by comparing with a control sample. While ARPES is powerful to study the surface

electronic structure in TI [13], it is not applicable to study TI when FMI is epitaxially grown the top, due to short-range escape depth ( 1nm) of photoelectrons [14]. In short, conclusive experimental evidence demonstrating the existence of such magnetic proximity effect is highly desired.

In this Chapter, we report the magnetic proximity effect near the interface between TI $Bi_2Se_3$ and ferromagnetic insulator (FMI) EuS, using the depth and composition resolved polarized neutron reflectometry (PNR). We find that the magnetization penetrates through $\sim$1 quintuple layer (QL) into $Bi_2Se_3$, with the total magnetization across this QL as large as $4\mu_B$ at 5K. The reason to choose Eu-based FMI not only lies in the largest magnetic moment of $Eu^{2+}$ ion ($\sim 7.9\mu_B$/ion), but also due to Eu's one of the largest thermal neutron absorption cross section (4530 barn) in the periodic table [49]. Thus, the absence of absorption feature in TI near the interface directly excludes the possibility that the magnetization comes from magnetic $Eu^{2+}$ ions interdiffused into TI region. Furthermore, contrary to the traditional view that proximity effect only exists below the Curie temperature of FMI, as shown in magnetically doped TI [36, 44, 33], here when temperature is raised up to 50K, far above the Curie temperature of EuS $T_c$=16.6K, the proximity magnetism still persists ($\sim 1\mu_B$/QL), with slightly shrunk penetration depth into TI. We show that this protection might be a direct consequence of topological magnetoelectric effect [27, 28], where the interfacial polarization and charge transfer leads to an effective magnetic field perpendicular to the TI/FM interface.

In order to enhanced the proximity effect, i.e. proximity layer induced magnetism in TI, in addition to the usual heterostructure (Fig. 1-3(a)),we propose a hybrid heterostructure based on FMI / magnetically doped TI, as illustrated in Fig. 2-1(a) which is an example composed of EuS/ V-doped $Bi_2Te_3$ heterostructure. In this structure, the easy axis of EuS and V-doped TI are in-plane and out-of-plane, respectively, leading to a complex magnetic interaction of the Eu ions near the interface (Fig. 2-1(b)). They are Heisenberg ferromagnetic or anti-ferromagnetic exchange coupling with other Eu ions in the same lattice plane (yellow-colored spin), the superexchange coupling with Eu ions in different planes mediated by S ions (green-colored spin), the

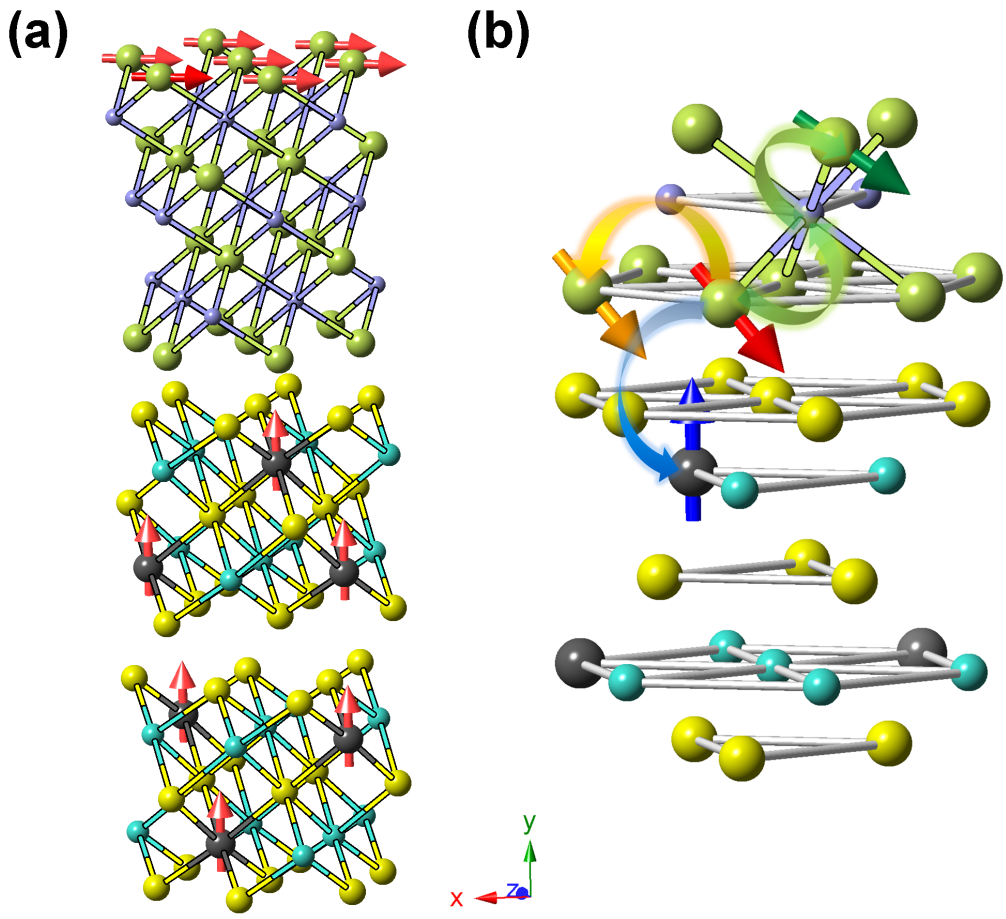


Figure 2-1: (a)hybrid heterostructure EuS / V-doped $Bi_2Te_3$. The spins of magnetic ions Eu (green) and V (grey) are labeled as red arrows. (b) In this structure, the interaction is quite complicated, that the Eu ion (in red) may experience Heisenberg interaction (yellow), super-exchange interaction (green), $d-f$ hybridizing exchange (blue), and interaction with the surface states of topological insulator.

interaction with surface states of TI and the $d-f$ hybridizing exchange to the V-dopants inside the TI. Such magnetic environment, especially the added interaction from magnetic dopants, has been shown to have huge influence to the enhancement of proximity magnetic coupling, even at small doping level. This could be understood that despite of the low doping level, as long as it is in FM state, the whole surface states of TI are magnetized with emergence of surface spin texture, which could strongly interact with the interfacial Eu ions.

## 2.2 Experimental Description of Polarized Neutron Reflectometry

High-quality TI/FMI heterostructure samples and magnetic TI/FMI hybrid heterostructures are grown using molecular beam epitaxy under $\sim 10^{-10}$torr ultrahigh vacuum, where thin film $Bi_2Se_3$ (0001) is grown on top of sapphire (0001) substrate, with FMI EuS (111) layer grown *in situ* above TI film with electron beam source. A capping layer of amorphous $Al_2O_3$ <10nm is deposited on the top for protection. In order to study the size effect of TI and FMI, we measured three TI/FMI samples, two of which have different thicknesses (7QL and 10QL) of $Bi_2Se_3$, but keeping EuS fixed as 5nm, and a third sample with 20QL $Bi_2Se_3$ but only 2nm of EuS. We find that neither the TI thickness nor the cooling history has observable effects to the proximity effect, at least when TI layer is thick enough to avoid interlayer hybridization. However, the proximity magnetism reduces when FMI layer becomes thinner. This seems conflict with the fact that proximity effect only involves the topmost layer of FMI [50, 51, 52, 53] thus thickness independent, but can be understood since the magnetic structure itself near the interface could be thickness-dependent [54, 55]. In addition, we measured another three magnetic TI/FMI samples, the 15 quintuple layer magnetic TI V-doped $Sb_2Te_3$ and 15 quintuple layer TI pure $Sb_2Te_3$ + 5nm EuS control sample, and one sample 15 quintuple layer magnetic TI V-doped $Sb_2Te_3$ + EuS where the proximity exchange coupling becomes most prominent.

The PNR measurements were carried out at Spallation Neutron Source, Oak Ridge National Laboratory (SNS, ORNL)[56] and Center of Neutron Researches in National Institute of Standard Technology (CNR, NIST). Fig. 2-2(a) shows a schematic of PNR experiment along with the sample configuration. Incident polarized neutrons (spin+) are reflected by the FMI/TI layered structure, with both spin components collected (Fig. 2-2(b), red and blue). An in-plane guiding field H=1T is always exerted on the sample to aid the alignment in FM phase, but has negligible impact to PNR signal when it is paramagnetic (see in Eq. 2.1). The fitting and refinement of PNR is performed using GenX program [57], from which the depth-dependent in-

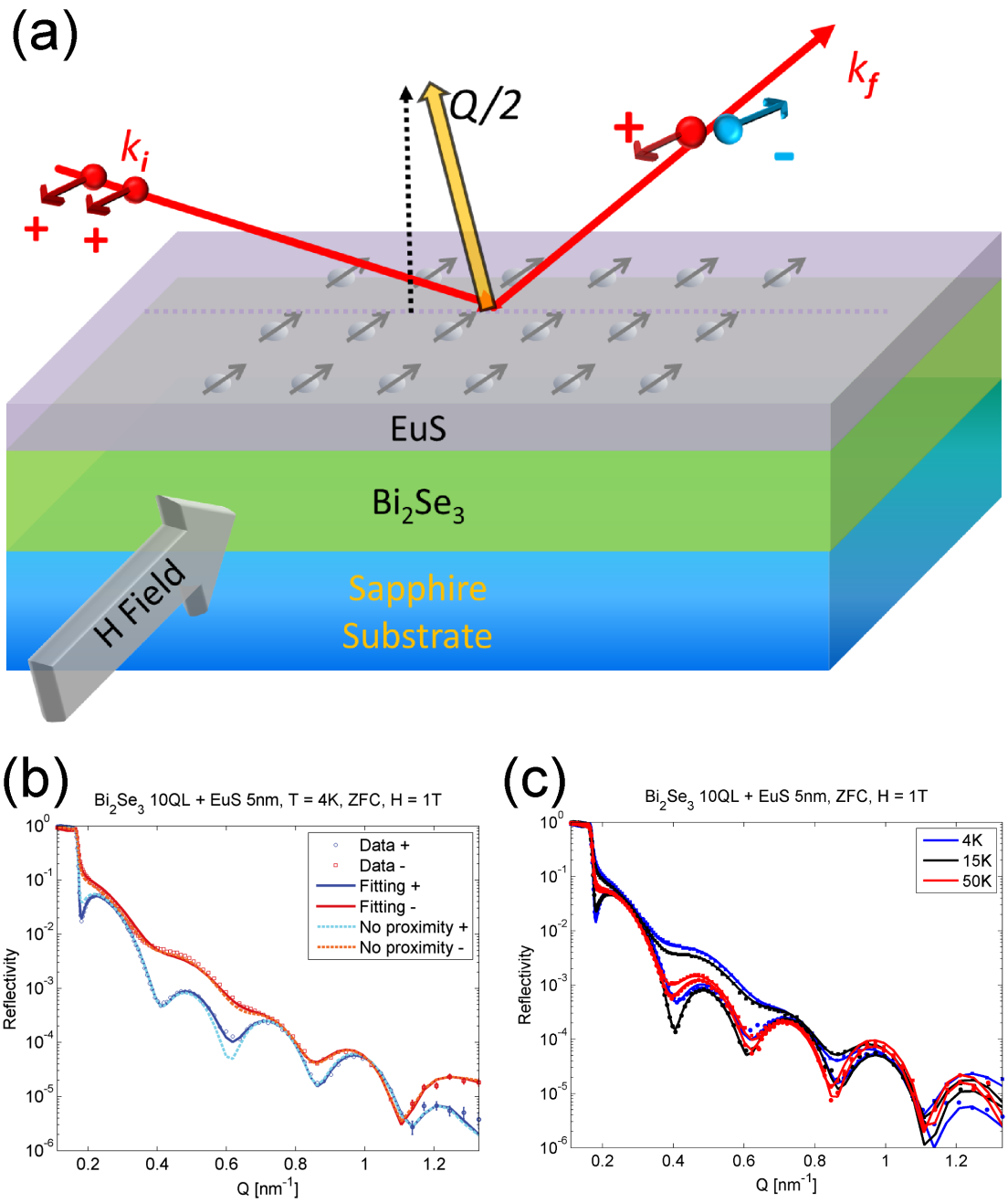


Figure 2-2: The configuration of PNR (a) and typical measured spectra (b, c). In (a), spin + neutrons with wavevector ki are reflected by the TI/FMI heterostructure, and both spin + and spin- neutrons with wavevector kf are collected by position-sensitive detector. The sensitivity of PNR fitting is illustrated in (b). The optimized fitting with zero proximity effect leads to inconsistence between experimental data (blue dot) and fitted curve (azure dashed line), indicating the robustness of the PNR fitting (red and blue solid lines). In (c), spin + and spin- are plotted using same color to emphasize the temperature dependence.

plane magnetization can be resolved. The sensitivity of PNR to proximity effect is shown in Fig. 2-2(b), that when forcibly setting proximity magnetism in TI to be zero, the best-fitting results (azure and orange) cannot reach good agreement with experimental data (see the gap $\sim 0.6\text{nm}^{-1}$). All samples are measured at 5K, 15K and 50K (Fig. 2-2(c)). The reflectivity of spin+ and spin- components at 50K (red curves in Fig. 2-2(c)) do not overlap completely, indicating the existence of magnetic structure, before doing the PNR fitting.

## 2.3 Results and Discussions

### 2.3.1 Proximity Effect

The profiles of various neutron scattering length density (SLD) obtained from PNR fitting, including nuclear SLD (NLSD), magnetic SLD (MSLD) and absorption SLD (ASLD), are shown in Fig. 2-3 as a function of height above the substrate. The substrate lies in the region below 0nm. NSLD denotes the compositional contrast, where the NSLDs for each compound layer are correctly reproduced from PNR fitting (sapphire substrate $5.7\times10^{-4}/\text{nm}^2$, $Bi_2Se_3$ $2.83\times10^{-4}/\text{nm}^2$, EuS $1.88\times10^{-4}/\text{nm}^2$ and amorphous $Al_2O_3$ $\sim 4\times10^{-4}/\text{nm}^2$, which further validates the fitting quality. The MSLD (blue curves) are plotted at 5K, 15K and 50K, respectively, under zero field cooling (ZFC). We see clearly that there is a penetration of magnetization into $Bi_2Se_3$. However, unlike the EuS region where strong ALSD caused by Eu elements is always accompanied, the magnetization into $Bi_2Se_3$ does not show any absorption (~9-10nm in Fig. 2), indicating that such magnetism in $Bi_2Se_3$is not from ferromagnetic Eu ions interdiffused into $Bi_2Se_3$, but from proximity effect.

What's more, the history of cooling does not affect the proximity magnetism, where field cooling (FC) at 1T (black curve) overlaps with the ZFC. This is also reasonable since the proximity is an effect intrinsic to TI instead of extrinsic to FMI cooling history. The survival of proximity effect in TI is accompanied by a persistence of ferromagnetism of EuS at 50K. If the magnetization of EuS is solely from the

external field, from Weiss molecular field theory, we could estimate the magnetization of EuS ( in $\mu_B$/ $Eu^{2+}$ion) as [58, 59].

$$\begin{aligned} \tilde{M} &= gJB_J(x) \\ &= gJ\left[\tfrac{2J+1}{2J}\coth\left(\tfrac{2J+1}{2J}x\right) - \tfrac{1}{2J}\coth\left(\tfrac{x}{2J}\right)\right] \end{aligned} \tag{2.1}$$

where for $Eu^{2+}$ the Landé factor $g$=2 [60], total angular momentum J=7/2 [61], $B_J(x)$ is the Brillouin function with $x \equiv gJ\mu_B(H + \alpha M)/k_BT$, wtih $H$ is the external field and $\alpha$ is Weiss molecular field constant. For $T > T_c$, we have $\alpha = 0$ by definition of ferromagnetism, thus the magnetization caused by $H$=1T at 50K is $\tilde{M} \simeq 0.04M_s$, only 4% of the saturated magnetization and much smaller than the ~10% experimental observed magnetism.

### 2.3.2 The Presence of Proximity Effect at Elevated Temperature

To further understand such persistent magnetization and the interplay between proximity magnetism in TI and ferromagnetism in FMI, we compare the magnetization in each region as a function of temperature (Fig. 2-4). Fig. 2-4(a) is the total magnetization penetrating through the TI layer (the integrated area of ∼9-10nm in Fig. 2-3), normalized with the thickness of 1QL=0.96nm. The errorbar mainly comes from the interfacial roughness of the fitting. We see that the sample with thinner (2nm) EuS layer has weaker magnetization to TI compared with thicker (5nm) EuS layers, but the proximity magnetism seems disappear at ∼75K through extrapolation to a convex function. On the contrary, the averaged magnetic moment per $Eu^{2+}$ ion in the main region of FMI layer (∼12-15nm in Fig. 2-3) disappears at lower temperature ∼60K. Therefore, the magnetization in main EuS region seems not correlated with proximity magnetism of $Bi_2Se_3$. On the other hand, the first few layers of EuS near the interface (∼10-12nm in Fig. 2-4) show reduced in-plane magnetic moments, allowing us to plot the magnetization for only the topmost few EuS layers (Fig. 2-4(c)), and correlate only this portion of magnetism in EuS to the proximity effect.

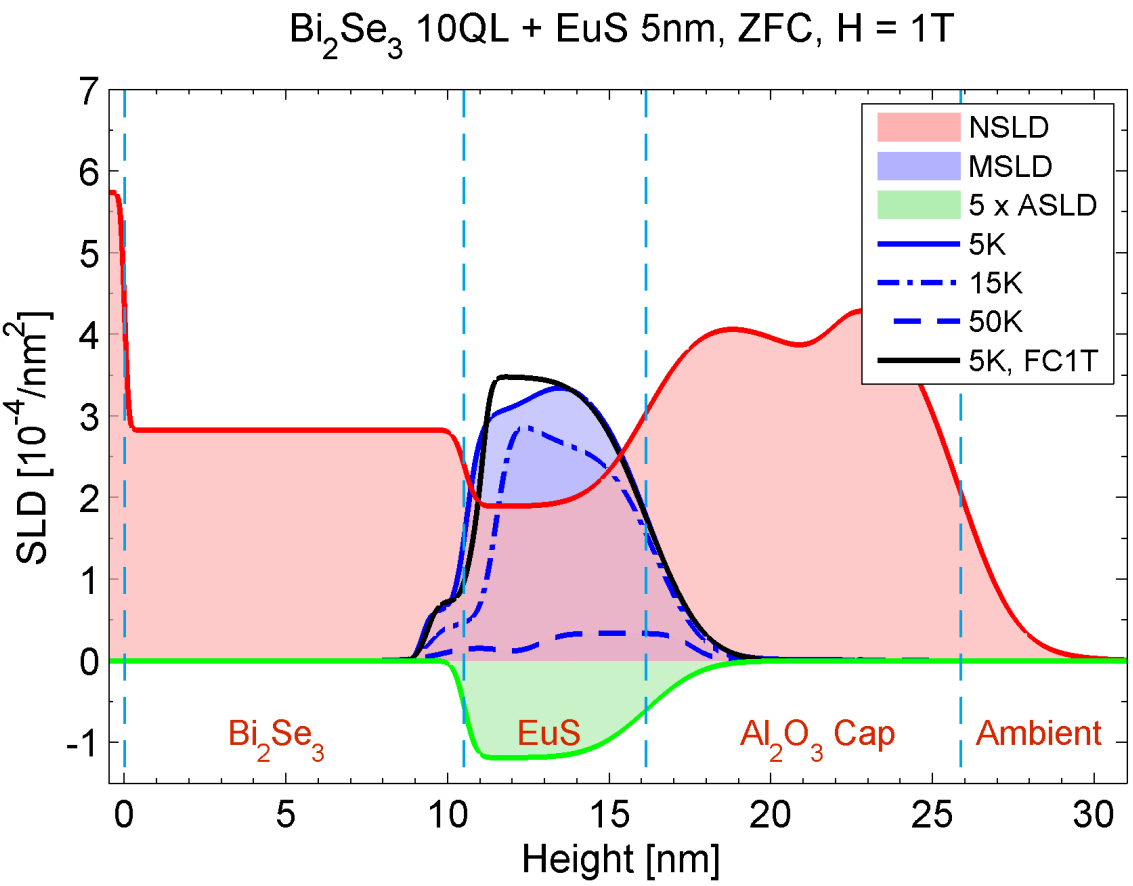


Figure 2-3: Profile of neutron scattering length density (SLD) as a function of height above the substrate. The red, blue and green areas correspond to Nuclear SLD (NSLD), Magnetic SLD (MSLD) and 5 times of Absorption SLD (ASLD), respectively. The magnetic proximity effect is revealed as the MSLD signal in TI side, without ASLD caused by ferromagnetic Eu ions. Such proximity effect exists at 50K, far above the 16.6 K Curie temperatures of EuS.

The ratio of total magnetization between topmost few layers of FMI and TI is plotted in Fig. 2-4(d), which can be regarded an indication of exchange coupling strength. This can be understood since $M_{//}(TI)/M_{\perp}(EuS)$is the true quantity to represent the coupling strength, but PNR only measures the in-plane magnetic moments. By assuming that $M_{\perp}(EuS)$ and $M_{//}(EuS)$are always complementary at each fixed temperature, we could use the reciprocal $M_{//}$(EuS)/$M_{//}$(TI) as a measure of coupling strength of proximity effect.

Due to short-range nature of exchange coupling, we infer that only the topmost EuS layers near the interface contribute to the proximity magnetism. This is corrob-

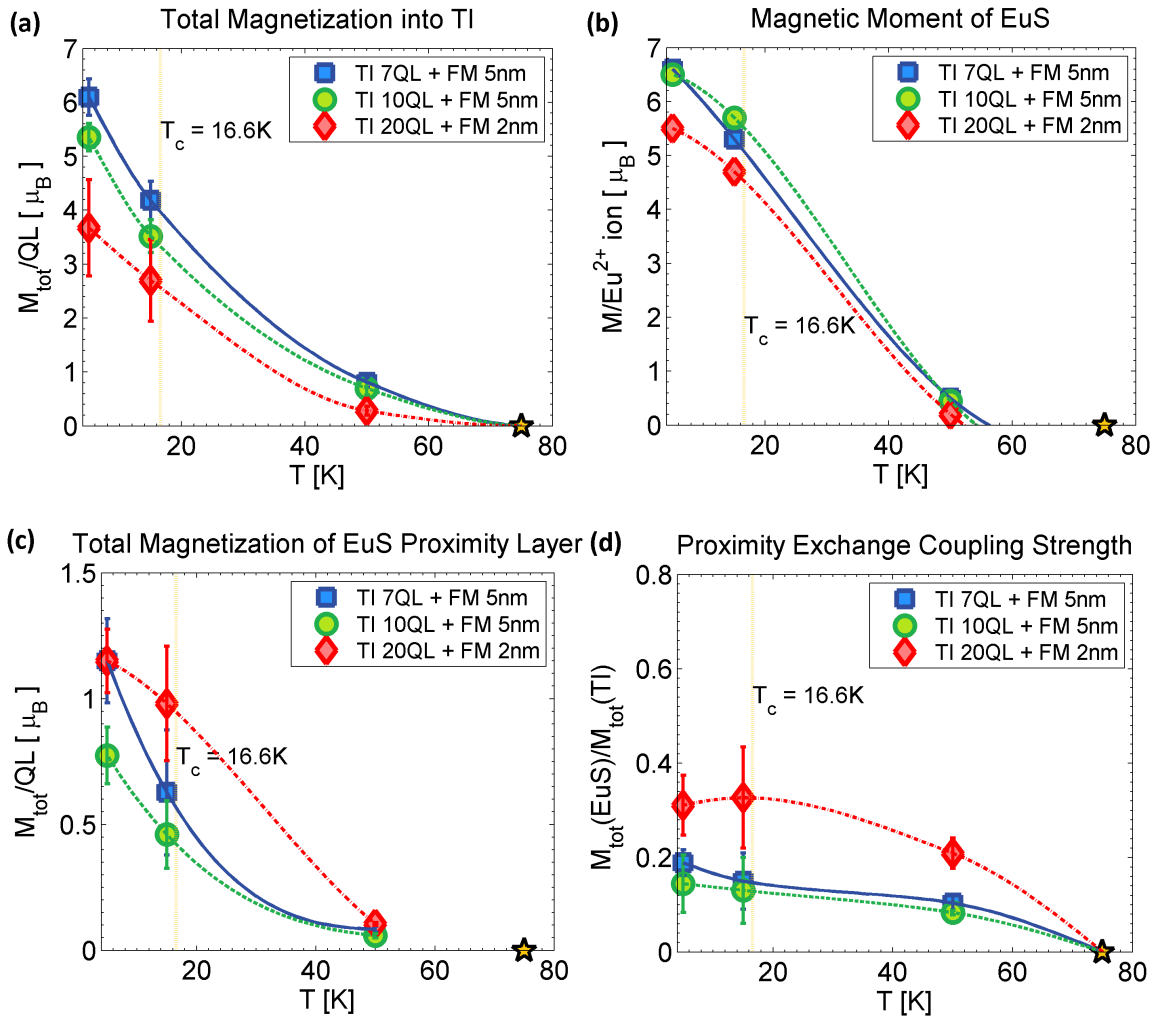


Figure 2-4: (a) The total magnetization into TI. Extrapolation shows that the magnetization disappears completely at ∼75K, which is highlighted as star. (b) The average magnetic moment per Eu ion in the FMI. (c) The total magnetization for topmost EuS layers near the interface with reduced magnetization. (d) The magnetization ratio between the EuS layers in proximity with the interface and the TI layers, indicating that the thinner FMI layer (∼2nm) leads to a stronger proximity exchange coupling.

orated by noticing that the 7QL and 10 QL samples have almost identical coupling strengths, at all temperatures. This is physically reasonable, that the proximity coupling strength, unlike magnetization, should be intrinsic and independent of temperature. Actually, if the coupling between FMI and TI is written by a simplified coupling Hamiltonian [62],

$$H_{\text{int}} = \sqrt{\hbar\gamma/\pi} \sum_{\mathbf{p},\mathbf{q}} \sum_{\alpha,\beta} \hat{a}^{+}_{\mathbf{p}\alpha} \hat{b}_{\mathbf{q}\beta} \tag{2.2}$$

where the $\hat{a}^{+}_{\mathbf{p},\alpha}$ and $\hat{b}_{\mathbf{q},\beta}$ creates and annihilates a state in TI and FMI, respectively, the ratio of magnetization plotted in Fig. 2-4(d) performs a similar role as the coupling constant $\gamma$ in Eq. 2.2, which is expected to be T-independent.

What's more, despite the weaker magnitude of induced proximity magnetism to TI, the 2nm FMI sample has stronger coupling strength (red line, Fig. 2-4(d)). This indicates that despite the proximity coupling is intrinsic to TI for one sample, it should be dependent on the magnetic structure of FMI close to the interface, i.e. coupling constant $\gamma$ is sample dependent.

We now show that the topological magneto effect, where magnetic field and electric field are coupled though an axion term [27, 24, 63], may provide a possible mechanism for the protection of magnetism. At the polar interface of $Bi_2Se_3$/EuS, the electric field caused by polarization can be written as $E = en_0/\varepsilon_0\varepsilon_{\text{eff}}$, where the surface carrier density $n_0$ is $\sim 10^{13}/\text{cm}^2$ [64, 65] in $n$-doped $Bi_2Se_3$ sample, $\varepsilon_{\text{eff}}$is the effective dielectric constant near the interface. The magnetoelectric effect can be described by axion electrodynamics [63] as

$$c_0\vec{H} = \frac{c_0\vec{B}}{\mu} + \alpha\frac{\vec{E}}{\mu_0} \tag{2.3}$$

Therefore, the internal magnetic field induced by electric field (assuming $\varepsilon_{eff} \sim 50$) could be as huge as $10^{-3}$T. The Weiss molecular field constant can be calculated as $\lambda = 3k_{\text{B}}T_c/\mu_0 NJ(J+1)g^2\mu_{\text{B}}^2$ [59, 66], which gives $\lambda = 4.8$ for EuS. Hence, the magnetoelectric coupling finally provides a strong out-of-plane internal magnetic field $\mu_0 H \sim 5\times10^{-3}$T. Despite small magnitude compared with external in-plane magnetic field, such out-of-plane magnetic field serves as the driving force to split the near-surface bands and generate strong in-plane magnetic texture such as Rashba-split states [67], and contribute to the PNR signal. In addition, this picture explains the reason why the 2nm EuS sample shows a stronger coupling strength. The $\varepsilon_{eff}$ near the interface is smaller for thinner FMI sample, resulting in a larger interfacial electric

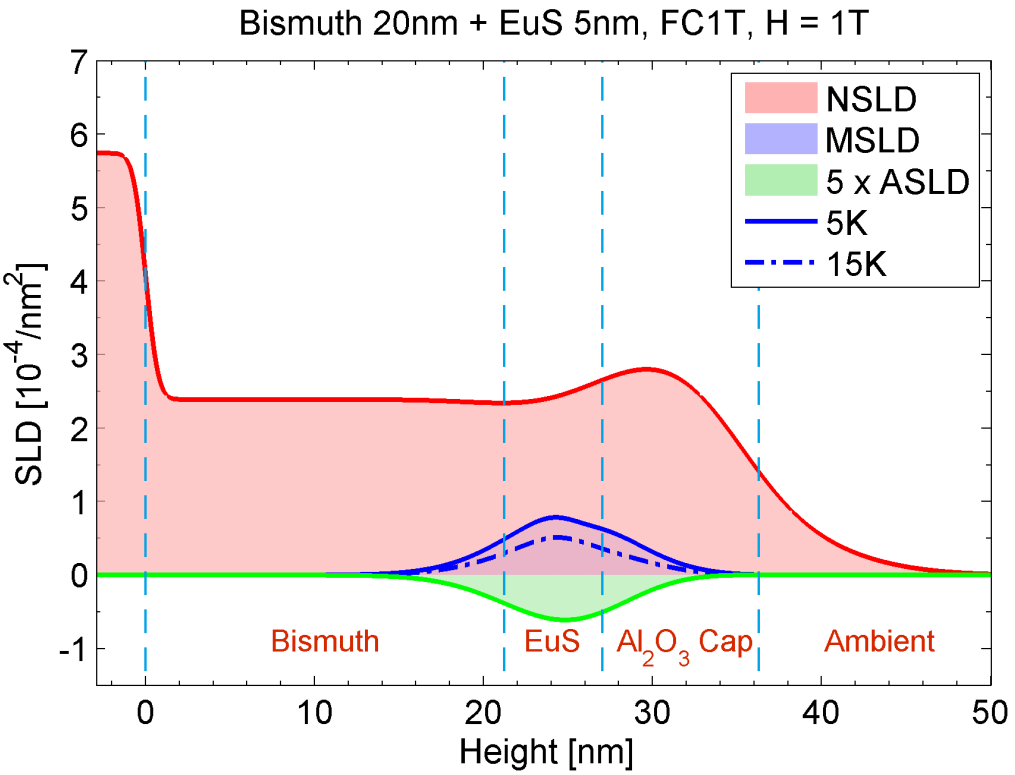


Figure 2-5: The profile of neutron SLDs for pure Bi/EuS control sample. There is no sign of proximity magnetism, indicating that the topological surface state in TI contributes to proximity. However, it is also possible that the effect is smeared by the large interdiffusion of Eu ions, or simply a lack of free carriers in semiconducting Bi films.

field hence stronger proximity coupling.

In order to study the origin of the proximity magnetism, that whether it is from topological surface states in TI or other states near the interface, we measure a control sample of 20nm pure Bi / 5nm EuS (Fig. 2-5). Rashba-split surface states are expected in this sample due to strong spin-orbit coupling of Bi, but not topological Dirac surface state. There is no signature of proximity effect, but it is probably caused by the lack of free carriers, since Bi undergoes a semimetal-semiconductor transition below a threshold thickness of $\sim$ 28nm [68]. What's worse, due to the non-epitaxial nature of the film growth, the Eu ions heavily interdiffused into Bi region, and the possible formation of $Eu^{3+}$ compounds which reduces the magnetization in EuS (blue curves in Fig. 2-5), the result is not as convincing as the case of $Bi_2Se_3$ films.

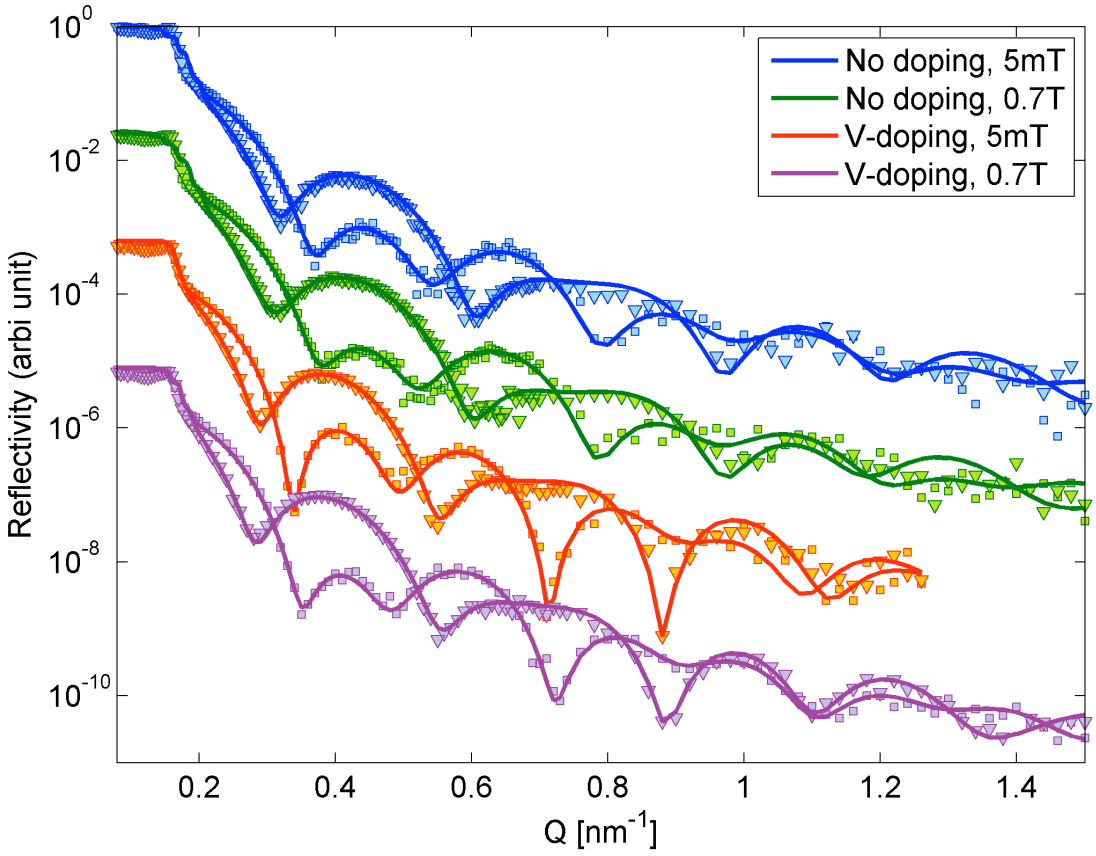


Figure 2-6: The polarized neutron reflectometry results of reflectivity for 15 nm $Sb_2Te_3$ / 5nm EuS heterostructure, with and without magnetic doping of Vanadium dopants. The measurement is performed at 5K, far below the Curie temperature of EuS $T_c$ = 16.6K.

### 2.3.3 Enhancement of Proximity Effect In Hybrid Heterostructures

To further enhance the strength of proximity effect, we could utilize the magnetic TI/ FMI hybrid heterostructure as illustrated in Fig. 2-1). The measurements are performed using PNR at high (0.7T) and low (5mT) field, with the presence of V-dopants or not. The fitting result is shown in Fig. 2-6. No matter at high field (green and purple curves) or low field (blue and orange curves), the presence of Vanadium dopants greatly changes the picture of magnetic structure, which can even be seen from different reciprocal periodicities. Moreover, without V-doping, the reflectivity curves are similar at low field (blue) and high field (green), indicating a saturation

behavior of magnetization of EuS. On the contrary, the large difference of the low field (orange) and high field (purple) curves with V-dopants indicates that the presence of V-dopants will greatly change the magnetic structure, especially the saturation behavior of EuS. This is indeed the case, as shown in the fitting result Fig. 2-7).

We see clearly that despite of the small V-doping level (0.1 in this case), the magnetization of EuS near the interface is reduced dramatically. This is consistent with the result from Fig. 2-6), where V-dopants will have huge influence to the reflectivity curves even without the fitting. Meanwhile, the proximity effect, revealed as a magnetization bump in the side of TI, is becoming more apparent. This is indeed consistent with the fact the drop of interfacial in-plane Eu magnetization indicates an increase of out-of-plane moment of Eu ions, which are responsible for proximity effect and the in-plane spin texture in TI.

To verify that such variation of magnetic structure of EuS near the interface is real, we performed an independent measurement of magnetic hysteresis loops using Physical Property Measurement System (PPMS) (Fig. 2-8), at various reset field. We see that although the coercivity is kept as constant (green squares), there is a bias field developed (blue stars). This indicates some coupling between an anti-ferromagnetic structure and a ferromagnetic structure. Since we know (see in Chapter 4) that V-doped TI is always ferromagnetic, such phenomena indicates that there is some possibility to develop antiferromagnetic structure of EuS near the interface with TI. This antiferromagnetism reduces the magnetization, and is quite consistent with Fig. 2-7.

## 2.4 Chapter Conclusions

To summarize, we provide a depth-sensitive evidence to show the emergence of magnetic proximity effect in $Bi_2Se_3$/EuS heterostructures by PNR, where the proximity coupling strength and penetration depth of magnetism into TI are extracted. The large neutron absorption of Eu elements enables us to recognize such magnetism in TI as proximity magnetism, instead of ferromagnetic $Eu^{2+}$ ions. This provides a

complementary approach to understand proximity effect in TI, in addition to magnetotransport or MOKE. Moreover, we observed a survival of the proximity effect above the Curie temperature of EuS layer, which may be explained by topological magnetoelectric effect. The magnetism emerges from interfacial polarization and is temperature insensitive. This "topological-protected magnetism" opens up a new approach to preserve the proximity magnetism at elevated temperature, leading to wide applications in TI-based next generation spintronic devices.

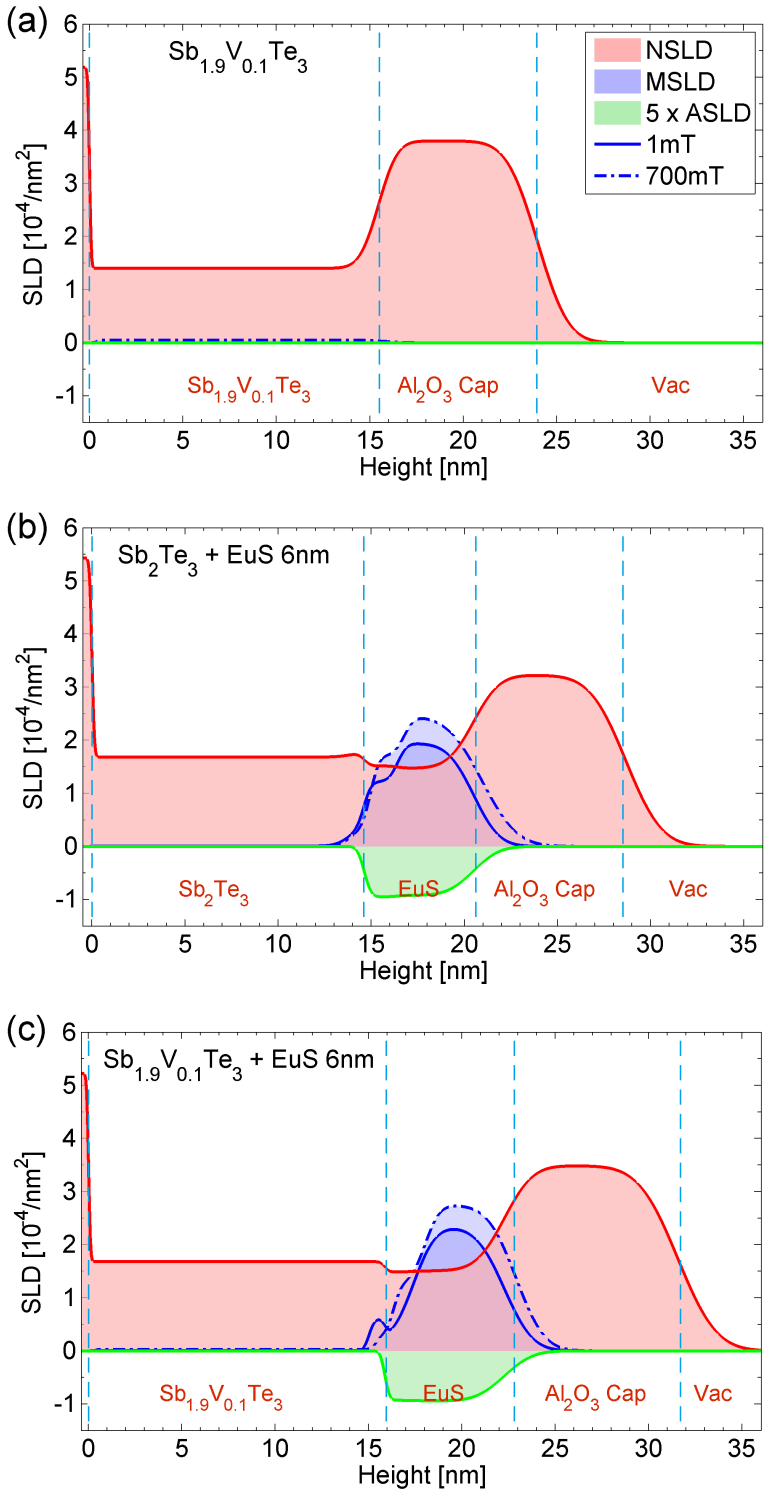


Figure 2-7: The polarized neutron reflectometry fitting results of scattering length density. NSLD, MSLD and ASLD denote Nuclear Scattering Length Density (compositional contrast), Magnetic Scattering Length Density (proportional to magnetization) and Absorption Scattering Length Density (caused solely by Eu elements for thermal neutron absorption), respectively.

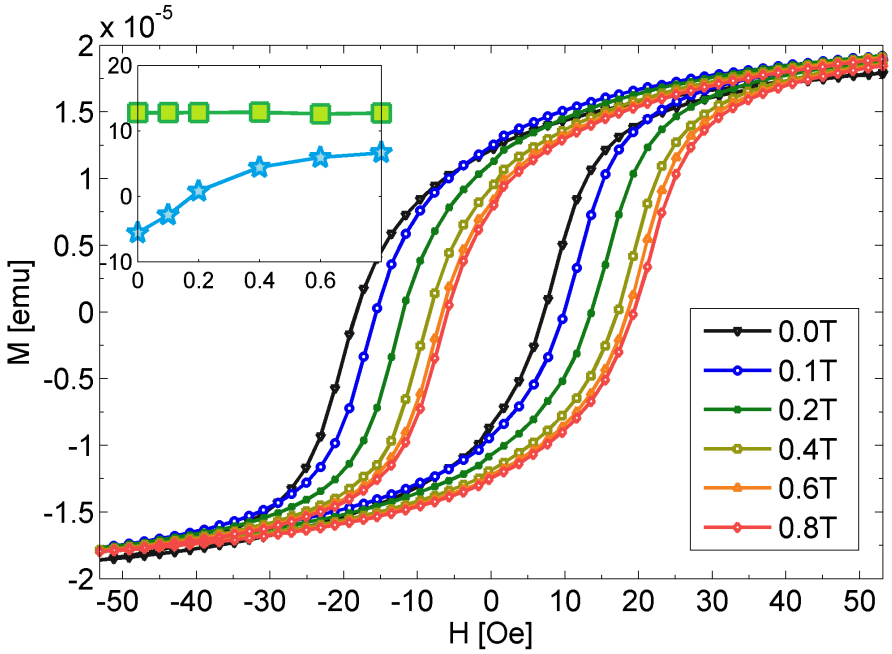


Figure 2-8: The magnetic hysteresis loop M(H) at various reset fields. Before each measurement, a H=-1T negative saturating field is applied to avoid any mixture, then a reset field with indicated magnitude is applied. The green squares and blue stars indicates coercivity and bias field, respectively.

# Chapter 3

# Interlayer Exchange Coupling of Magnetic Insulator / Topological Insulator / Magnetic Insulator Trilayer As A Probe For Electronic State Determination

## 3.1 Introduction to Interlayer Exchange Coupling

Despite the experimental proof in Chapter 2 about the existence of proximity exchange coupling, a complete determination of the magnetic structure between TI and FMI turns out to be nontrivial. In other words, we need more information to determine which particular electronic state could participate into this proximity effect. The difficulties are at least two folds. On the one hand, the interaction between the TI and FMI states is self-consistent in nature, where TI states can lead to complex spin structure, such as magnetic precession in FMI [69], or other spin transfer torque which modifies the spin texture neat the interface. On the other hand, the extraction of such interfacial information is also hindered by the insufficient experimental

capabilities for a comprehensive understanding. For instance, despite the powerful technique of spin-resolved ARPES to study surface electronic and magnetic structure of doped TI [13], due to the small ($\sim 1\,\mathrm{nm}$) escape depth of the photoelectrons [14], ARPES renders to be inapplicable to study interfacial magnetic structure where a FMI layer is epitaxially grown on the top of TI. Magneto-optical Kerr effect (MOKE) is another promising method, which could be used to determine both in-plane and out-of-plane magnetization, and has been successfully applied in TI studies [30]. However, the resulting signal of rotated polarization is indeed an overall effect of total magnetization projection, without sensitivity to individual layer. Due to the short-range nature of exchange coupling [70, 51, 71, 72, 73, 74, 50], only the thin layer of magnetic moments very close to the interface contributes to the proximity effect, instead of the total measured magnetization as in MOKE. Actually, at the interface of TI/FMI structure, strong spin-orbit coupling may tilt the interfacial magnetic moment and result in a different magnetic structure near the interface [38, 75]. Another powerful characterization tool is polarized neutron reflectometry (PNR), which has shown great advantages [54] thanks to both compositional and depth sensitivity, but PNR only measures the in-plane magnetization component, without resolving the electronic states of TI which participate in the proximity exchange coupling. Therefore, a deeper understanding of TI/FMI proximity, which considers only the near-interface FMI states, with distinguishability of particular TI states involved in the exchange-coupling process, is clearly needed.

In this chapter, we calculate the interlayer coupling constant between two thin layers of FMI, separated by a thin spacer layer of three-dimensional TI, within linear response theory [76] and indirect exchange interaction scheme, which is RKKY type interaction[72, 50] when the system is conducting, and super-exchange interaction when the system is insulating. We take EuS/$Bi_2Se_3$/EuS as an example of FMI/TI/FMI trilayer, due to large magnetic moment of $Eu^{2+}$ ion. Since both interlayer magnetic coupling and magnetic proximity effect share the same physical origin of exchange coupling between FMI and TI, the TI electronic states participating in the proximity effect are naturally expected to be resolved through the interlayer coupling

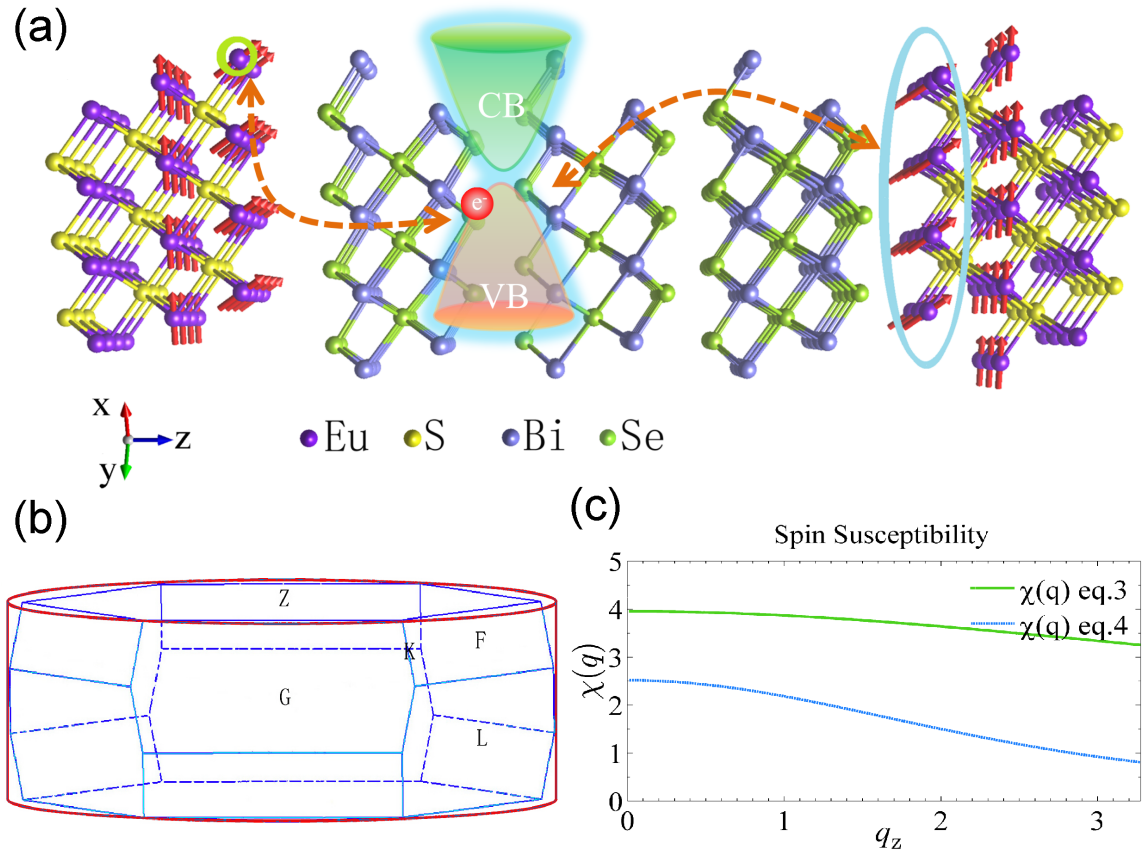


Figure 3-1: a) The atomic configuration of EuS/$Bi_2Se_3$/EuS trilayer, which is a viable example for FMI/TI/FMI structure. The magnetic moment of Eu atoms are shown as red arrows. The spin structure near the interface may be canted near the interface. The interlayer coupling (orange dashed line) is achieved through the electronic states of the TI spacer. b) the original 1st Brillouin zone and the simplified cylindrical integration volume. c) The comparison betweens spin susceptibilities using eqs. 3.3 and 3.4, with 4-band Hamiltonian.

process.

We use one atomic layer thickness of magnetic moment of FMI to describe the short-range exchange coupling interaction, and apply model Hamiltonian of $Bi_2Se_3$ as [23, 77] as the prototype of TI. Despite the fact that density functional theory calculation[40, 78] shows more complicated behavior, such as coexistence of normal and topological surface state, the model Hamiltonian approach is still instructive due to the insights of magnetic coupling it captures, the simplicity when varying the system geometry with no need to build multiple supercells, and is especially useful for non-epitaxial heterostructure where supercell could not be built. In this approach, we show that a ferromagnetic-antiferromagnetic oscillatory coupling also exists when varying the number of quintuple layer (QL) of TI, similar to the interlayer exchange coupling results in Fe/Cr/Fe [72, 79]. Most importantly, we show distinct behaviors of coupling between the massive Dirac TI state and the $p_z$ bands of Bi and Se, due to the paramagnetic nature of Dirac surface state and large diamagnetism of Bi [80, 81] orbitals. The sign difference and the tunability of coupling constant vs Fermi level can be applied independently to identify the TI states contributing to the proximity effect, due to the same origin of short-range magnetic exchange coupling process. Our approach, when applied to various FMI/TI/FMI systems, can be used to better understand the TI/FMI proximity effects, and thus for optimized designing of TI-based spintronic devices.

## 3.2 Theoretical Description of Methodology

### 3.2.1 Interlayer Exchange Coupling Constant

The FMI/TI/FMI trilayer EuS/$Bi_2Se_3$/EuS is schematically represented in Fig. 3-1a. For a given localized magnetic ion (Eu ion in green circle) of FMI close to the interface, the interlayer magnetic coupling constant $I_{12}$ is an overall effect of the indirect exchange coupling of all the Eu ions (blue ellipse) on the other side of TI/FMI interface, through the coupling of electronic states in TI (orange dashed lines). Due

to the localized nature of Eu moments, we could apply the RKKY type of interlayer coupling strength[72, 74, 50],

$$I_{12} = -\frac{A^2 S^2 d}{2V_0^2 (2\pi)^3} \int dq_z d^2 q_\parallel e^{iq_z z} \chi(q_\parallel, q_z) \sum_{R_\parallel \in F_2} e^{iq_\parallel \cdot R_\parallel} \tag{3.1}$$

where $A$ is the amplitude of the contact potential $A\vec{S}_i \cdot \vec{s}$, with $\vec{S}_i$ and $\vec{s}$ are the spins of FMI and TI, respectively, $V_0$ is the atomic volume, $S$ is the spin of the FMI, for $Eu^{2+}$, $S = 7/2$ at 0 K. For finite temperature $T$, in a mean field framework we can estimate $S$ as

$$S(T) = S(0)\left(1 - (T/T_c)^2\right)$$

for EuS $T_c = 16.6$ K. $d$ is the distance between adjacent atomic planes in its original expression, in our present situation, due to layered structure of $Bi_2Se_3$, it is appropriate to take $d \sim 0.96$ nm which is the thickness of 1 QL, since 1 QL is the smallest coarse-grained unit for electronic properties, even though 3 QL is the unit for periodic crystalline structure; $z$ is the distance between two FMI layers, $z = (N+1)d$, where $N$ is the number of QL; $R$ is the in-plane components of the coordinates of the Eu ions to be summed up, and $\chi(q_\parallel, q_z)$ is the $q$-dependent magnetic susceptibility of the TI spacer. The TI states participating in the exchange coupling enter into the $\chi(q_\parallel, q_z)$ term, and are finally reflected in $I_{12}$. This is the theoretical basis why we could study TI/FMI proximity effect by studying interlayer coupling of FMI/TI/FMI.

In Eq. 3.1, the integration of $q$ should be performed within the 1st Brillouin zone of $Bi_2Se_3$ (Fig. 3-1(b), blue polyhedron). However, if we define $q$ and $k$ periodically in reciprocal lattice by using periodic zone scheme instead of folded zone scheme, we could define a prismatic auxiliary zone and use the reciprocal unit cell with prismatic shape. Since the in-plane area is hexagonal and close to a circle, we further define a cylindrical integration zone which shares the same volume with the original 1st Brillouin zone (Fig. 3-1(b), red cylinder), which effectively reduces the integration dimension. Finally, the interlayer coupling constant can be simplified as

$$I_{12} = -\frac{1}{2}\left(\frac{A}{V_0}\right)^2 \frac{S^2 d^2}{2\pi V_0} \int_{-\pi/d}^{+\pi/d} dq_z \chi(q_\parallel = 0, q_z) e^{iq_z z} \tag{3.2}$$

Here we have used the fact that in the period zone scheme, the in-plane and out-of-plane components are decoupled; for $q_\parallel \neq 0$, we have

$$\sum_{R_\parallel \in F_2} e^{iq_\parallel \cdot R_\parallel} = 0$$

.

### 3.2.2 $q$-dependent Spin Susceptibility

In order to calculate the interlayer coupling constant $I_{12}$ in Eq. 3.2, we need the magnetic susceptibility. The spin magnetic susceptibility along direction $\mu$ ($\mu = x, y, z$) $\chi_{\mu\mu,\text{spin}}$ for a generic spinor state can be written using Kubo formula as [82]

$$\chi_{\mu\mu,\text{spin}}(\mathbf{q}) = \frac{\mu_B^2}{4\pi^3} \sum_{\substack{m,occ \\ n,empty}} \int d^3\mathbf{k} \\ \frac{f_0(E_{n,\mathbf{k}}) - f_0(E_{m,\mathbf{k}+\mathbf{q}})}{E_{m,\mathbf{k}+\mathbf{q}} - E_{n,\mathbf{k}} + i\delta} \left|\langle m, \mathbf{k}+\mathbf{q} \left| S_\mu \right| n, \mathbf{k} \rangle\right|^2 \tag{3.3}$$

where $E_{n,\mathbf{k}}$ denotes the eigenvalue at band number $n$ and wavevector $\mathbf{k}$, with corresponding eigenstate $|n, \mathbf{k}\rangle$, $S_\mu$ ($S_z = I \otimes \sigma_z$,$S_x = \tau_z \otimes \sigma_x$ and $S_y = \tau_z \otimes \sigma_y$ ) is the spin operator along direction $\mu$ and $\mu_B$ is the Bohr magneton. The integration over $\mathbf{k}$ is over the cylindrical integration zone in Fig. 3-1(b).

When the spinor structure is absent, and within plane-wave approximation, Eq. 3.3 can be greatly simplified as [76, 83],

$$\chi_{\text{spin}}(\mathbf{q}) = \frac{\mu_B^2}{4\pi^3} \sum_{\substack{m,occ \\ n,empty}} \int \frac{f_0(E_{n,\mathbf{k}}) - f_0(E_{m,\mathbf{k}-\mathbf{q}})}{E_{m,\mathbf{k}-\mathbf{q}} - E_{n,\mathbf{k}} + i\delta} d^3\mathbf{k} \tag{3.4}$$

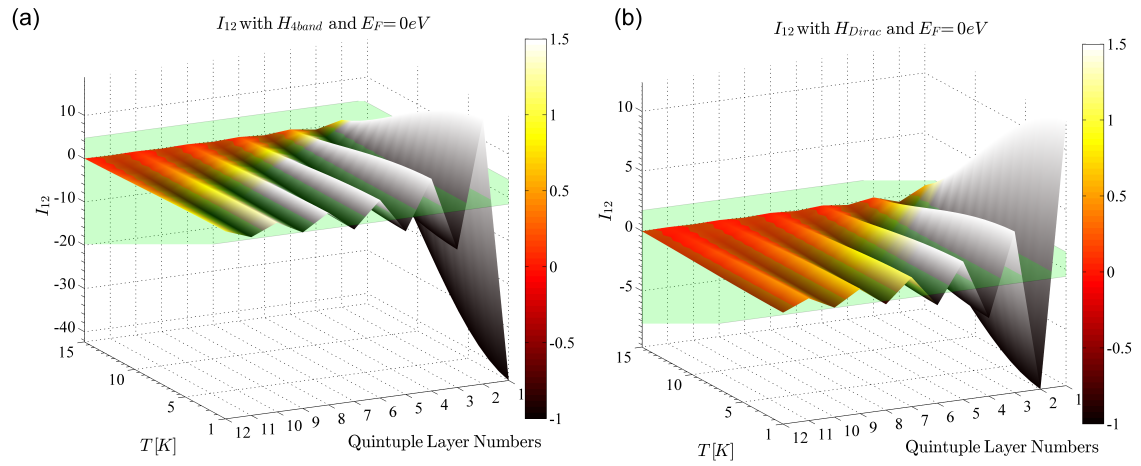


Figure 3-2: The interlayer exchange coupling constant $I_{12}$ as a function of temperature and number of QL, with 4-band Hamiltonian (a) and Massive Dirac Hamiltonian (b). The oscillating ferromagnetic ($I_{12} < 0$) - antiferromagnetic ($I_{12} > 0$) coupling behavior are shown in both cases, but with a sign change.

where $f_0$ is the Fermi-Dirac distribution function.

The comparison between Eq. 3.3 and Eq. 3.4 is shown in Fig. 3-1(c). The resulting spin susceptibility (calculated using Eq. 3.3 and overlap of eigenstates of Hamiltonian Eq. 3.7, is $\sim 1/2$ compared with the result using the simplified version Eq. 3.4. This could be understood as a consequence of spin texture of bands, where electronic transition amplitude for minority spin components is suppressed due to the lack of population in $\sim 1/2$ of the k space[47]. Actually, in order to calculate the exact magnitude of susceptibility, density-functional perturbation theory method which requires the input of realistic states and summation over all bands, is needed[84]. However, since we are more interested in the role that TI state plays in proximity effect, in addition the effective Hamiltonian approach we adopt involves only few bands, in the following we use Eq. 3.4 instead of Eq. 3.3 to calculate the interlayer coupling constant in Eq. 3.1, for computational simplicity but without loss of qualitative illustration.

### 3.2.3 Estimation of Orbital Magnetic Susceptibility

Besides the spin susceptibility which contributes to paramagnetism, due to diamagnetic nature of bulk $Bi_2Se_3$, we include the diamagnetic orbital term as well. The $q$-dependent orbital susceptibility can be regarded as an overlap between eigenstates and their curvatures [81, 83, 84]. In the $q \to 0$ limit, the susceptibility from spin paramagnetism and orbital diamagnetism can be simplified as[76]

$$\chi_{\text{orb}}(q \to 0) = -\frac{4}{3}\left(\frac{m_e}{m^* g^*}\right)^2 \chi_{\text{spin}}(q \to 0) \tag{3.5}$$

where $m^*$ is the effective mass of electron, $D(E)$ is the density of state near energy $E$. In the case of Dirac surface state, $g^* \simeq \frac{2m_e}{m^*}$ is valid[85], hence we expect the spin paramagnetism is dominant for surface states. This is consistent with the recent experimental report about paramagnetic Dirac susceptibility in TI[86]. On the contrary, for bulk parabolic-like bands, $g^* \simeq 2$. [76] Due to the small effective mass of $Bi_2Se_3$, we expect the orbital diamagnetism dominates the spin paramagnetism in bulk $Bi_2Se_3$, which is also true based on experimental value [87]. Neglecting the Van Vleck paramagnetism which is only significant at high temperature[76], the total magnetic susceptibility at low temperature can be written as

$$\chi(\mathbf{q}) \simeq \chi_{\text{orb}}(\mathbf{q}) + \chi_{\text{spin}}(\mathbf{q}) \tag{3.6}$$

### 3.2.4 4-band Model Hamiltonian of TI $Bi_2Se_3$

In order to calculate the magnetic susceptibility in Eq. 3.6, eigenvalues from a model Hamiltonian are needed. Using a 4-band $k \cdot p$ theory, and a basis$\left|p_{1z}^+, \uparrow\right\rangle$, $\left|p_{2z}^-, \uparrow\right\rangle$, $\left|p_{1z}^+, \downarrow\right\rangle$, $\left|p_{2z}^-, \downarrow\right\rangle$, the model Hamiltonian of a TI in $Bi_2Se_3$ family can be written as [40, 77]

$$\begin{aligned} H(k) &= \varepsilon_0(k) I_{4\times 4} + M(k) I \otimes \sigma_z + A_1 k_z \sigma_z \otimes \tau_x \\ &\quad + A_2 k_x \sigma_x \otimes \tau_x - A_2 k_y \sigma_y \otimes \tau_x \end{aligned} \tag{3.7}$$

where $\varepsilon_0(k) = C + D_1 k_z^2 + D_2(k_x^2 + k_y^2)$, $k_\pm = k_x \pm i k_y$, $M(k) = M_0 - B_1 k_z^2 - B_2(k_x^2 + k_y^2)$. For $Bi_2Se_3$ we have $C = -0.0068\,\mathrm{eV}$, $D_1 = 0.013\,\mathrm{eV \cdot nm^2}$, $D_2 = 0.196\,\mathrm{eV \cdot nm^2}$, $M_0 = 0.28\,\mathrm{eV}$, $B_1 = 0.10\,\mathrm{eV \cdot nm^2}$, $B_2 = 0.566\,\mathrm{eV \cdot nm^2}$, $A_1 = 0.22\,\mathrm{eV \cdot nm}$ and $A_2 = 0.41\,\mathrm{eV \cdot nm}$. The doubly degenerate eigenvalues can be written as

$$\begin{cases} E(2^-_{z,\uparrow/\downarrow}, k) = \varepsilon_0(k) + \sqrt{M^2(k) + A_1^2 k_z^2 + A_2^2(k_x^2 + k_y^2)} \\ E(1^+_{z,\uparrow/\downarrow}, k) = \varepsilon_0(k) - \sqrt{M^2(k) + A_1^2 k_z^2 + A_2^2(k_x^2 + k_y^2)} \end{cases} \tag{3.8}$$

where 1=Bi and 2=Se in this notation.

### 3.2.5 Effective Hamiltonian for Massive Dirac Surface States

Contrary to the 4-band model which describes the bulk highest valence and lowest conduction states of $Bi_2Se_3$, the surface states are ideally only localized on the TI surface. However, due to the band bending effect which allows surface-state confinement near the interface, multiple surface states penetrate into the bulk [67], including the Dirac surface states, M-shape valence states and Rashba-split conduction states. The strong band bending effect in $Bi_2Se_3$ can result in a deep penetration of states $\sim$12 QL. Thus, for thin TI spacer, it is still important to consider the possibility that the surface states participating in the interlayer magnetic coupling.

For the purpose of qualitative demonstration, we neglect the M-shape valence states and Rashba-split conduction states, but only keep the Dirac states. The effective Hamiltonian for the Dirac states with gap opening can be written as[23]

$$H_{2D}(k) = Dk^2 I + \begin{pmatrix} \mathcal{H}_D + M \cdot \sigma & tI \\ tI & -\mathcal{H}_D + M \cdot \sigma \end{pmatrix} \tag{3.9}$$

where $\mathcal{H}_D = \hbar v_F(\sigma_x k_y - \sigma_y k_x)$. For 4 QL $Bi_2Se_3$ and magnet MnSe, $M = 28.2\,\mathrm{meV}$, $t = 17.6\,\mathrm{meV}$, $D = 0.098\,\mathrm{eV \cdot nm^2}$, $v_F = 2.66 \times 10^5\,\mathrm{m/s}$. For simplicity we keep these parameters fixed when varying the thickness of TI and the type of magnet. The eigenvalues can be written as

$$E(k) = Dk^2 \pm \sqrt{\hbar^2 v_F^2 k^2 + M^2 + t^2 + 2\sqrt{M^2 t^2 + \hbar^2 v_F^2 (M_x k_y - M_y k_x)^2}} \tag{3.10}$$

In sum, the interlayer coupling constant $I_{12}$ can be thus be calculated by substituting Eq. 3.6 back to Eq. 3.2. The eigenvalues in Eq. 3.10 and Eq. 3.8 can be used to obtain the magnetic susceptibility based on Eq. 3.4. From the modeled Hamiltonian approach, since we are more interested in a qualitative behavior rather than a quantitative magnitude, we regard Eq. 3.5 valid at finite $q$ values to incorporate the orbital contribution.

## 3.3 Results and Discussions

The interlayer coupling constant $I_{12}$ as a function of QL number and temperature are shown in Fig. 3-2, using the bulk 4-band Hamiltonian (Eq. 3.7, Fig. 3-2(a)) and Dirac Hamiltonian (Eq. 3.9, Fig. 3-2(b)). It is remarkable to see that at the same QL number, a sign difference of $I_{12}$ exists when the interlayer coupling are contributed by the valence and conduction electrons or Massive Dirac electrons. This is not only physically reasonable, due to the diamagnetic nature of bulk $Bi_2Se_3$ and paramagnetic nature of the surface states, but also agrees with the recent experimental report [45] which is able to extract paramagnetic Dirac susceptibility in the diamagnetic background in TI.

The significance of the sign difference can hardly be overestimated. In device application using TI/FMI proximity effect, it requires the exchange coupling of FMI with the Dirac surface states to open up the surface band gap. However, the FMI may also couple with other TI states simultaneously. Thus, the sign of $I_{12}$ would tell directly which TI states would dominate the proximity exchange coupling, and provide guidelines to suppress the proximity effect with other TI states while keeping the Dirac surface states dominant for future device design. Moreover, with the aid

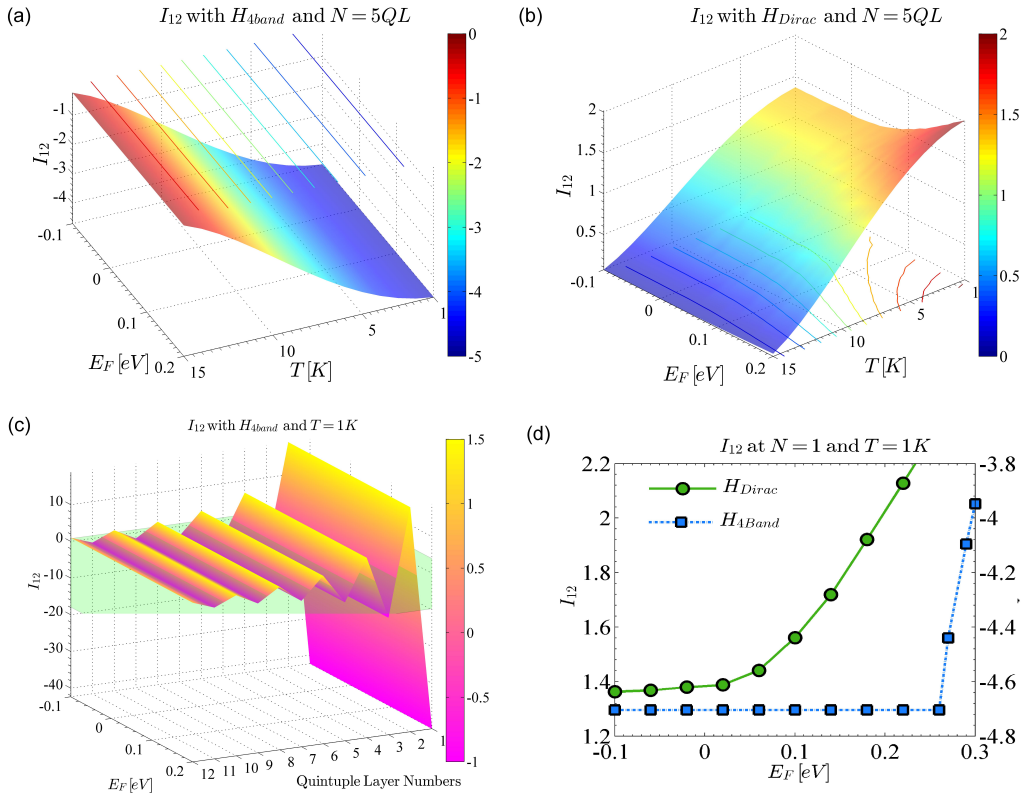


Figure 3-3: a-b) Interlayer coupling constant $I_{12}$ at $T = 1\,\mathrm{K}$, as a function of temperature and Fermi level, for the 4-band and Dirac Hamiltonian, respectively. Within the bulk-band gap, $I_{12}$ does not change for the 4-band Hamiltonian, while $I_{12}$ is sensitive to $E_F$ for the Dirac Hamiltonian. c) The coupling constant $I_{12}$ as a function of quintuple layer number (thickness) and Fermi level, showing the oscillating behavior for all thicknesses. d) The comparison of interlayer coupling constant $I_{12}$ between 4-band Hamiltonian and Dirac Hamiltonian, at 5 QL and 1 K. We see that for the 4-band Hamiltonian $I_{12}$ remains constant while for Dirac Hamiltonian $I_{12}$ keeps changing. This fact can be used to identify the TI states participating in the proximity effect. We can also see that above the bulk band gap, the 4-band $I_{12}$ starts to change dramatically.

of external magnetic field, it is theoretically possible to resolve the relative weights of coupling strength from TI Dirac state and other states, since they have different responses to external magnetic field.

Besides the sign change, the dependence of Fermi level provides further evidence to identify the TI states involved in the proximity effect (Figs. 3-3a and b). We see that for the bulk $p_z$ bands (Fig. 3-3a), $I_{12}$ is insensitive with Fermi level $E_F$ within $\sim 0.3\,\mathrm{eV}$ bulk band gap (Fig. 3-3d, blue square curve), whereas on the contrary,

a sensitive change of $I_{12}$ with $E_F$ (Fig. 3-3b and Fig. 3-3d, green circle curve) is shown when coupled with the Dirac states. Therefore, by varying the Fermi level and measuring the variation of $I_{12}$, it is in principle possible to resolve the particular TI states contributing to the exchange coupling, and determine the relative weights in the proximity effect as well.

Due to the oscillating coupling behavior of nearby QL number, the thickness fluctuation becomes one factor which makes the resulting $I_{12}$ deviated from the ideal case, and hinders further extraction to determine the weights in the proximity effect. In the condition that the lateral correlation length is large enough ($\xi > z$), the averaged effect coupling constant $\bar{I}_{12}$ can be written as averaging over the thickness fluctuations [51]

$$\bar{I}_{12} = \int dz P(z) I(z) \tag{3.11}$$

where $P(z)$ is the distribution function of spacer thickness. For simplicity we define Gaussian distribution

$$P(z) = \frac{1}{\sqrt{2\pi}\sigma} \exp\left(-\frac{(z-\bar{z})^2}{2\sigma^2}\right) \tag{3.12}$$

where $\sigma$ is the thickness variation. Since the Se-Bi-Se-Bi-Se atomic layers within 1 QL is the strong chemical bonding, while the bonding between QLs is weaker van der Waals interaction, we still use 1 QL as the unit of thickness and discretizing $z \propto d$ with $d$ the thickness of 1 QL, without considering the possibility to break the chemical bonds within 1 QL which leads to fractional thickness in the unit of 1 QL. However, $\sigma$ can still be arbitrary as it denotes the relative weights for different thicknesses to appear in the layered structure. As an illustration, the resulting change of $I_{12}$ for 4-band Hamiltonian with different $\sigma$ are shown in Fig. 3-4. When the thickness fluctuation increases, the resulting averaged $\bar{I}_{12}$ drops dramatically. Thus, in order to determine the particular TI states involved in the proximity exchange coupling as well as their relative weights, high-quality samples with negligible thickness fluctuation are desirable.

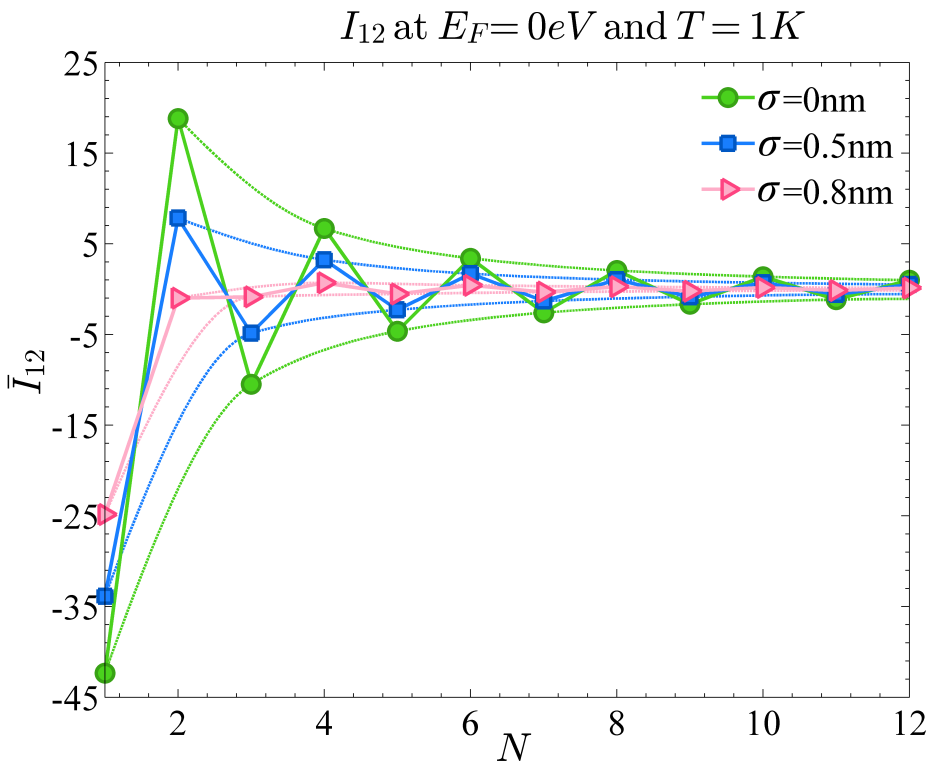


[!ht]

Figure 3-4: The interlayer coupling constant $I_{12}$ at various thickness fluctuation , $\sigma$ = 0.5 and 0.8 nm, using a 4-band Hamiltonian model at $E_F$ = 0 eV and $T$ = 1 K. Stronger thickness fluctuation has a smoothing effect on the overall coupling constant, and may hamper the manifestation of TI states participating in the proximity effect.

### 3.3.1 Magnetic Structure of EuS/$Bi_2Se_3$/EuS Trilayer System

To gain some experimentally insight that how the magnetic structure looks like of such interlayer exchange coupled trilayer system, we measured the magnetic hysteresis and magnetization of a trilayer structure composed of 5 quintuple layer of TI $Bi_2Se_3$, sandwiched between 2 nm of FMI EuS, using Superconducting Quantum Interference Device (SQUID) based Physical Property Measurement System (PPMS). The results are illustrated in Fig. 3-5. The in-plane hysteresis are shown in Fig. 3-5(b),(d), while the out-of-plane hysteresis are shown in in Fig. 3-5(a),(c). We see directly that since it is much easier to saturate at in-plane direction (∼200Oe in-plane comparing with ∼2000Oe out-of-plane at 2K), the magnetic anisotropic easy axis is in the in-plane direction. This means that the coupling between the two layers of EuS is unlikely

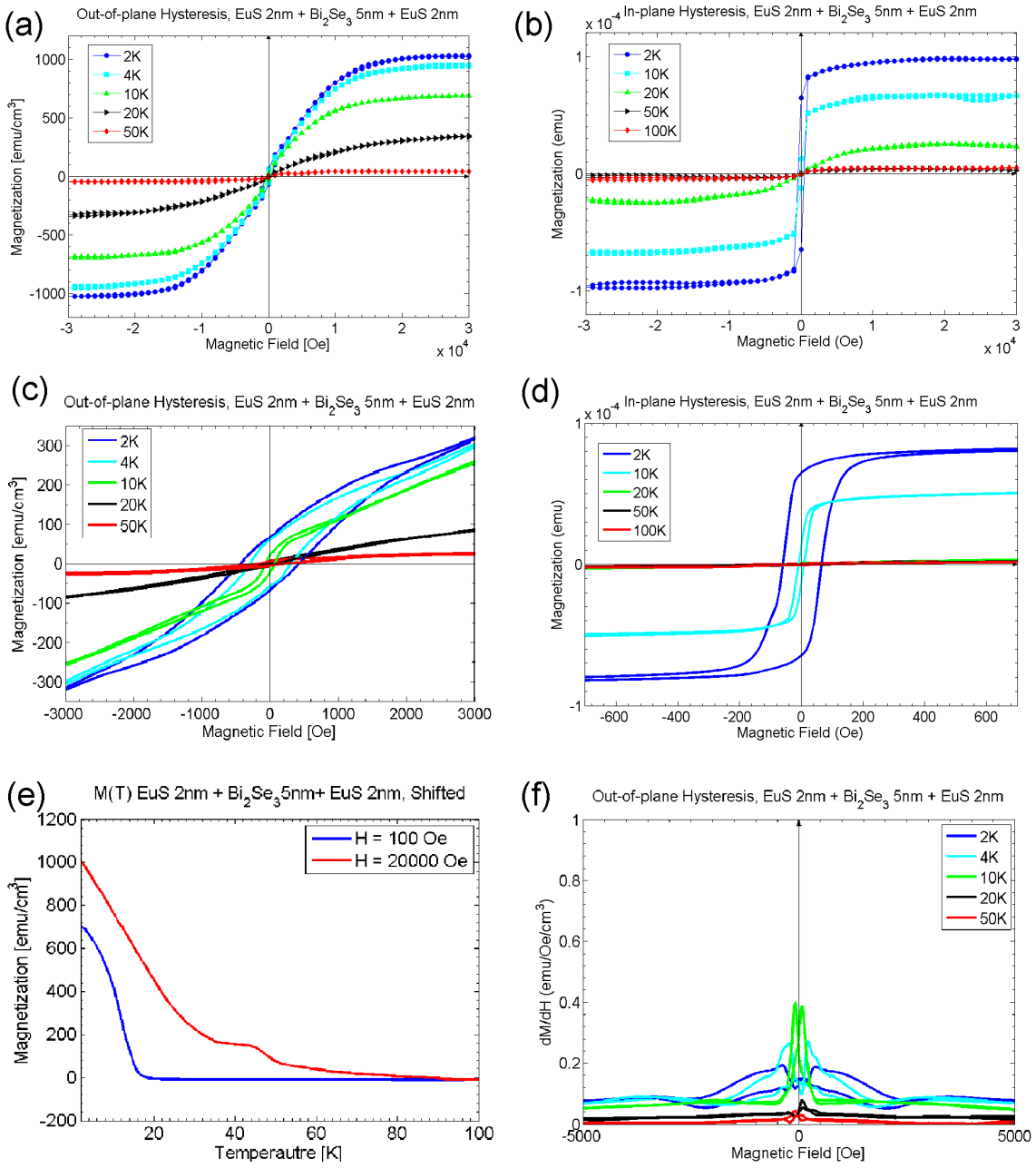


Figure 3-5: The magnetic response of the 2nm EuS/ 5nm $Bi_2Se_3$/ 2nm EuS trilayer system. (a,c) the full range and low-field magnetic hysteresis M(H) in the out-of-plane direction. (b,d) the full range and low-field magnetic hysteresis M(H) in the in-plane direction. (e) M(T), the magnetization as a function of temperature. Despite the coupling between the two EuS layers, at least at low field 100Oe, the Curie temperature stays at its nominal value $T_c$ ~16.6K. (f)The differential magnetic response $\chi = dM/dH$ at various temperatures.

to alter the easy axis. Fig. 3-5(e) is the magnetization M as a function of temperature T, at low and high field, respectively. The nominal value Curie temperature $T_c$ ~16.6K does not change at low field H=100Oe, indicating that the interlayer exchange coupling is also unlikely to alter Curie temperature unless large guiding field is exerted. What's more, the differential response function $\chi = dM/dH$ demonstrates the sensitivity of magnetization $M$ of the trilayer system in response to the external magnetic field $H$.

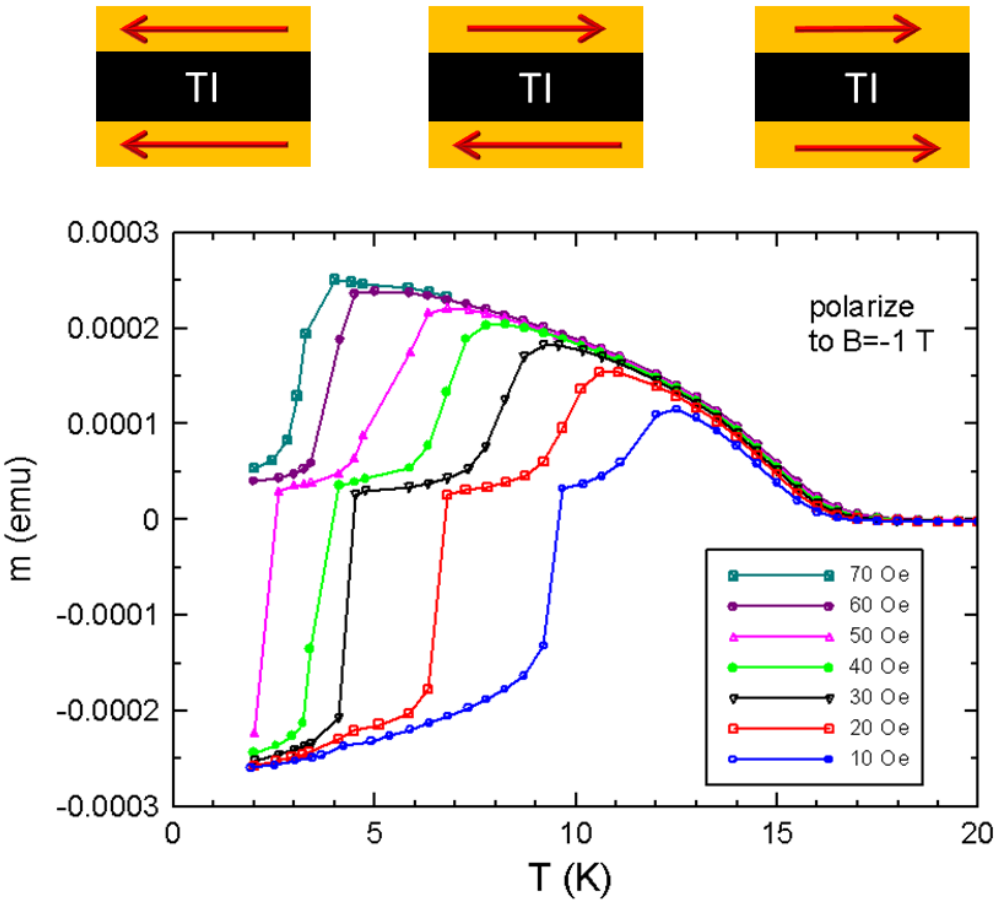


Figure 3-6: Magnetization as a function of temperature, M(T), at various reset fields.

To further illustrate the magnetic structure and response in a trilayer system, we measure the magnetization M(T) of a trilayer system EuS 5nm / 7QL $Bi_2Se_3$ / EuS 5nm, at various reset fields, as shown in Fig. 3-6. To eliminate the memory effect, an intentional temperature increase with either +1T or -1T saturating field is applied to

ensure the reproducibility of the results. After field-cooling down to the lowest temperature 2K, a small reset field- either positive or negative- is applied accompanied with the variation of temperature. In Fig. 3-6, a large negative saturating field is exerted before each set of measurement, which roughly saturates both of the EuS layers. Then when adding a positive reset field and gradually increasing the temperature, it first jumps to a small positive magnitude, indicating an anti-ferromagnetic coupling between the two EuS layers. When the magnetization reaches the peak value, the two EuS layers start to align ferromagnetically.

## 3.4 Chapter Conclusions

We have provided a systematic approach to illustrate the feasibility that how interlayer exchange coupling in FMI/TI/FMI structure can help understand the TI/FMI proximity effect, with the capability to identify the TI states involved in the proximity exchange. By changing the external magnetic field or Fermi level, the weights for the exchange coupling between the FMI and desired TI Dirac states can be obtained. Such information can hardly be obtained directly by the experimental probes such as ARPES, MOKE, PNR or transport, since this approach circumvents the complications of the TI-FMI interaction, but infers the TI states from the simpler indirect FMI-FMI coupling using TI states as medium. In this perspective, the interlayer coupling between two FMIs in the FMI/spacer/FMI structure is not only an interesting phenomenon by itself, but also can be regarded as a probe to study the properties of the spacer.

Moreover, since the interlayer exchange coupling in magnetic multilayers, such as Fe/Cr superlattice[88], has played a significant role in giant magnetoresistance (GMR) [89, 90, 91], the present work also sheds light on the application of magnetic data storage and magnetic field sensors. As shown in Fig. 3-3(d), the interlayer exchange coupling constant could be tuned when coupling with Dirac states of TI. This provides a method to achieve electrically controlled magnetic coupling, with reversibility due to gating, and rapid response due to high-mobility, backscattering-

protected Dirac electrons. The only prerequisite is that the exchange coupling with massive Dirac states should overcome the bulk TI states. This may be realized in thinner TI film where the bulk bands diminish whereas the surface bands dominate. Therefore, further studies of interlayer exchange coupling in TI based magnetic layers for GMR applications, are highly desired.

# Chapter 4

# The Van Vleck Nature of Long-Range Magnetic Order in V-Doped Topological Insulator $Sb_2Te_3$

## 4.1 Introduction

The breaking of time-reversal symmetry (TRS) and opening of surface bandgap of topological insulator (TI) is an essential step towards observing other quantum states [28, 1, 92]. When the TI's chiral Dirac surface state is gapped, a number of promising novel phenomena could be realized, including quantum anomalous Hall effect (QAHE) [92, 27, 36, 93, 45, 33, 94, 95], where spontaneous magnetization and spin-orbit coupling lead to a topologically nontrivial electronic structure, and topological magneto-electric effect results through coupling between electric field and spin texture, which can potentially lead to low-power electrically-controlled spintronic devices [96, 15, 24, 48, 47]. There are two generic approaches to break the TRS: by magnetic proximity effect or by conventional transition metal (TM) doping [28, 38, 97, 98]. Doping TM impurities(*i.e.* V, Cr, Mn) into TI can induce a perpendicular ferromagnetic (FM) anisotropy, providing a straightforward method to open up the bandgap of the TI's chiral surface state and tune the corresponding transport prop-

erties [45, 33, 99, 100, 101, 102, 103]. In diluted magnetic semiconductors (DMSs) doped with TM atoms, the induced FM order in general originates from itinerant charge carriers [104, 105], i.e. Ruderman-Kittel-Kasuya-Yosida (RKKY)-mediated FM order. However, in magnetically doped TI, the itinerant carriers may destroy the QAHE by providing additional conduction channels [46], resulting in a leakage current [15, 106], which severely hinders magnetic TI for device applications. Therefore, a carrier-free yet long range mechanism to induce FM order in magnetically doped TI is highly desirable for progress towards device applications.

On the other hand, in magnetically doped TI, the first-principle calculations predicted that the insulating magnetic ground state can indeed be obtained by a proper choice of TM dopants, through van Vleck-type ferromagnetism in the absence of itinerant carriers [36]. Recently, Chang *et al.* [45, 33] has reported experimental observation of QAHE in magnetic TI Cr- and V-doped $(Bi,Sb)_2Te_3$, where the insulating FM order [103] excludes the RKKY-type interaction and indicates the FM mechanism to be of van Vleck-type as first-principle calculations predicted. In such a system, the inverted band structure in TI leads to the large matrix element of valence band [36, 103, 46], dramatically increasing the contribution to spin susceptibility. Since the van Vleck-type susceptibility is directly related with $2^{nd}$ order energy perturbation [76], one could understand the van Vleck-type mechanism qualitatively from $2^{nd}$ order perturbation theory, as shown in Eq. 4.1

$$E_0^{(2)} = \sum_n{}' \frac{\left| \langle 0 | \, \mu_B (\vec{L} + g\vec{S}) \cdot H \, | n \rangle \right|^2}{E_0 - E_n} \tag{4.1}$$

Here, $\sum'$ denotes the summation over all partially filled states. In this sense, the matrix element $\left| \langle 0 | \, \mu_B (\vec{L} + g\vec{S}) \cdot H \, | n \rangle \right|$ when $n$ becomes valence band is huge, and contributes significantly to the spin susceptibility [36, 46]. On the other hand, Eq. 4.1 also tells us that there are additional contributions from other partially filled states, enabling us to adopt a more direct approach to experimentally prove the van Vleck-type ferromagnetism without the carrier dependence, where electronic states in addition to itinerant electrons will contribute to FM order.

## 4.2 Experimental Description of Electron Energy Loss Spectroscopy

In this Chapter, we report the magnetization of partially filled Vanadium (V) $2p_{3/2}$and $2p_{1/2}$($L_3$ and $L_2$) core states, using low-temperature high-resolution Electron Energy Loss Spectroscopy (EELS). The condition for partial filling of core states is achieved when a high-energy incidence of electrons on a sample in a transmission electron microscope (TEM) excites a core electron to unoccupied states leaving a core-hole behind, giving to the energy-loss spectrum. Analyzing the fine structure of the energy-loss spectrum provides not only the information on the unoccupied local density of states, but also angular momentum, spin and chemical nature of the element. We find that by comparing with room temperature ($RT$) spectrum, the Te $M_{4,5}$ edge at $T$=10K shows no shift, while the V $L_3$ and $L_2$ peaks show a red shift as large as 0.6eV. In addition, there is a clear drop of $L_3/L_2$ peak intensity ratio. EELS simulation with FEFF 9 [107, 108, 109] shows that such a shift is a signature of onset of FM, which is independently verified through magneto-transport results, which shows anomalous Hall effect below the Curie temperature $T_C$ ∼70K.

High-quality V-doped $Sb_2Te_3$ films are grown by molecular beam epitaxy (MBE) under a base vacuum ∼ $5\times10^{-10}$ Torr, where thin film $Sb_2Te_3$ (111) was grown on top of etched Si (111) substrates with V-dopants coevaporated from an electron beam source during TI growth. Ultrathin cross sectional TI film samples are fabricated through focused ion beam and post processing for high-resolution TEM studies. The EELS measurements were carried out using the doubled aberration corrected JEM-ARM200CF TEM, equipped with a cold field-emission gun and the state-of-the-art duel energy-loss spectrometer (Quantum GIF). V-doped $Sb_2Te_3$samples still maintain a very good layered structure (Fig.4-1(a)), due to the likely case that V dopants tend to substitute Sb sites instead of creating interstitials [45]. The selected area electron diffraction (SAD) pattern (Figs. 4-1b,c) along [0001] zone-axis direction also verifies negligible influence of V-dopants to the crystal structure, in that the V-doped $Sb_2Te_3$ has almost identical lattice constant compared with that of pure $Sb_2Te_3$.

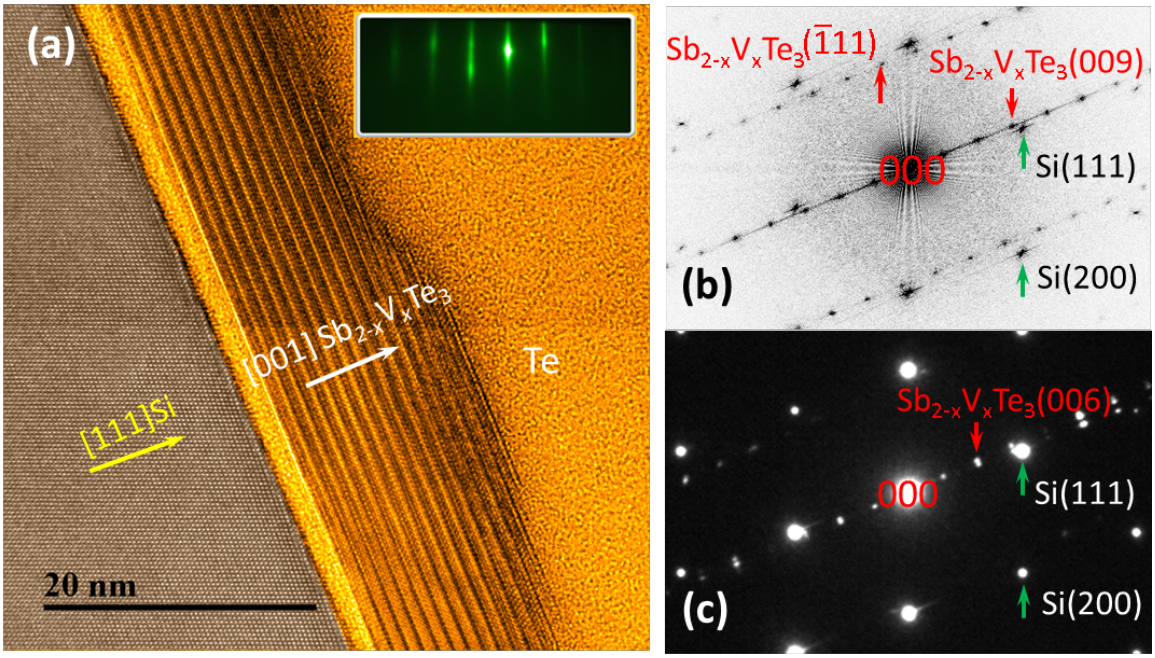


Figure 4-1: (a) High-resolution image of the V-doped $Sb_2Te_3$ sample S3 grown on etched Si substrate (bottom-left, brown region) viewed along $[\bar{1}\bar{1}0]$ of $Sb_{2-x}V_xTe_3$. Another capping layer (top-right, yellow region) is mainly composed of amorphous Te protection layers. The upper left inset is a reflection high-energy electron diffraction (RHEED) image showing the ultrahigh crystalline quality of the MBE-grown film. (b) Diffractogram from(a). One set of spots as indicated by green arrows can be indexed as $(0\bar{1}1)$ pattern of Si, while the other set of spots indicated by red arrows can be indexed as $(\bar{1}\bar{1}0)$ pattern of a rhombohedral lattice with $a$=0.42 nm and $c$=3.03 nm which is basically the same as $Sb_2Te_3$ lattice, indicating negligible influence of V-dopants to the lattice. The [001] $Sb_2Te_3$ is slightly misaligned ($\sim 3^\circ$) with [111] Si (c) Select-area electron diffraction pattern from the area containing both film and substrate.

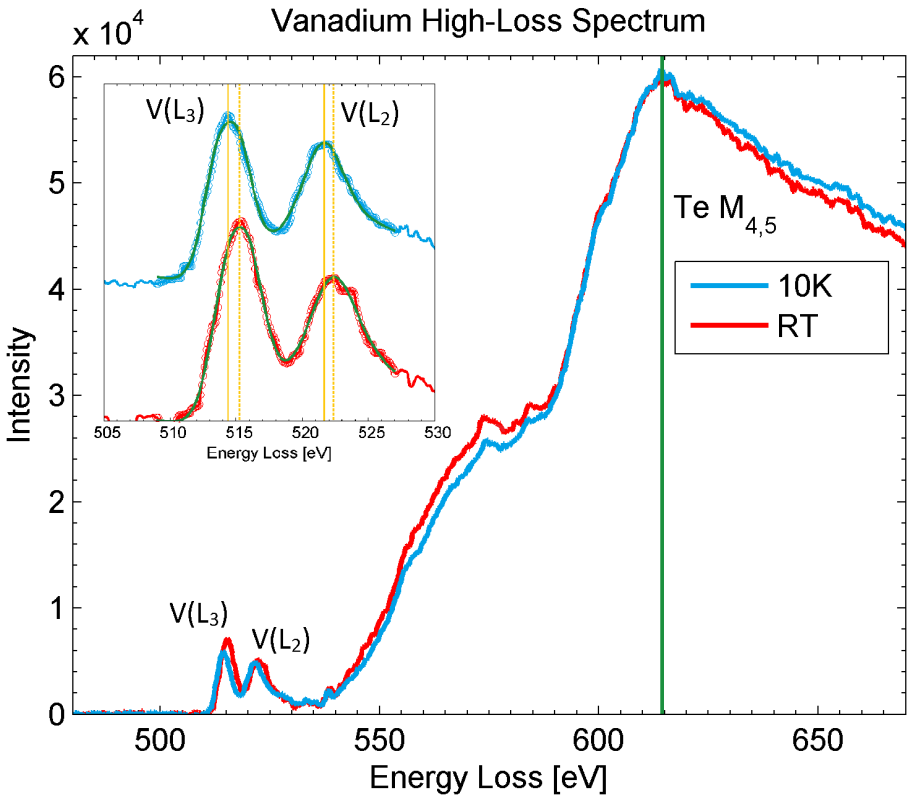


Figure 4-2: EELS spectra of V $L$ and Te $M_{4,5}$ edges at $RT$ (red curve) and 10 K (blue curve) for sample S2, normalized with Te $M_{4,5}$ edge intensity. The energy position of Te $M_{4,5}$edge is invariant as temperature (green line), while there is a clear redshift of vanadium's $L_3$ and $L_2$ positions (yellow lines) and a drop of $L_3/L_2$ ratio. The energy scale has been accurately calibrated by simultaneously acquiring and aligning of the zero-loss peak.

## 4.3 Results and Discussions

### 4.3.1 Low-Temperature Electron Energy Loss Spectroscopy

Fig. 4-2 shows the main result of this Chapter comparing with the EELS spectra in the high-loss region at $RT$ and low temperature $T$=10K. A simultaneous collection of both low-loss and high-loss spectra allows for a high-accuracy positioning of zero-loss peak thus accurate energy scale calibration. We see clearly that the $M_{4,5}$ edge of the Te element does not shift with temperature, while there are obvious peak position shifts (>0.5eV) for both V $L_3$ and $L_2$ peaks, accompanied with a decrease in $L_3/L_2$ ratio.

In order to verify the observed peak shift, we measured three samples of $Sb_{2-x}V_xTe_3$ with different V concentrations and thicknesses, namely sample S1: 20 quintuple layer (QL) with $x$=0.08; S2: 20QL with $x$=0.16 and S3: 12 QL with $x$=0.08. The corresponding mean V-V distances in all the samples are thus $\geq$ 10nm. Since EELS is a spatially highly localized probe and there might be small non-uniformity of dopants, we collected 8 spectra at both 10K and $RT$ for each sample to reduce the measurement uncertainty. Furthermore, we use two different algorithms to extract the peak positions. The averaged V $L_3$ and $L_2$ peak positions and $L_3/L_2$ ratios for all the three samples are plotted in Figs. 4-3 (b-d).

All three samples show the same trend that the $L_3$ and $L_2$peak positions at $T$=10K (blue and green dots in Figs. 4-3b and c) undergo a redshift compared with $RT$ (red and purple dots). For $L_2$ peaks, all three samples shift similar amounts $\sim$ 0.4eV, while for $L_3$ peak positions, the shift ranges from 0.3eV (samples S1 and S3) to 0.7eV (sample S2). This indicates that at low temperature, certain mechanism which does not change Te states alters the $L_3$ and $L_2$ core states of V. The higher concentration of V tends to yield a stronger energy reduction of $L_3$ peaks. In addition, the $L_3/L_2$ ratio drops from $\sim$ 1.4 to 1.1 (samples S2 and S3), indicating a possible change of electronic structure or even a phase transition [110].

### 4.3.2 Spectrum Simulation and Comparison

To understand the possible origin of the peak position shift and peak intensity ratio drop, we simulate the EELS spectrum with a non-magnetic V-doped TI nanosphere using FEFF 9 (Fig. 4-3(a) inset). We take 1.0nm for full multiple scattering cutoff radius and 0.5nm for self-consistent-field cutoff radius to ensure convergence, with Hedin-Lundqvist self-energy and random phase approximation with core-hole correction. The resulting non-magnetic peak positions give $E(L_3)$ =515.1eV and $E(L_2)$ =523.8eV, which are both higher than the magnitude at $RT$. The higher V energy for a non-magnetic system is quite reasonable, since even at $RT$, there is already partial magnetization due to the field in the sample areas from the objective lens of the microscope. In other words, the redshift of V $L_3$ and $L_2$ peaks is consistent with

| $\chi$ | **E** | **2C**$_3$ | **3C'**$_2$ | **I** | **2S**$_6$ | $3\sigma_d$ |
|---|---|---|---|---|---|---|
| $\Gamma^{(2)}_{full}$ | 5 | -1 | +1 | 5 | -1 | +1 |

Table 4.1: Character table of irreducible representation for the full rotational group. When crystal field is present, this becomes a reducible representation and the degeneracy is lifted.

a picture that non-magnetic system has even higher energy.

As shown in Fig. 4-3, the different amount of redshift for $L_3$ and $L_2$ edges is consistent with a temperature-independent Te $M_{4,5}$ position at ~615eV. Sample S2 with highest V concentration ($x$=0.16) shows the highest redshift, indicating that such redshift has an origin related to strong V-V interaction. Moreover, since the $L_3$ and $L_2$ has similar order of peak positions (around 515eV and 521eV), but different $l$-$s$ spin coupling configuration, the different redshift amount between $L_3$ and $L_2$ peaks further indicates that a spin-related process may play an important role in the V-V interaction.

### 4.3.3 Additional Evidence for van Vleck Magnetism From A Group Theoretical Perspective

Thus, the consistently observed trend at $RT$ and $T$=10K of the energy redshift of V's $L_3$ and $L_2$ edge and the decrease of $L_3/L_2$ ratio from non-magnetic simulations unambiguously indicates a change of electronic structure, while the very different redshift behavior between $L_3$ and $L_2$ peak together with a concentration dependence further indicating a magnetic origin from these core levels. Actually, this core-level magnetism for V-dopants could also be understood through crystal field theory. For an $l$=2 transition metal ion dopant (such as V), the character table of irreducible representation for full rotational group is shown in Table 4.3.3. The conjugacy classes are taken as the symmetry elements contained in TI's $D_{3d}$ group. Under TI's rhombohedral $D_{3d}$ crystal field, this irreducible representation $\Gamma^{(2)}_{full}$ becomes reducible, resulting in the lift of degeneracy and crystal field splitting.

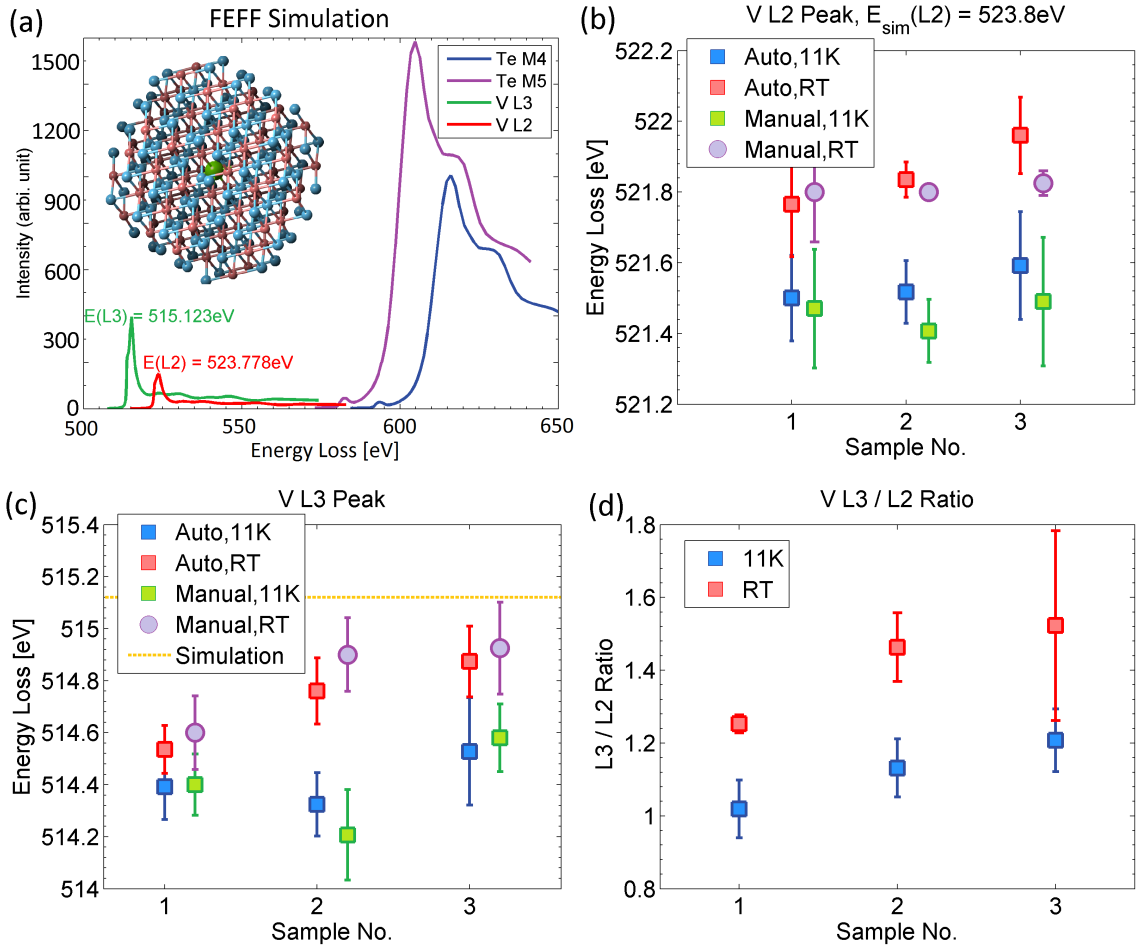


Figure 4-3: (a) FEFF simulation of the high-loss EELS spectrum of V-doped $Sb_2Te_3$, using a nanosphere (inset) with a scattering center in the middle. (b-d) Experimental EELS peak positions and shifts. (b) The V-$L_2$peak positions, showing similar trend of redshift for all three samples. The two algorithms show consistent results (c) The V-$L_3$ peak positions, where sample S2 with highest V-concentration shows highest redshift. A horizontal yellow line marks the energy position from non-magnetic simulation, which is slightly higher than the $RT$ magnitudes. (d) The V's $L_3/L_2$ peak intensity ratio change. At $T$=10K, the ratio drops, which is also consistent with the simulation, where for non-magnetic system the ratio is even higher.

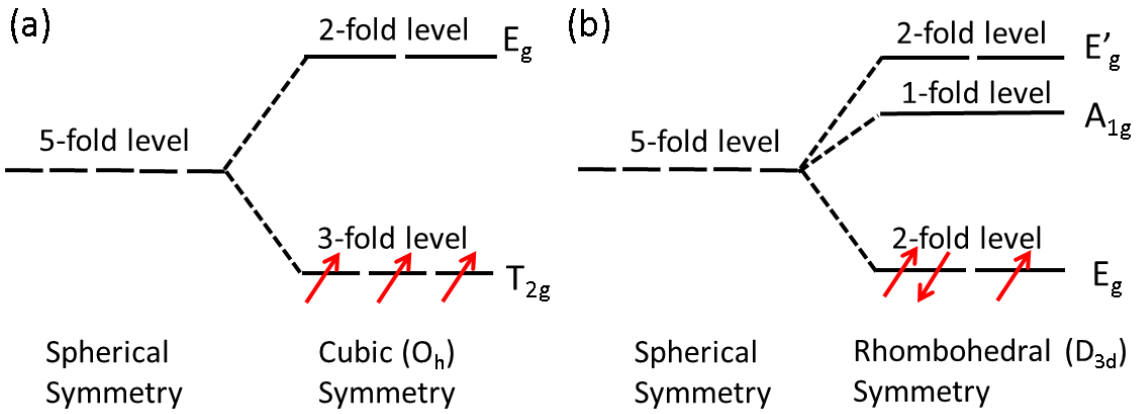


Figure 4-4: (a) Crystal field splitting in cubic crystal field. $T_{2g}$ levels allow the spin alignment from all three *3d* electrons of V (red arrows), leading to a possible FM order. (b) Crystal field splitting under rhombohedral $D_{3d}$ crystal field. Since the energy only splits into a 2-fold level and only 1 electron has unpaired spin it is too weak to form a FM order.

From Table 1 and character table of $D_{3d}$ group [111], we calculate the decomposition of the representation $\Gamma^{(2)}_{full}$ in $D_{3d}$ group as:

$$\Gamma^{(2)}_{full} = A_{1g} \oplus 2E_g \tag{4.2}$$

i.e. instead of splitting to a 2-fold $E_g$ and a 3-fold $T_{2g}$ level which is the case of octahedral crystal field, an $l$=2 transition metal ion would split from a 5-fold level to two 2-fold levels ($E_g$ and $E'_g$) and one non-degenerate level $A_{1g}$ (Fig. 4-4) under TI's rhombohedral crystal field.

Since V has electron configuration [Ar] $3d^3 4s^2$, this crystal field effect tends out to be important to explain why sole V's *3d* electron states may not be sufficient to form FM order in TI. Unlike cubic crystal field where a 3-fold $T_{2g}$ state allows a parallel spin configuration (Fig. 4-4(a)), the 2-fold $E_g$ level and Pauli's exclusion principle only lead to single unpaired electron under rhombohedral crystal field. This becomes too weak to form a long range FM order by solely *3d* valence states (Fig. 4-4(b)). Therefore, the FM order in V-doped TI may be mediated from other V-states, such as core states. This is fully consistent with our EELS results for $L_3$ and $L_2$ core states at $T$=10K.

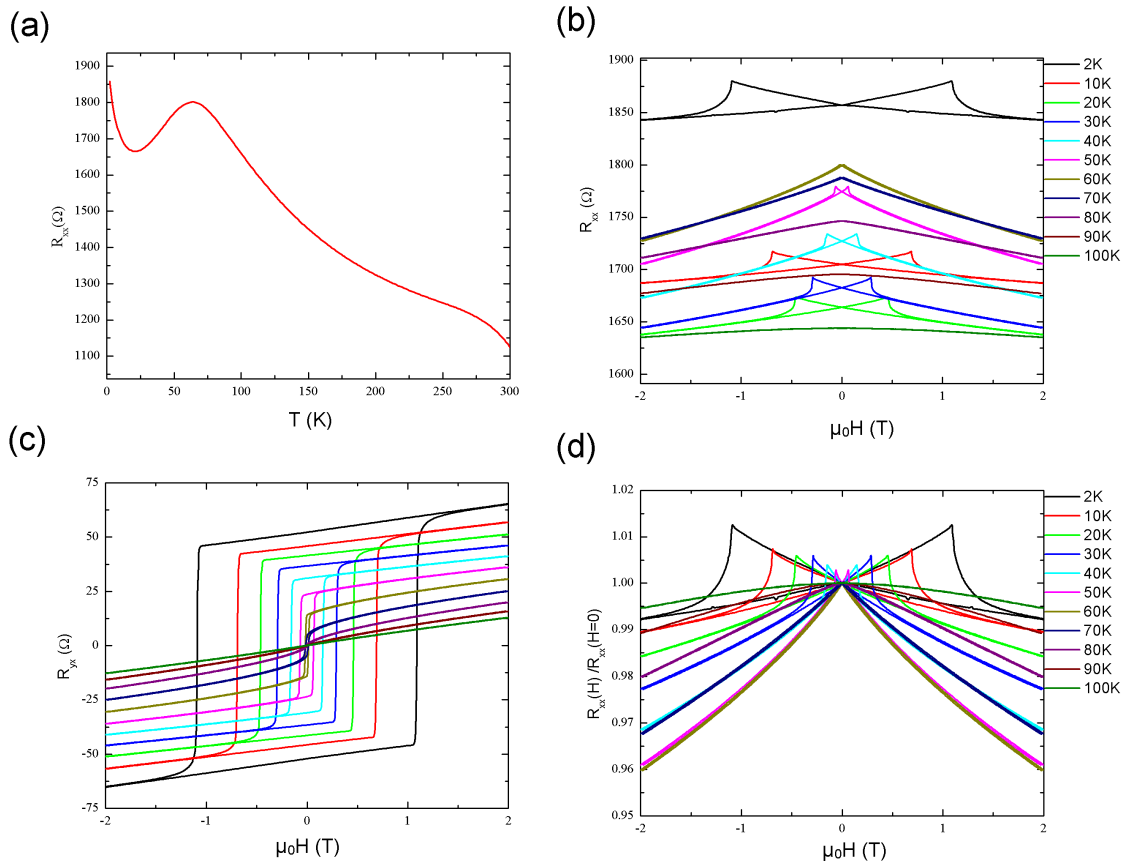


Figure 4-5: (a) Longitudinal resistance $R_{xx}$ as a function of temperature at zero-field. (b) Magnetic-field dependent longitudinal resistance $R_{xx}$ at various temperature, whose feature could be seen more clearly after normalization, as done in (d). Above 70K, it shows weak anti-localization behavior, while below 70K, the butterfly shape indicates the onset of FM order. (c) Magnetic-field dependent Hall resistance $R_{xy}$. The opening up of hysteresis loop below 70K is quite consistent with (a) and (d), indicating an onset of FM order.

### 4.3.4 Direct Transport Result for Demonstration of Magnetic Order

In order to further demonstrate that the V-doped $Sb_2Te_3$ system is indeed FM at $T$=10K, we perform magnetotransport measurement for both longitudinal and transverse directions. Temperature-dependent longitudinal DC resistivity at zero magnetic field (Fig. 4-5(a)) shows a resistivity hump at about 70K, indicating the onset of FM order since the spin-disorder scattering is reduced [112]. Fig. 4-5(b) is the longitu-

dinal magnetoresistance $\rho_{xx}$ at various temperatures. After normalizing to zero field (Fig. 4-5(d)), it shows a typical weak anti-localization behavior and butterfly shape above and below 70K, indicating a non-FM / FM transition. This transition is further corroborated by Fig. 4-5(c), showing the hysteresis loop of the Hall resistance $\rho_{yx}$. The loop is closed above 70K, which is -consistent with the $\rho_{xx}$result. Hence we conclude that the Curie temperature $T_c$to be $\sim$70K, far above the EELS measurement temperature $T$=10K. This independently verifies the FM order of our V-doped $Sb_2Te_3$ sample.

## 4.4 Chapter Conclusions

In conclusion, we have demonstrated the van Vleck nature of FM order in V-doped TI $Sb_2Te_3$ using low-temperature high resolution EELS. An energy redshift is observed in V's $L_3$ and $L_2$ core states, which could be understood as a signature due to the onset of FM order, while the FM order itself is shown independently through magnetotransport measurement. The V-dopants' core-level contribution to the ferromagnetism in TI is thus in sharp contrast to the RKKY-type ferromagnetism, where only itinerant electrons contribute to the magnetic susceptibility regardless the core level states, but consistent with the picture of van Vleck-type ferromagnetism, where the susceptibility is a summation of contribution from all possible intermediate states. In this sense, although we could not exclude the contribution of RKKY interaction to the FM order from the band electrons, van Vleck mechanism, resulting from core levels and playing significant role in FM order, is observed unambiguously. Such a core-level contribution could also be understood from a crystal-field perspective, where three *3d* electrons under rhombohedral crystal field could neither lead to FM order nor screen the contribution from the cores.

# Chapter 5

# Tunable THz Surface Plasmon based on Topological Insulator / Layered Superconductor Hybrid Structure

## 5.1 Introduction to Surface Plasmon

Surface plasmon polariton (SPP) is the collective excitation of electrons at the interface between conductor and dielectrics driven by electromagnetic (EM) waves [113, 114]. Despite its wide applications in nanophotonics [115], near-field optics and tip-enhanced Raman spectroscopy [116, 117], and biological sensors and antennas [118, 119], SPP in general suffers from problem of huge non-radiative loss due to the strong absorption of the metal [113, 114, 115, 116] accompanied with additional radiative loss [120], which limits SPP's lifetime and propagation length for further application in integrated devices.

In order to solve the SPP loss problem, the low-loss plasmonics based on graphene [121, 122, 123, 124, 125, 126, 127, 128, 129, 130, 131, 132, 133, 134, 135] and topological insulators (TI) [136, 137, 138, 139, 140, 141, 142, 143] has attracted much recent attention. In far infrared and THz range, the major loss mechanism in graphene lies in the scattering between electrons and optical phonons [123]. A number of

studies in graphene plasmonics have been conducted utilizing the properties of low loss and tunability. Yan *et al.* [144] have reported enhanced plasmon resonance in patterned graphene-insulator stack structure comparing with single-layered graphene, while Ju *et al.* [124] demonstrated an enhanced tunability at THz range in micro-ribbon graphene metamaterials. These efforts target at manipulation of photons and miniaturization of optical devices, and could be further integrated and hybridized toward further applications in detectors, modulators or other integrated devices.

On the other hand, in doped 3D TI, the electron-impurity scattering becomes dominant due to weak electron-phonon coupling [140], with a further reduced backscattering probability thanks to topological protected surface states [37, 1, 28]. However, unlike the booming studies in graphene plasmonics, the plasmon hybrid devices in TI have been seldom reported, even with comparable performance in THz range as well as other promising features such as net spin polarization, i.e. "spin plasmon" [136, 137, 138, 143] and spin-charge separation [142].

Therefore, in this chapter, we propose a plasmonic hybrid structure composed of 3D TI in close contact with layered superconductor. This structure provides a new platform where SPP waves are supported. The tunability of the SPP propagation can be achieved independently through either gate voltage or external magnetic field. Since the Majorana bound states, which are non-Abelian anyons in superconductors and have great significance in topological quantum computation[1, 149, 18, 20], are predicted to exist at the boundary between 3D TI and superconductor, this plasmonic structure may provide a new perspective in search of Majorana bound states.

## 5.2 Theory

### 5.2.1 Dispersion Relation of Anisotropic SPP Wave

Since the SPP wave is well localized at the interface, while the Dirac electrons only exist on the surface of TI, we could apply anisotropic dielectric functions to model the dielectric function of a 3D TI in order to capture both the dielectric function of

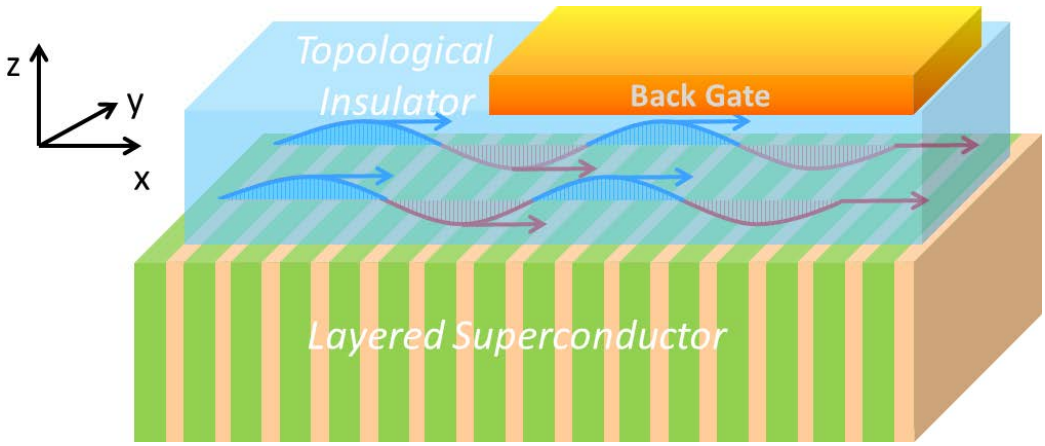


Figure 5-1: The schematic configuration of 3D TI-layered superconductor hybrid structure. The $z < 0$ region consists of alternating layers of superconductor and insulator. The SPP wave propagates along the interface. A back gate is present to tune the Fermi level of the interfacial electrons, which leads to a change of dielectric functions and furthermore a change of SPP propagation properties.

surface 2D chiral Dirac electrons (Fig. 5-1, $xy$ plane, $z = 0$) and the bulk dielectric constant (Fig. 5-1, $z > 0$ region).

In order to describe wave propagation in the layered structure( Fig. 5-1 $z < 0$ region), we adopt the method proposed by Averkov et al [145] using anisotropic dielectric function. This is valid when $\lambda_{SP} \gg D$ , where $\lambda_{SP}$ is the SPP wavelength, and $D$ is the spatial periodicity of the layered structure. Since we are interested in long wavelength THz range, the condition that $\lambda_{SP} \gg D$ is guaranteed to meet.

In this approach, the anisotropy leads to the existence of optical axis where EM wave suffers no birefringence [146]. Thus the electric field and magnetic field at the interface can be written as a superposition of ordinary wave and extraordinary wave:

$$\begin{cases} \mathbf{E}_j = \left( \mathbf{E}_j^o e^{-\kappa_j^o |z|} + \mathbf{E}_j^e e^{-\kappa_j^e |z|} \right) e^{i(q_x x + q_y y - \omega t)} \\ \\ \mathbf{H}_j = \left( \mathbf{H}_j^o e^{-\kappa_j^o |z|} + \mathbf{H}_j^e e^{-\kappa_j^e |z|} \right) e^{i(q_x x + q_y y - \omega t)} \end{cases} \tag{5.1}$$

where $j = 1, 2$ denotes the TI and layered superconductor side, respectively. Based

on our model, the TI dielectric function is defined as $\varepsilon_1 = (\varepsilon_{2D}(q,\omega), \varepsilon_{2D}(q,\omega), \varepsilon_d)$ with optical axis along $z$ direction, while the dielectric function of layered superconductor is defined as $\varepsilon_2 = (\varepsilon_c(\omega), \varepsilon_{ab}(\omega), \varepsilon_{ab}(\omega))$, which is anisotropic along $x$ direction.

By noticing the different direction of optical axis in the upper TI region and lower superconductor region, that for ordinary wave and extraordinary wave we have $E^o_{1z} = 0$, $E^o_{2x} = 0$, and $H^e_{1z} = 0$, $H^e_{2x} = 0$, respectively. These equalities are valid approximately, since when the gap is opened, The electromagnetic constitutive relation is modified to incorporate the topological magnetoelectric effect [63],

$$\begin{cases} \mathbf{D} = \epsilon\mathbf{E} - \frac{\epsilon_0 c\alpha\theta}{\pi}\mathbf{B} \\ \\ \mathbf{H} = \frac{1}{\mu}\mathbf{B} + \frac{\alpha\theta}{c\mu_0\pi}\mathbf{E} \end{cases} \tag{5.2}$$

However, despite the $O(\alpha)$ correction to the electromagnetic field by this axion constitutive relation, it actually contributes only to an order of $O(\alpha^2) \sim 10^{-4}$ correction to the plasmon energy[63]. Moreover, since we are interested in the relative SPP energy shift upon gating or gapping other than the absolute magnitude of SPP energy, the contribution from axion term will be canceled out when calculating the energy difference, since the un-gated or gapless SPP energy already contains contribution from the axion term [147]. Thus, compared with the huge energy shift($\sim 1\%$ originated from gapping or doping), in all following calculations, we could safely neglect the axion term and set $\alpha = 0$. Within this approximation, the components of the EM fields are shown in Appendix 1, with light speed in vacuum $c = 1$ and $\mu$ is the magnetic permeability of the layered superconductor material.

Substituting the EM field components back to Eq. 5.1, we obtain the localization constants, i.e. inverse of penetration depth away from the interface.

$$\begin{cases} \kappa_1^o = \sqrt{q_x^2 + q_y^2 - \varepsilon_{2D}(q,\omega)\omega^2} \\ \kappa_1^e = \sqrt{\varepsilon_{2D}(q,\omega)\left(\frac{q_x^2+q_y^2}{\varepsilon_d} - \omega^2\right)} \\ \kappa_2^o = \sqrt{q_x^2 + q_y^2 - \mu\varepsilon_{ab}(q,\omega)\omega^2} \\ \kappa_2^e = \sqrt{\frac{\varepsilon_c(q,\omega)}{\varepsilon_{ab}(q,\omega)}q_x^2 + q_y^2 - \mu\varepsilon_c(q,\omega)\omega^2} \end{cases} \tag{5.3}$$

The dispersion relation of the resulting surface wave can be written in a determinant form:

$$\begin{vmatrix} -i\kappa_1^o & \frac{i\omega^2\varepsilon_1}{\kappa_1^e} & -\frac{q_y^2-\left(\kappa_2^o\right)^2}{i\mu\kappa_2^o} & 0 \\ -q_y^2 & q_x^2 & 0 & -q_x^2+\mu\omega^2\varepsilon_{ab} \\ \kappa_1^o q_y^2 & \frac{\omega^2 q_x^2\varepsilon_1}{\kappa_1^e} & \frac{q_x^2 q_y^2}{\mu\kappa_2^o} & \omega^2\varepsilon_{ab}\kappa_2^e \\ 1 & 1 & -1 & -1 \end{vmatrix} = 0 \tag{5.4}$$

In this paper, we only consider the wave propagating along x direction, neglecting the oblique excitation. The dispersion relation can finally be simplified as

$$q = \omega\sqrt{\frac{\varepsilon_d\varepsilon_{ab}(\omega)\left[\varepsilon_c(\omega) - \mu\varepsilon_{2D}(q,\omega)\right]}{\varepsilon_c(\omega)\varepsilon_{ab}(\omega) - \varepsilon_{2D}(q,\omega)\varepsilon_d}} \tag{5.5}$$

which is the main analytical result. In this expression, $\mu$ is the effective permeability of the layered superconductor structure, q is the wavenumber along $x$ direction, and can be a complex number. When both the upper and lower materials are isotropic, i.e. $\varepsilon_{2D} = \varepsilon_d = \varepsilon_1$ and $\varepsilon_{ab} = \varepsilon_c = \varepsilon_2$, it is further reduced to the well-known result $q = \omega\sqrt{\frac{\varepsilon_1\varepsilon_2}{\varepsilon_1+\varepsilon_2}}$.

### 5.2.2 Dielectric Function of Layered Superconductor

Define dimensionless frequency $\Omega = \omega/\omega_J$, with $\omega_J$ the Josephson plasmon frequency of the layered superconductor, the dielectric function of layered superconductor can

be written as [145]:

$$\varepsilon_c(\Omega) = \varepsilon_s \left(1 - \frac{1}{\Omega^2}\right), \quad \varepsilon_{ab}(\Omega) = \varepsilon_s \left(1 - \frac{\gamma^2}{\Omega^2}\right) \tag{5.6}$$

where the imaginary parts are neglected. Throughout this article, we take the value reported in [145] and set the interlayer dielectric constant $\varepsilon_s = 16$, current-anisotropy parameter $\gamma = 200$ and $\omega_J = 4\,\mathrm{meV}$.

### 5.2.3 Dielectric Function of Gapless Topological Insulator

The dielectric function of the chiral gapless topological insulator surface have been reported in [136, 137, 139], where for the Hamiltonian for 2D helical Dirac electron gas $\mathcal{H}_0$:

$$\mathcal{H}_0 = \hbar v_F \sum_k \Psi_k^+ \left(\hat{z} \times \vec{k}\right) \cdot \vec{\sigma} \Psi_k \tag{5.7}$$

the Lindhard Dielectric function $\varepsilon_{2D}(q, \omega)$ can be written as

$$\varepsilon_{2D}(q,\omega) = 1 - V_{2D}(q)\Pi(q,\omega) = 1 - \frac{e^2}{2\varepsilon_0 q}\Pi(q,\omega) \tag{5.8}$$

with the polarization operator

$$\Pi(q,\omega) = \frac{g}{4\pi^2} \sum_{\gamma,\gamma'} \int d\mathbf{k} \frac{n_{\mathbf{k},\gamma} - n_{\mathbf{k}+\mathbf{q},\gamma'}}{\hbar\omega + E_{\mathbf{k},\gamma} - E_{\mathbf{k}+\mathbf{q},\gamma'} + i\delta} |\left\langle f_{\mathbf{k},\gamma} | f_{\mathbf{k}+\mathbf{q},\gamma'} \right\rangle|^2 \tag{5.9}$$

In this expression, $g$ is the spin/valley degeneracy, for the chiral states we have $g = 1$ due to spin-momentum locking, $n_{\mathbf{k},\gamma}$ is Fermi occupation value at energy eigenvalue, $E_{\mathbf{k},\gamma} = \gamma\hbar v_F k$, with $\gamma = 1$ for conduction band and $\gamma = -1$ for valence band, respectively. The spinor eigenstates $|f_{\mathbf{k},\gamma}\rangle = \left(e^{-i\theta_\mathbf{k}/2},\ i\gamma e^{i\theta_\mathbf{k}/2}\right)/\sqrt{2}$, with $\theta_\mathbf{k}$ defined as $\tan\theta_\mathbf{k} = k_y/k_x$. We take the value of Fermi velocity $v_F = 6.2 \times 10^5\,\mathrm{m/s}$ [4] in all calculations.

RPA-Relaxation time (RT) approximation[148] can be applied to describe the

SPP damping along the propagation direction, which leads to a finite propagation length. Defining polarizability $\chi(q,\omega) \equiv \frac{e^2}{q^2}\Pi(q,\omega)$, the renormalized polarizability, taking the conservation of electron number into account, can then be written as

$$\chi_\tau(q,\omega) = \frac{(1+i/\omega\tau)\chi(q,\omega+i/\tau)}{1+(i/\omega\tau)\chi(q,\omega+i/\tau)\chi(q,0)} \tag{5.10}$$

where $\tau$ is the relaxation time, which is in general frequency-dependent, and mainly originated from the electron-phonon coupling, scattering by superconductor quasi-particles as well as impurities scattering. In this situation, $\tau$ can be calculated using electron self-energy[123],

$$\Sigma(E) = \Sigma_{e-ph}(E) + \Sigma_{sc}(E) + \Sigma_{imp}(E) \tag{5.11}$$

When the SPP frequency is higher than the gap of the superconductor or above the optical frequency of the topological insulator, the self energy in Eq. 5.11 contains prominent imaginary part, which leads to a drastic reduction of propagation length. However, since we are interested in low frequency SPP ($\omega < \omega_J = 4meV$, shown in Fig. 5-2),where only impurity scattering dominates, the relaxation time can be directly written as $\tau = \mu\hbar\sqrt{n\pi}/ev_F$, without the need of implementing Eq. 5.11. Since $\tau \sim 10^{-12}s$ is a very large quantity, and moreover we are interested in the frequency and the tunability of SPP, other than the exact propagation length, for simplicity, we take $\tau = \infty$ in all following calculations, using Eq. 5.9 instead of Eq. 5.10.

Eq. 5.9 can be calculated either analytically [122, 139]or numerically, thanks to the identical expression of polarization operator within RPA for simple Dirac gas and helical Dirac gas. In our approach, we choose $T = 10\,\mathrm{K}$ for numerical integration to avoid discontinuity, and compare with analytical result with at least 6 digit agreement. Then the numerical result for gapless TI is applied to solve for the dielectric function of TI when surface state is gapped.

### 5.2.4 Dielectric Function of Gapped Topological Insulator

Either the magnetic field perpendicular to the interface ($z$ direction in Fig. 5-1) or the superconductivity would open up a gap to the gapless Dirac cone, and lift out the degeneracy at $k = 0$, and further alter the dielectric function as well as SPP dispersions. In order to take into account the effect of gaps, we adopt the Bogoliubov-de Gennes Hamiltonian [37, 18], which can be regarded as a generalization of Eq. 5.7:

$$\mathcal{H}_{BdG}=\frac{1}{2}\sum_{\mathbf{k}}\Psi_{\mathbf{k}}^{+}\begin{pmatrix} k_x\sigma_y-k_y\sigma_x+M\sigma_z-E_F & i|\Delta|\sigma_y \\ -i|\Delta|\sigma_y & -k_x\sigma_y-k_y\sigma_x-M\sigma_z-E_F \end{pmatrix}\Psi_{\mathbf{k}} \tag{5.12}$$

where spinor $\Psi_{\mathbf{k}} = \left(c_{\mathbf{k}\uparrow}, c_{\mathbf{k}\downarrow}, c^{+}_{-\mathbf{k}\uparrow}, c^{+}_{-\mathbf{k}\downarrow}\right)$, $M$ and $|\Delta|$ denote the magnetic gap and superconductivity gap, respectively, $E_F$ is the chemical potential. Both Eq. 5.8 and Eq. 5.9 still hold, but the eigenvalues and eigenvectors are changed. The eigenvalues can now be written as

$$\begin{aligned}
E_1 &= \sqrt{|\Delta|^2+2\left(|\Delta|^2M^2+E_F^2M^2+E_F^2k^2\right)^{1/2}+M^2+k^2+E_F^2} \\
E_2 &= \sqrt{|\Delta|^2-2\left(|\Delta|^2M^2+E_F^2M^2+E_F^2k^2\right)^{1/2}+M^2+k^2+E_F^2} \\
E_3 &= -\sqrt{|\Delta|^2-2\left(|\Delta|^2M^2+E_F^2M^2+E_F^2k^2\right)^{1/2}+M^2+k^2+E_F^2} \\
E_4 &= -\sqrt{|\Delta|^2+2\left(|\Delta|^2M^2+E_F^2M^2+E_F^2k^2\right)^{1/2}+M^2+k^2+E_F^2}
\end{aligned}$$

The corresponding unnormalized eigenvectors are shown in Appendix 2.

## 5.3 Results and Discussions

In order to conveniently express the dielectric functions for both TI and layered superconductor, we define dimensionless wavenumber $Q = v_F q_x/(c\omega_J)$, and all energies are dimensionless and expressed in the unit of $\omega_J$.

The SPP dispersion relations are obtained by solving Eq. 5.5. The typical disper-

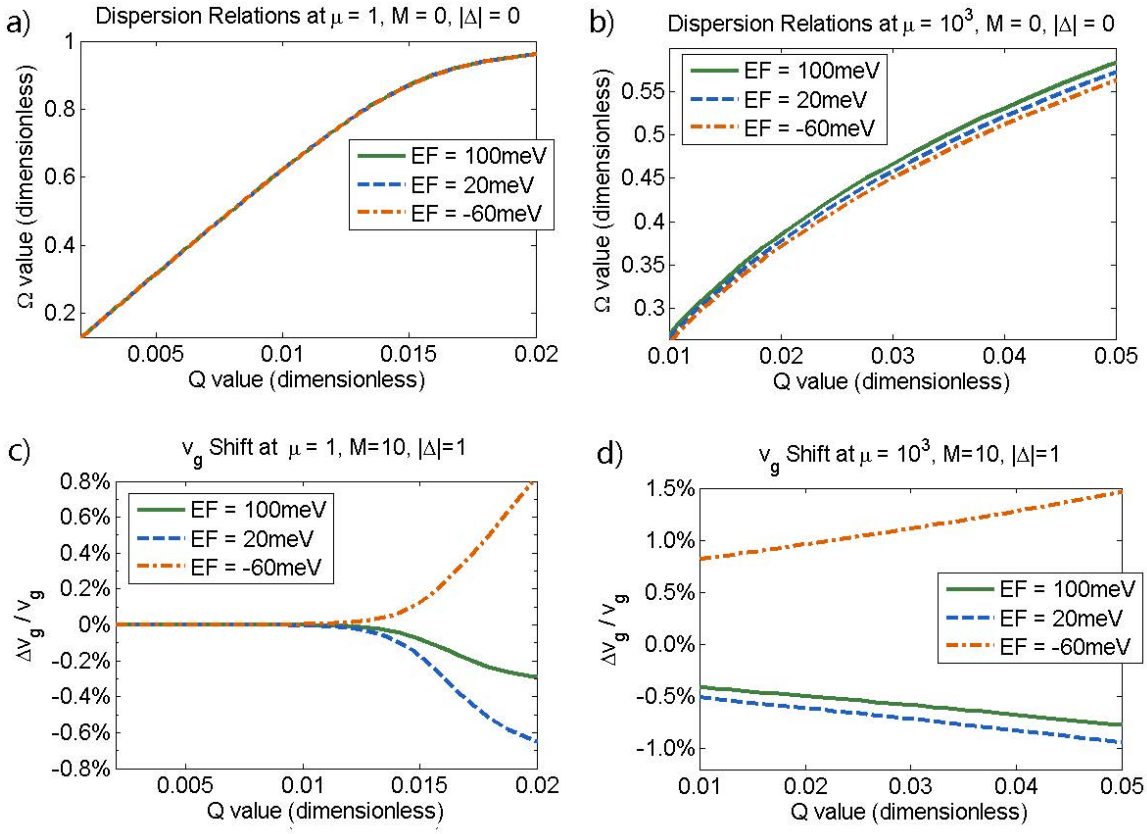


Figure 5-2: The dispersion relations (a-b) and gap-induced group velocity changes (c-d) of SPP at various Fermi levels with respect to gap opening. The Fermi levels are taken at 3 different values with 80 meV interval. In c), at $\mu = 1$, even if the tuning of Fermi level does not change much to the dispersion relation itself as shown in a), it still shows a shift to SPP group velocity at high $Q$ range.

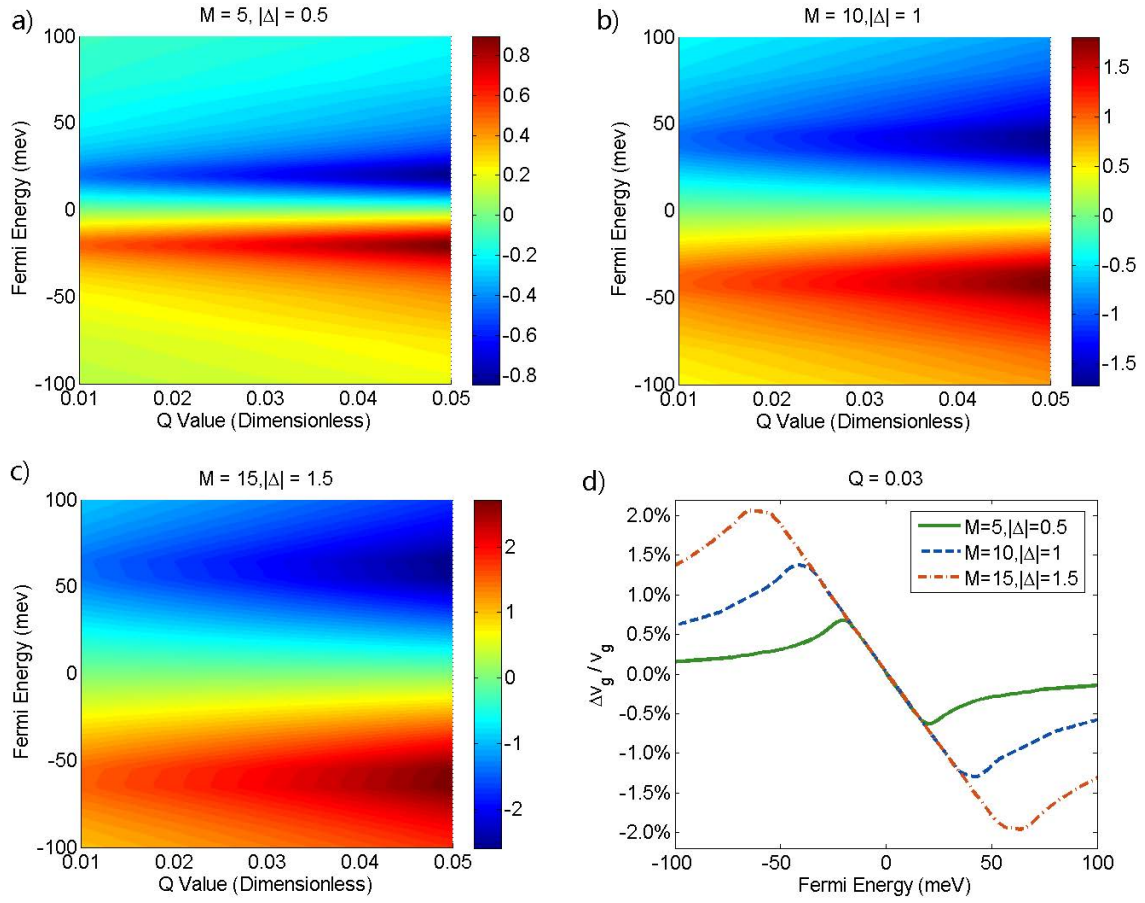


Figure 5-3: The percentage shift of SPP group velocity as a function of $Q$ and $E_F$, at 3 different gap values $M = 5$ $|\Delta| = 0.5$ (a), $M = 10$ $|\Delta| = 1.0$, (b) and $M = 15$ $|\Delta| = 1.5$, (c). The change is negative for $E_F > 0$ and positive for $E_F < 0$, and reaches maximum when the Fermi level is close to the gap values (d). Notice all gap values are expressed in the unit of $\omega_J$ ($\omega_J = 4\,\text{meV}$ throughout calculation), for instance the green solid line $M = 5$ $|\Delta| = 0.5$ corresponds to $M = 20\,\text{meV}$ $|\Delta| = 2\,\text{meV}$.

sion relations at various gate voltages, i.e. Fermi levels $E_F$, are shown in Fig. 5-2 a and b. We see an enhanced tunability, i.e. shift of dispersion relation when $E_F$ varies, when the lower layer has increased effective magnetic permeability $\mu$. By defining the SPP group velocity $v_g = d\Omega/dQ$, we see an additional change of propagation properties induced by either $M$ or $|\Delta|$ (Fig. 5-2 c and d) by plotting the percentage SPP group velocity shift

$$\frac{\Delta v_g}{v_g} = \frac{v_g(gapped) - v_g(gapless)}{v_g(gapless)}$$

Here both the magnetic gap $M$ and superconductivity gap $|\Delta|$ are dimensionless in the unit of Josephson plasmon frequency $\omega_J$.

In order to further investigate the effect of gap to the SPP propagation, the relative shift of group velocity $\Delta v_g/v_g$ as a function of dimensionless wavenumber $Q$ and Fermi level $E_F$ are shown in Fig. 5-3, at different values of gap. It can be seen directly that the shift is increased at larger gap value, and it increases as a function of Q. Most importantly, the shift reaches peak value when the Fermi level approaches to the gap value. This feature can be seen more clearly in a line plot with fixed $Q$ value (Fig. 5-3 (d)).We also see that SPP group velocity $v_g$ does not shift when Fermi level $E_F = 0$.

In contrary to the $Q$ and $E_F$ dependent shift of group velocity caused by energy gap, the localization constants show a qualitatively different behavior. The localization constant in TI side $\kappa_1^o$ is neither sensitive to $E_F$ nor to $Q$ (Fig. 5-4(a)(c)(e)), while in layered superconductor side, $\kappa_2^o$ is tunable by $E_F$ but still $Q$-independent. The importance of the localization constant shift as $Q$ can hardly be overestimated, in that it indicates that the different propagation properties of SPP is almost fully coming from the group velocity, other than the difference in SPP wavelength. The fewer controllable variables would indefinitely make the experimental results easier to explain.

The reason that the maximum $v_g$ shift occurs when the gap matches the Fermi level can be understood in the light of electronic transition and available electron density for plasmonic oscillation. Electrons in the conduction band are mostly extended and dominate the surface plasmon excitation. When the Fermi level is lower than

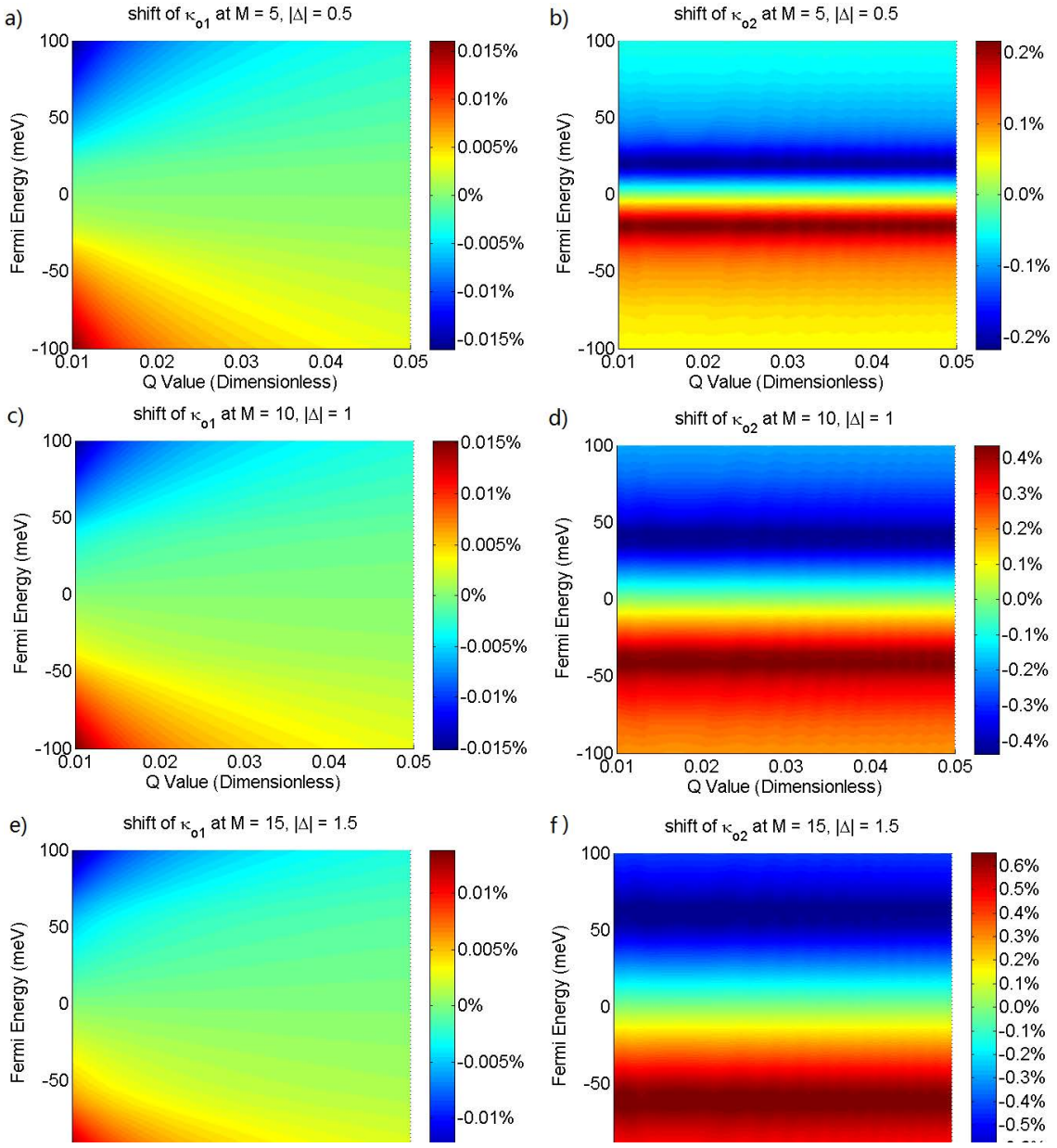


Figure 5-4: Relative shift of o-light component of localization constants for TI $\kappa_1^o$ (figs a, c, e), and layered superconductor $\kappa_2^o$ (figs b, d, f). The localization constants for e-light $\kappa_1^e$ and $\kappa_2^e$ have different magnitudes but similar feature of $\kappa_1^o$ and $\kappa_2^o$, respectively. We see that the shift is not sensitive to Fermi level $E_F$ of topological insulators, but always reaches peak values when $E_F$ is near the value of gap. Unlike the shift of group velocity, which is $Q$ dependent, the localization constants are almost independent $Q$ value.

the energy gap, charge carriers need additional energy to fulfill the transition to the conduction band in order to contribute to the collective excitation. On the other hand, since the SPP is excited by EM waves, when the Fermi level is higher than the energy gap, the electronic transition by optical excitation is limited by occupied electrons. The increasing forbidden transition leads to a reduced shift of dielectric function, and moreover the $v_g$ shift is reduced accordingly. Thus, only when the Fermi level reaches the value of energy gap are the number of available electrons participating in the electronic transition and collective excitation maximized, and leads to a shift of SPP frequency and group velocity.

## 5.4 Chapter Conclusions

We provide a generic theoretical framework to study the surface plasmon polariton (SPP) at the interface between topological insulator (TI) and layered superconductors. The SPP in this hybrid structure may be widely applied to study novel optical and transport phenomena at the interface, through the tunability of SPP propagation by gating or gapping the surface states of the TI. It can also be generalized to a larger category of materials in proximity to TI surface. For instance, Wei *et al.* [38] have shown that when the ferromagnetic insulator EuS is on the top of topological insulator $Bi_2Se_3$, it induces significant magnetic moment in $Bi_2Se_3$ thin films and induces breaking of T-reversal symmetry. The SPP in such Ferromagnetic- TI hybrid structure can also be studied within this approach.

Furthermore, Majorana zero mode is predicted to exist [28, 18, 149] as a domain wall state at the interface between TI and ferromagnetic-superconductor boundaries. Therefore, at the TI-layered superconductor interface, propagating SPP may interact with the Majorana domain wall state, and leads to the shift of the SPP propagation properties, including group velocity, reflectivity and transmissivity, etc. In this regards, the change of optical properties of SPP can be considered a semi-classical manifestation of the existence of Majorana fermions, which is a pure quantum phenomenon with non-Abelian statistics. The existence of the zero mode level may

contribute to electronic transition, and leads to a further change of dielectric functions. Unlike transport measurements, which involve only a single Majorana fermion domain wall state, this hybrid structure can be regarded as the interaction between SPP and a series of domain wall states, coming from each domain wall state along the interface. In a nutshell, the SPP on the TI surface may provide insights to the detection of Majorana Fermions as a conceptually novel platform.

# Appendix 1

$$H_{1x}^o = \frac{\kappa_1^o}{i\omega} E_{1y}^o,\ E_{1x}^o = -\frac{q_y}{q_x} E_{1y}^o,\ H_{1y}^o = -\frac{i\kappa_1^o q_y}{\omega q_x} E_{1y}^o$$

$$H_{1z}^o = \frac{q_x^2 + q_y^2}{\omega q_x} E_{1y}^o,\ H_{1x}^e = \frac{i\omega\varepsilon_{2D}(q,\omega)}{\kappa_1^e} E_{1y}^e,\ E_{1x}^e = \frac{q_x}{q_y} E_{1y}^e$$

$$H_{1y}^e = -\frac{i\omega q_x \varepsilon_{2D}(q,\omega)}{q_y \kappa_1^e} E_{1y}^e,\ E_{1z}^e = \left(\frac{i\kappa_1^e}{q_y} + \frac{i\omega^2 \varepsilon_{2D}(q,\omega)}{q_y \kappa_1^e}\right) E_{1y}^e$$

$$H_{2z}^o = \frac{q_x}{\omega\mu} E_{2y}^o,\ H_{2y}^o = \frac{i q_x q_y}{\omega\mu\kappa_2^o} E_{2y}^o,\ E_{2z}^o = -\frac{i q_y}{\kappa_2^o} E_{2y}^o$$

$$H_{2x}^o = \frac{q_y^2 - (\kappa_2^o)^2}{i\omega\mu\kappa_2^o} E_{2y}^o,\ E_{2z}^e = \frac{\kappa_2^e}{i q_y} E_{2y}^e,\ H_{2z}^e = \frac{\omega\varepsilon_{ab}(q,\omega)}{q_x} E_{2y}^e$$

$$H_{2y}^e = -\frac{\omega\varepsilon_{ab}(q,\omega)\kappa_2^e}{i q_x q_y} E_{2y}^e,\ E_{2x}^e = \frac{q_x^2 - \mu\omega^2\varepsilon_{ab}(q,\omega)}{q_x q_y} E_{2y}^e$$

# Appendix 2

Define $k^2 = k_x^2 + k_y^2$, $\delta^- = |\Delta| - M$ and $\delta^+ = |\Delta| + M$, the four eigenvectors can be written as:

$$\begin{aligned}
|f_{\mathbf{k},1}\rangle &= \left(-1, \frac{\delta^- + \sqrt{(\delta^-)^2 + k^2}}{ik_x + k_y}, -\frac{\delta^- + \sqrt{(\delta^-)^2 + k^2}}{ik_x + k_y}, 1\right)^T \\
|f_{\mathbf{k},2}\rangle &= \left(1, \frac{\delta^+ - \sqrt{(\delta^+)^2 + k^2}}{ik_x + k_y}, \frac{\delta^+ - \sqrt{(\delta^+)^2 + k^2}}{ik_x + k_y}, 1\right)^T \\
|f_{\mathbf{k},3}\rangle &= \left(-1, \frac{\delta^- - \sqrt{(\delta^-)^2 + k^2}}{ik_x + k_y}, \frac{-\delta^- + \sqrt{(\delta^-)^2 + k^2}}{ik_x + k_y}, 1\right)^T \\
|f_{\mathbf{k},4}\rangle &= \left(1, \frac{\delta^+ + \sqrt{(\delta^+)^2 + k^2}}{ik_x + k_y}, \frac{\delta^+ + \sqrt{(\delta^+)^2 + k^2}}{ik_x + k_y}, 1\right)^T
\end{aligned}$$

## Appendix 3: List of Publications

17. **Mingda Li**, Brian Kirby, Cuizu Chang, Ju Li* and Jagadeesh Moodera*, "Enhanced Proximity Effect with Possible Realization of Interfacial Spin Liquid ", to be submitted.

16. **Mingda Li***, Cuizu Chang*, Lijun Wu, Jing Tao, Weiwei Zhao, Moses Chan, Jagadeesh Moodera, Ju Li and Yimei Zhu*, "Experimental Verification of Van Vleck Nature of Long-Range Ferromagnetic Order in Vanadium-Doped Three-Dimensional Topological Insulator $Sb_2Te_3$". *Phys. Rev. Lett.* **114**, 146802 (2015), As **Corresponding Author**.

15. **Mingda Li***, Wenping Cui, Jin Yu, Zuyang Dai, Zhe Wang, Ferhat Katmis, Wanlin Guo and Jagadeesh Moodera, "Magnetic Proximity Effect and Interlayer Exchange Coupling of Ferromagnetic / Topological Insulator / Ferromagnetic Trilayer", *Phys. Rev. B* **91**, 014427 (2015), As **Corresponding Author**.

14. Asli Ugur, Ferhat Katmis, **Mingda Li**, Lijun Wu, Yimei Zhu, Kripa Varanasi, Karen Gleason*, "Unraveling Conduction Mechanisms in Nanocrystalline Conjugated Polymers", submitted to *Science*.

13. **Mingda Li*,** Zuyang Dai, Wenping Cui, Zhe Wang, Ferhat Katmis, Peisi Le, Jiayue Wang, Lijun Wu and Yimei Zhu, "Tunable THz Surface Plasmonics based on Topological Insulator-Layered Superconductor Hybrid Structure", *Phys. Rev. B* **89**, 235432 (2014)**,** As **Corresponding Author**.

12. Zhe Wang, Emiliano Fratini, **Mingda Li**, Peisi Le, Eugene Manontov, Piero Baglioni, Sow-Hsin Chen, "Hydration-dependent dynamic crossover

phenomenon in protein hydration water", *Phys. Rev. E* **90**, 042705 (2014).

11. **Mingda Li*,** Wenping Cui, Lijun Wu, Qingping Meng, Yimei Zhu, Yong Zhang, Weishu Liu and Zhifeng Ren, "Topological Effect to Surface Plasmon Excitation in Topological Insulator Nanowires". *Can. J. Phys.* 10.1139/cjp-2014-0418 (2014). As **Corresponding Author**.

10. Junjie Niu, Akihiro Kushima, **Mingda Li**, Wenbin Li, Ziqiang Wang and Ju Li*, "Scalable Synthesis of Sulfur Nanosponge Cathode for Lithium-Sulfur Battery with Greatly Improved Cyclability", *J. Mater. Chem. A* **2**, 19788-19796 (2014).

09. Wenping Cui, **Mingda Li***, Zuyang Dai, Qingping Meng and Yimei Zhu, , "Near-Field Optical Effect of a Core-Shell Nanostructure In Proximity to a Flat Surface", *J. Chem. Phys.*, **140**, 044109 (2014) . As **Corresponding Author**.

08. Zhe Wang, Wei-Shan Chiang, Peisi Le, Emiliano Fratini, **Mingda Li**, Ahmet Alatas, Piero Baglionib and Sow-Hsin Chen*, "One role of hydration water in proteins: key to the 'softening' of short time intraprotein collective vibrations of a specific length scale", *Soft Matter*, **10**, 4298 (2014).

07. Zhiting Tian*, **Mingda Li***, Zhensong Ren, Hao Ma, Ahmet Alatas, Stephen Wilson, "Investigation of phonon transport in PbTe-PbSe alloys using inelastic x-ray scattering", submitted to *Appl. Phys. Lett.* As **Co-Corresponding Author**.

06. Zhe Wang, Kao-Hsiang Liu, Peisi Le, **Mingda Li**, Wei-Shan Chiang, Juscelino Leao, Madhusudan Tyagi, John R.D. Copley, Andrey Podlesnyak, Alexander I. Kolesnikov, Chung-Yuan Mou, and Sow-Hsin Chen*, "Boson peak in deeply-cooled confined water: A possible way to explore the existence of the liquid-to-liquid transition in water", *Phys. Rev. Lett.,* **112**, 237802 (2014).

05. Albert D. Liao, Mengliang Yao, Ferhat Katmis, **Mingda Li**, Shuang Tang, Jagadeesh Moodera, Cyril Opeil, and Mildred Dresselhaus, "Inducing Anisotropic Electronic Transport in Bismuth Thin Films", *Appl. Phys. Lett.* **105**, 063114 (2014).

04. Sergey Paltsev, Frank O' Sullivan, Nathan Lee, Anna Agarwal, **Mingda Li**, X. Li, N. Fylaktos (2013), "Natural Gas Monetization Pathways for Cyprus: Interim Report - Economics of Project Development Options", MIT Energy Initiative, Massachusetts Institute of Technology, Cambridge, MA. ISBN 978-0-9828008-8-1.

03. **Mingda Li**, Xiang-qiang Chu, Emiliano Fratini, Piero Baglioni, Ahmet Alatas, E. Ercan Alp, Sow-Hsin Chen*, "Phonon-like excitation in secondary and tertiary structure of hydrated protein powders", *Soft Matter,* **7**, 9848-9853 (2011) .

02. Cheng-Si Tsao, **Mingda Li**, Yang Zhang, Juscelino B. Leao, Wei-Shan Chiang, Tsui-Yun Chung, Yi-Ren Tzeng, Ming-Sheng Yu, and Sow-Hsin Chen*, "Probing the Room Temperature Spatial Distribution of Hydrogen in Nanoporous Carbon by Use of Small-Angle Neutron Scattering", *J. Phys. Chem. C*, **114**, 19895 (2010) .

01. Cheng-Si Tsao, Yun Liu, **Mingda Li**, Yang Zhang, Juscelino B. Leao, Hua-Wen Chang, Ming-Sheng Yu and Sow-Hsin Chen*, "Neutron Scattering Methodology for Absolute Measurement of Room-Temperature Hydrogen Storage Capacity and Evidence for Spillover Effect in a Pt-Doped Activated Carbon", *J. Phys. Chem. Lett.* **1,** 1569-1573 (2010).

# Bibliography


[1] M. Z. Hasan and C. L. Kane. Colloquium: Topological insulators. Reviews of Modern Physics, 82(4):3045–3067, 2010.

[2] Yasuhiro Hatsugai. Chern number and edge states in the integer quantum hall effect. Phys. Rev. Lett., 71:3697–3700, Nov 1993.

[3] J. E. Moore and L. Balents. Topological invariants of time-reversal-invariant band structures. Phys. Rev. B, 75:121306, Mar 2007.

[4] Haijun Zhang, Chao-Xing Liu, Xiao-Liang Qi, Xi Dai, Zhong Fang, and Shou-Cheng Zhang. Topological insulators in bi2se3, bi2te3 and sb2te3 with a single dirac cone on the surface. Nature physics, 5(6):438–442, 2009.

[5] Alexander Altland and Martin R. Zirnbauer. Nonstandard symmetry classes in mesoscopic normal-superconducting hybrid structures. Phys. Rev. B, 55:1142–1161, Jan 1997.

[6] Shinsei Ryu, Andreas P Schnyder, Akira Furusaki, and Andreas W W Ludwig. Topological insulators and superconductors: tenfold way and dimensional hierarchy. New Journal of Physics, 12(6):065010, 2010.

[7] Andreas P. Schnyder, Shinsei Ryu, Akira Furusaki, and Andreas W. W. Ludwig. Classification of topological insulators and superconductors in three spatial dimensions. Phys. Rev. B, 78:195125, Nov 2008.

[8] Andreas P. Schnyder, Shinsei Ryu, Akira Furusaki, and Andreas W. W. Ludwig.

Classification of topological insulators and superconductors. AIP Conference Proceedings, 1134(1), 2009.

[9] D. Hsieh, Y. Xia, D. Qian, L. Wray, F. Meier, J. H. Dil, J. Osterwalder, L. Patthey, A. V. Fedorov, H. Lin, A. Bansil, D. Grauer, Y. S. Hor, R. J. Cava, and M. Z. Hasan. Observation of time-reversal-protected single-dirac-cone topological-insulator states in $bi_2te_3$ and $sb_2te_3$. Phys. Rev. Lett., 103:146401, Sep 2009.

[10] D. Hsieh, Y. Xia, D. Qian, L. Wray, J. H. Dil, F. Meier, J. Osterwalder, L. Patthey, J. G. Checkelsky, N. P. Ong, A. V. Fedorov, H. Lin, A. Bansil, D. Grauer, Y. S. Hor, R. J. Cava, and M. Z. Hasan. A tunable topological insulator in the spin helical dirac transport regime. Nature, 460(7259):1101–1105, 2009. 10.1038/nature08234.

[11] Y. L. Chen, J. G. Analytis, J.-H. Chu, Z. K. Liu, S.-K. Mo, X. L. Qi, H. J. Zhang, D. H. Lu, X. Dai, Z. Fang, S. C. Zhang, I. R. Fisher, Z. Hussain, and Z.-X. Shen. Experimental realization of a three-dimensional topological insulator, bi2te3. Science, 325(5937):178–181, 2009.

[12] Yi Zhang, Ke He, Cui-Zu Chang, Can-Li Song, Li-Li Wang, Xi Chen, Jin-Feng Jia, Zhong Fang, Xi Dai, Wen-Yu Shan, Shun-Qing Shen, Qian Niu, Xiao-Liang Qi, Shou-Cheng Zhang, Xu-Cun Ma, and Qi-Kun Xue. Crossover of the three-dimensional topological insulator bi2se3 to the two-dimensional limit. Nat Phys, 6(8):584–588, 2010. 10.1038/nphys1689.

[13] D. Hsieh, Y. Xia, L. Wray, D. Qian, A. Pal, J. H. Dil, J. Osterwalder, F. Meier, G. Bihlmayer, C. L. Kane, Y. S. Hor, R. J. Cava, and M. Z. Hasan. Observation of unconventional quantum spin textures in topological insulators. Science, 323(5916):919–922, 2009.

[14] L. A. Wray, S. Xu, M. Neupane, A. V. Fedorov, Y. S. Hor, R. J. Cava, and M. Z. Hasan. Chemically gated electronic structure of a superconducting doped

topological insulator system. 10th International Conference on Materials and Mechanisms of Superconductivity (M2s-X), 449, 2013.

[15] L Andrew Wray. Device physics: Topological transistor. Nature Physics, 8(10):705–706, 2012.

[16] Dmytro Pesin and Allan H. MacDonald. Spintronics and pseudospintronics in graphene and topological insulators. Nat Mater, 11(5):409–416, 2012. 10.1038/nmat3305.

[17] Ivana Vobornik, Unnikrishnan Manju, Jun Fujii, Francesco Borgatti, Piero Torelli, Damjan Krizmancic, Yew San Hor, Robert J Cava, and Giancarlo Panaccione. Magnetic proximity effect as a pathway to spintronic applications of topological insulators. Nano letters, 11(10):4079–4082, 2011.

[18] Liang Fu and Charles L Kane. Superconducting proximity effect and majorana fermions at the surface of a topological insulator. Physical Review Letters, 100(9):096407, 2008.

[19] A. R. Akhmerov, Johan Nilsson, and C. W. J. Beenakker. Electrically detected interferometry of majorana fermions in a topological insulator. Phys. Rev. Lett., 102:216404, May 2009.

[20] Yukio Tanaka, Takehito Yokoyama, and Naoto Nagaosa. Manipulation of the majorana fermion, andreev reflection, and josephson current on topological insulators. Phys. Rev. Lett., 103:107002, Sep 2009.

[21] Jay D. Sau, Roman M. Lutchyn, Sumanta Tewari, and S. Das Sarma. Generic new platform for topological quantum computation using semiconductor heterostructures. Phys. Rev. Lett., 104:040502, Jan 2010.

[22] C.W.J. Beenakker. Search for majorana fermions in superconductors. Annual Review of Condensed Matter Physics, 4(1):113–136, 2013.

[23] Weidong Luo and Xiao-Liang Qi. Massive dirac surface states in topological insulator/magnetic insulator heterostructures. Physical Review B, 87(8), 2013.

[24] R. D. Li, J. Wang, X. L. Qi, and S. C. Zhang. Dynamical axion field in topological magnetic insulators. Nature Physics, 6(4):284–288, 2010.

[25] X. L. Qi, R. D. Li, J. D. Zang, and S. C. Zhang. Inducing a magnetic monopole with topological surface states. Science, 323(5918):1184–1187, 2009.

[26] Qin Liu, Chao-Xing Liu, Cenke Xu, Xiao-Liang Qi, and Shou-Cheng Zhang. Magnetic impurities on the surface of a topological insulator. Physical review letters, 102(15):156603, 2009.

[27] X. L. Qi, T. L. Hughes, and S. C. Zhang. Topological field theory of time-reversal invariant insulators. Physical Review B, 78(19):195424, 2008.

[28] X. L. Qi and S. C. Zhang. Topological insulators and superconductors. Reviews of Modern Physics, 83(4):1057. 006NK ISSN = 0034-6861, DOI = DOI 10.1103/RevModPhys.83.1057, url = <Go to ISI>://WOS:000308825700001, year = 2011, type = Journal Article.

[29] V. Men'shov, V. Tugushev, S. Eremeev, P. Echenique, and E. Chulkov. Magnetic proximity effect in the three-dimensional topological insulator/ferromagnetic insulator heterostructure. Physical Review B, 88(22), 2013.

[30] M. Lang, M. Montazeri, M. C. Onbasli, X. Kou, Y. Fan, P. Upadhyaya, K. Yao, F. Liu, Y. Jiang, W. Jiang, K. L. Wong, G. Yu, J. Tang, T. Nie, L. He, R. N. Schwartz, Y. Wang, C. A. Ross, and K. L. Wang. Proximity induced high-temperature magnetic order in topological insulator - ferrimagnetic insulator heterostructure. Nano Lett, 2014.

[31] Xiaodong Li, Yuriy G Semenov, and Ki Wook Kim. Thz detector based on proximity effect of topological insulator. In Device Research Conference (DRC), 2012 70th Annual, pages 111–112. IEEE, 2012.

[32] Qi-Kun Xue. Nanoelectronics: A topological twist for transistors. Nature nanotechnology, 6(4):197–198, 2011.

[33] C. Z. Chang, J. Zhang, X. Feng, J. Shen, Z. Zhang, M. Guo, K. Li, Y. Ou, P. Wei, L. L. Wang, Z. Q. Ji, Y. Feng, S. Ji, X. Chen, J. Jia, X. Dai, Z. Fang, S. C. Zhang, K. He, Y. Wang, L. Lu, X. C. Ma, and Q. K. Xue. Experimental observation of the quantum anomalous hall effect in a magnetic topological insulator. Science, 340(6129):167–70, 2013.

[34] Qi-Kun Xue. Preface to the special topic on topological insulators. National Science Review, 1(1):31–31, 2014.

[35] Jing Wang, Biao Lian, Haijun Zhang, Yong Xu, and Shou-Cheng Zhang. Quantum anomalous hall effect with higher plateaus. Physical Review Letters, 111(13), 2013.

[36] R. Yu, W. Zhang, H. J. Zhang, S. C. Zhang, X. Dai, and Z. Fang. Quantized anomalous hall effect in magnetic topological insulators. Science, 329(5987):61–4, 2010.

[37] B Andrei Bernevig. Topological Insulators and Topological Superconductors. Princeton University Press, 2013.

[38] P. Wei, F. Katmis, B. A. Assaf, H. Steinberg, P. Jarillo-Herrero, D. Heiman, and J. S. Moodera. Exchange-coupling-induced symmetry breaking in topological insulators. Physical Review Letters, 110(18), 2013.

[39] Vladimir Nikolaevich MenâĂŹshov, Viktor Vital'evich Tugushev, and Evgenii Vladimirovich Chulkov. Engineering near-surface electron states in three-dimensional topological insulators. JETP letters, 98(10):603–608, 2014.

[40] SV Eremeev, VN Men'shov, VV Tugushev, PM Echenique, and EV Chulkov. Magnetic proximity effect at the three-dimensional topological insulator/magnetic insulator interface. Physical Review B, 88(14):144430, 2013.

[41] Vladimir Nikolaevich MenâĂŹshov, Viktor Vital'evich Tugushev, and Evgenii Vladimirovich Chulkov. Interface-induced states at the boundary between a 3d topological insulator and a normal insulator. JETP letters, 97(5):258–264, 2013.

[42] Vladimir Nikolaevich MenâĂŹshov, Viktor Vital'evich Tugushev, and Evgenii Vladimirovich Chulkov. Bound states induced by a ferromagnetic delta-layer inserted into a three-dimensional topological insulator. JETP letters, 96(7):445–451, 2012.

[43] Zilong Jiang, Ferhat Katmis, Chi Tang, Peng Wei, Jagadeesh S. Moodera, and Jing Shi. A comparative transport study of bi2se3 and bi2se3/yttrium iron garnet. Applied Physics Letters, 104(22):–, 2014.

[44] Vladimir Nikolaevich MenâĂŹshov, Viktor Vital'evich Tugushev, and Evgenii Vladimirovich Chulkov. Carrier mediated ferromagnetism on the surface of a topological insulator. JETP Letters, 94(8):629–634, 2011.

[45] C. Z. Chang, A.B. Chang, C. D. Chang, E.F. Chang, G.H. Chang, G.H. Chang, G.H. Chang, G.H. Chang, G.H. Chang, G.H. Chang, and G.H. Chang. Nat. Mater., 25:1065, 2014.

[46] K. He, Y. Wang, and Q. K. Xue. Quantum anomalous hall effect. National Science Review, 1(1):38–48, 2013.

[47] O. V. Yazyev, J. E. Moore, and S. G. Louie. Spin polarization and transport of surface states in the topological insulators bi2se3 and bi2te3 from first principles. Physical Review Letters, 105(26):266806, 2010.

[48] F. X. Xiu, L. A. He, Y. Wang, L. N. Cheng, L. T. Chang, M. R. Lang, G. A. Huang, X. F. Kou, Y. Zhou, X. W. Jiang, Z. G. Chen, J. Zou, A. Shailos, and K. L. Wang. Manipulating surface states in topological insulator nanoribbons. Nature Nanotechnology, 6(4):216–221, 2011.

[49] Varley F. Sears. Neutron scattering lengths and cross sections. Neutron News, 3(3):26–37, 1992.

[50] P. Bruno and C. Chappert. Ruderman-kittel theory of oscillatory interlayer exchange coupling. Physical Review B, 46(1):261–270, 1992.

[51] P. M. Levy, S. Maekawa, and P. Bruno. Range dependence of interlayer exchange coupling. Physical Review B, 58(9):5588–5593, 1998.

[52] U. RÃijcker, S. O. Demokritov, J. Nassar, and P. GrÃijnberg. Magnetic interlayer coupling across semiconducting eus layers. Europhysics Letters (EPL), 66(5):736–742, 2004.

[53] Jae-Ho Han and Hyun-Woo Lee. Interlayer exchange coupling between next nearest neighbor layers. Physical Review B, 86(17), 2012.

[54] S. R. Spurgeon, J. D. Sloppy, D. M. Kepaptsoglou, P. V. Balachandran, S. Nejati, J. Karthik, A. R. Damodaran, C. L. Johnson, H. Ambaye, R. Goyette, V. Lauter, Q. M. Ramasse, J. C. Idrobo, K. K. S. Lau, S. E. Lofland, J. M. Rondinelli, L. W. Martin, and M. L. Taheri. Thickness-dependent crossover from charge- to strain-mediated magnetoelectric coupling in ferromagnetic/piezoelectric oxide heterostructures. Acs Nano, 8(1):894–903, 2014.

[55] Y. G. Semenov, X. P. Duan, and K. W. Kim. Voltage-driven magnetic bifurcations in nanomagnet-topological insulator heterostructures. Physical Review B, 89(20), 2014.

[56] V. Lauter, H. Ambaye, R. Goyette, W. T. H. Lee, and A. Parizzi. Highlights from the magnetism reflectometer at the sns. Physica B-Condensed Matter, 404(17):2543–2546, 2009.

[57] M. Bjorck and G. Andersson. Genx: an extensible x-ray reflectivity refinement program utilizing differential evolution. Journal of Applied Crystallography, 40:1174–1178, 2007.

[58] David L. Goodstein. States of matter. Dover, New York, dover edition, 1985.

[59] Nicola A. Spaldin. Magnetic materials : fundamentals and applications. Cambridge University Press, Cambridge ; New York, 2nd edition, 2011.

[60] P. Quinet and E. Biemont. Lande g-factors for experimentally determined energy levels in doubly ionized lanthanides. Atomic Data and Nuclear Data Tables, 87(2):207–230, 2004.

[61] Tiffany S. Santos. Europium oxide as a perfect electron spin filter. Thesis, 2007.

[62] Takehito Yokoyama and Yaroslav Tserkovnyak. Spin diffusion and magnetoresistance in ferromagnet/topological-insulator junctions. Physical Review B, 89(3), 2014.

[63] A. Karch. Surface plasmons and topological insulators. Physical Review B, 83(24):245432, 2011.

[64] J. F. Tian, C. Z. Chang, H. L. Cao, K. He, X. C. Ma, Q. K. Xue, and Y. P. Chen. Quantum and classical magnetoresistance in ambipolar topological insulator transistors with gate-tunable bulk and surface conduction. Scientific Reports, 4:4859, 2014.

[65] D. Kim, S. Cho, N. P. Butch, P. Syers, K. Kirshenbaum, S. Adam, J. Paglione, and M. S. Fuhrer. Surface conduction of topological dirac electrons in bulk insulating bi2se3. Nature Physics, 8(6):459–463, 2012.

[66] Chih-wen Chen. Magnetism and metallurgy of soft magnetic materials. Dover Publications, New York, 1986.

[67] M. S. Bahramy, P. D. King, A. de la Torre, J. Chang, M. Shi, L. Patthey, G. Balakrishnan, P. Hofmann, R. Arita, N. Nagaosa, and F. Baumberger. Emergent quantum confinement at topological insulator surfaces. Nat Commun, 3:1159, 2012.

[68] C. A. Hoffman, J. R. Meyer, F. J. Bartoli, A. Divenere, X. J. Yi, C. L. Hou, H. C. Wang, J. B. Ketterson, and G. K. Wong. Semimetal-to-semiconductor transition in bismuth thin-films. Physical Review B, 48(15):11431, 1993.

[69] Xiaodong Li, Xiaopeng Duan, and Ki Wook Kim. Controlling electron propagation on a topological insulator surface via proximity interactions. Physical Review B, 89(4):045425, 2014.

[70] Patrick Bruno. Theory of interlayer exchange interactions in magnetic multilayers. Journal of Physics: Condensed Matter, 11(48):9403, 1999.

[71] P Bruno. Interlayer exchange coupling: The role of electron confinement in the overlayer due to the vacuum barrier. Journal of magnetism and magnetic materials, 164(1):27–36, 1996.

[72] P Bruno. Theory of interlayer magnetic coupling. Physical Review B, 52(1):411, 1995.

[73] E Bruno and BL Gyorffy. Geometrical resonance in magnetic multilayers. Physical review letters, 71(1):181, 1993.

[74] P Bruno. Interlayer exchange coupling: a unified physical picture. Journal of magnetism and magnetic materials, 121(1):248–252, 1993.

[75] Patrick Bruno. Tight-binding approach to the orbital magnetic moment and magnetocrystalline anisotropy of transition-metal monolayers. Physical Review B, 39(1):865, 1989.

[76] Robert M White. Quantum theory of magnetism: magnetic properties of materials, volume 32. Springer, 2007.

[77] Chao-Xing Liu, Xiao-Liang Qi, HaiJun Zhang, Xi Dai, Zhong Fang, and Shou-Cheng Zhang. Model hamiltonian for topological insulators. Physical Review B, 82(4):045122, 2010.

[78] SV Eremeev, VN Men'shov, VV Tugushev, and EV Chulkov. Interface induced states at the boundary between a 3d topological insulator bi _2 se _3 and a ferromagnetic insulator eus. arXiv preprint arXiv:1407.6880, 2014.

[79] Jochen Kienert. Ferromagnetism and interlayer exchange couplingin thin metallic ïňĄlms. PhD thesis, Humboldt University of Berlin, July 2008.

[80] FA Buot and JW McClure. Theory of diamagnetism of bismuth. Physical Review B, 6(12):4525, 1972.

[81] JE Hebborn and NH March. Conduction electron diamagnetism in alloys and magnetic-field-dependent dielectric constant of a fermi gas. Proceedings of the Royal Society of London. Series A. Mathematical and Physical Sciences, 280(1380):85–96, 1964.

[82] Laurent-Patrick Levy. Magnetism and Superconductivity. Springer, 2000.

[83] JE Hebborn and NH March. Orbital and spin magnetism and dielectric response of electrons in metals. Advances in Physics, 19(78):175–215, 1970.

[84] Francesco Mauri and Steven G. Louie. Magnetic susceptibility of insulators from first principles. Phys. Rev. Lett., 76:4246–4249, May 1996.

[85] Mikito Koshino and Tsuneya Ando. Anomalous orbital magnetism in dirac-electron systems: Role of pseudospin paramagnetism. Phys. Rev. B, 81:195431, May 2010.

[86] Lukas Zhao, Haiming Deng, Inna Korzhovska, Zhiyi Chen, Marcin Konczykowski, Andrzej Hruban, Vadim Oganesyan, and Lia Krusin-Elbaum. Singular robust room-temperature spin response from topological dirac fermions. Nature materials, 13:580, 2014.

[87] M Kumar. Diamagnetic Susceptibility and Anisotropy of Inorganic and Organometallic Compounds, volume 27. Springer, 2007.

[88] M. N. Baibich, J. M. Broto, A. Fert, F. Nguyen Van Dau, F. Petroff, P. Etienne, G. Creuzet, A. Friederich, and J. Chazelas. Giant magnetoresistance of (001)fe/(001)cr magnetic superlattices. Phys. Rev. Lett., 61:2472–2475, Nov 1988.

[89] A. Fert, P. GrÃijnberg, A. BarthÃľlÃľmy, F. Petroff, and W. Zinn. Layered magnetic structures: interlayer exchange coupling and giant magnetoresistance. Journal of Magnetism and Magnetic Materials, 140âĂŞ144, Part 1(0):1 – 8, 1995. International Conference on Magnetism.

[90] S. S. P. Parkin, N. More, and K. P. Roche. Oscillations in exchange coupling and magnetoresistance in metallic superlattice structures: Co/ru, co/cr, and fe/cr. Phys. Rev. Lett., 64:2304–2307, May 1990.

[91] S. S. P. Parkin, R. Bhadra, and K. P. Roche. Oscillatory magnetic exchange coupling through thin copper layers. Phys. Rev. Lett., 66:2152–2155, Apr 1991.

[92] Cui-Zu Chang, Peng Wei, and Jagadeesh S. Moodera. Breaking time reversal symmetry in topological insulators. MRS Bulletin, 39(10):867–872, 2014.

[93] Chao-Xing Liu, Xiao-Liang Qi, Xi Dai, Zhong Fang, and Shou-Cheng Zhang. Quantum anomalous hall effect in hg1-ymnyte quantum wells. Physical Review Letters, 101(14):146802, 2008.

[94] X. F. Kou, S. T. Guo, Y. B. Fan, L. Pan, M. R. Lang, Y. Jiang, Q. M. Shao, T. X. Nie, K. Murata, J. S. Tang, Y. Wang, L. He, T. K. Lee, W. L. Lee, and K. L. Wang. Scale-invariant quantum anomalous hall effect in magnetic topological insulators beyond the two-dimensional limit. Physical Review Letters, 113(13):137201, 2014.

[95] J. G. Checkelsky, R. Yoshimi, A. Tsukazaki, K. S. Takahashi, Y. Kozuka, J. Falson, M. Kawasaki, and Y. Tokura. Trajectory of the anomalous hall effect towards the quantized state in a ferromagnetic topological insulator. Nature Physics, 10(10):731–736, 2014.

[96] A. M. Essin, J. E. Moore, and D. Vanderbilt. Magnetoelectric polarizability and axion electrodynamics in crystalline insulators (vol 102, 146805, 2009). Physical Review Letters, 103(25):146805, 2009.

[97] P. Larson and W. R. L. Lambrecht. Electronic structure and magnetism in bi2te3, bi2se3, and sb2te3 doped with transition metals (ti-zn). Physical Review B, 78(19), 2008.

[98] M. G. Vergniory, M. M. Otrokov, D. Thonig, M. Hoffmann, I. V. Maznichenko, M. Geilhufe, X. Zubizarreta, S. Ostanin, A. Marmodoro, J. Henk, W. Hergert, I. Mertig, E. V. Chulkov, and A. Ernst. Exchange interaction and its tuning in magnetic binary chalcogenides. Physical Review B, 89(16), 2014.

[99] S. Y. Xu, M. Neupane, C. Liu, D. M. Zhang, A. Richardella, L. A. Wray, N. Alidoust, M. Leandersson, T. Balasubramanian, J. Sanchez-Barriga, O. Rader, G. Landolt, B. Slomski, J. H. Dil, J. Osterwalder, T. R. Chang, H. T. Jeng, H. Lin, A. Bansil, N. Samarth, and M. Z. Hasan. Hedgehog spin texture and berry's phase tuning in a magnetic topological insulator. Nature Physics, 8(8):616–622, 2012.

[100] Y. L. Chen, J. H. Chu, J. G. Analytis, Z. K. Liu, K. Igarashi, H. H. Kuo, X. L. Qi, S. K. Mo, R. G. Moore, D. H. Lu, M. Hashimoto, T. Sasagawa, S. C. Zhang, I. R. Fisher, Z. Hussain, and Z. X. Shen. Massive dirac fermion on the surface of a magnetically doped topological insulator. Science, 329(5992):659–662, 2010.

[101] Y. S. Hor, P. Roushan, H. Beidenkopf, J. Seo, D. Qu, J. G. Checkelsky, L. A. Wray, D. Hsieh, Y. Xia, S. Y. Xu, D. Qian, M. Z. Hasan, N. P. Ong, A. Yazdani, and R. J. Cava. Development of ferromagnetism in the doped topological insulator bi2-xmnxte3. Physical Review B, 81(19):195203, 2010.

[102] C. Z. Chang, P. Z. Tang, Y. L. Wang, X. Feng, K. Li, Z. C. Zhang, Y. Y. Wang, L. L. Wang, X. Chen, C. X. Liu, W. H. Duan, K. He, X. C. Ma, and Q. K. Xue. Chemical-potential-dependent gap opening at the dirac surface states of

bi2se3 induced by aggregated substitutional cr atoms. Physical Review Letters, 112(5):056801, 2014.

[103] C. Z. Chang, J. S. Zhang, M. H. Liu, Z. C. Zhang, X. Feng, K. Li, L. L. Wang, X. Chen, X. Dai, Z. Fang, X. L. Qi, S. C. Zhang, Y. Y. Wang, K. He, X. C. Ma, and Q. K. Xue. Thin films of magnetically doped topological insulator with carrier-independent long-range ferromagnetic order. Advanced Materials, 25(7):1065–1070, 2013.

[104] H. Ohno, D. Chiba, F. Matsukura, T. Omiya, E. Abe, T. Dietl, Y. Ohno, and K. Ohtani. Electric-field control of ferromagnetism. Nature, 408(6815):944–946, 2000.

[105] T. Dietl. A ten-year perspective on dilute magnetic semiconductors and oxides. Nature Materials, 9(12):965–974, 2010.

[106] J. W. Liu, T. H. Hsieh, P. Wei, W. H. Duan, J. Moodera, and L. Fu. Spin-filtered edge states with an electrically tunable gap in a two-dimensional topological crystalline insulator. Nature Materials, 13(2):178–183, 2014.

[107] J. J. Rehr, J. J. Kas, M. P. Prange, A. P. Sorini, Y. Takimoto, and F. Vila. Ab initio theory and calculations of x-ray spectra. Comptes Rendus Physique, 10(6):548–559, 2009.

[108] K. Jorissen, J. J. Rehr, and J. Verbeeck. Multiple scattering calculations of relativistic electron energy loss spectra. Physical Review B, 81(15):155108, 2010.

[109] J. J. Rehr, J. J. Kas, F. D. Vila, M. P. Prange, and K. Jorissen. Parameter-free calculations of x-ray spectra with feff9. Physical Chemistry Chemical Physics, 12(21):5503–5513, 2010.

[110] R. F. Egerton. Electron energy-loss spectroscopy in the electron microscope. The language of science. Plenum Press, New York, 2nd edition.

[111] M. S. Dresselhaus, G. Dresselhaus, and A. Jorio. Group theory : application to the physics of condensed matter. Springer-Verlag, Berlin, 2008.

[112] J. S. Dyck, P. Hajek, P. Losit'ak, and C. Uher. Diluted magnetic semiconductors based on sb2-xvxte3 (0.01 <= x <= 0.03). Physical Review B, 65(11), 2002.

[113] JM Pitarke, VM Silkin, EV Chulkov, and PM Echenique. Theory of surface plasmons and surface-plasmon polaritons. Reports on progress in physics, 70(1):1, 2007.

[114] Stefan Alexander Maier. Plasmonics: Fundamentals and Applications: Fundamentals and Applications. Springer, 2007.

[115] M. L. Brongersma and P. G (Eds.) Kik. Surface Plasmon Nanophotonics. Springer Series in Optical Sciences Vol. 131, edited by PG Kik and ML Brongersma. Springer, Dordrecht, 2007.

[116] Satoshi Kawata. Near-field optics and surface plasmon polaritons, volume 20. Springer, 2001.

[117] Wenping Cui, Mingda Li, Zuyang Dai, Qingping Meng, and Yimei Zhu. Near-field optical effect of a core-shell nanostructure in proximity to a flat surface. The Journal of Chemical Physics, 140(4):044109, 2014.

[118] Jiri Homola. Surface plasmon resonance based sensors, volume 4. Springer, 2006.

[119] Jan Becker. Plasmons as sensors. Springer, 2012.

[120] Tomáš Váry and Peter Markoš. Propagation of surface plasmon polaritons through gradient index and periodic structures. Opto-Electronics Review, 18(4):400–407, 2010.

[121] B Wunsch, T Stauber, F Sols, and F Guinea. Dynamical polarization of graphene at finite doping. New Journal of Physics, 8(12):318, 2006.

[122] E. H. Hwang and S DasSarma. Dielectric function, screening, and plasmons in two-dimensional graphene. Physical Review B, 75(20):205418, 2007.

[123] Marinko Jablan, Hrvoje Buljan, and Marin Soljačić. Plasmonics in graphene at infrared frequencies. Physical review B, 80(24):245435, 2009.

[124] Long Ju, Baisong Geng, Jason Horng, Caglar Girit, Michael Martin, Zhao Hao, Hans A Bechtel, Xiaogan Liang, Alex Zettl, Y Ron Shen, et al. Graphene plasmonics for tunable terahertz metamaterials. Nature nanotechnology, 6(10):630–634, 2011.

[125] Frank HL Koppens, Darrick E Chang, and F Javier Garcia de Abajo. Graphene plasmonics: a platform for strong light–matter interactions. Nano letters, 11(8):3370–3377, 2011.

[126] Hugen Yan, Fengnian Xia, Zhiqiang Li, and Phaedon Avouris. Plasmonics of coupled graphene micro-structures. New Journal of Physics, 14(12):125001, 2012.

[127] AN Grigorenko, Marco Polini, and KS Novoselov. Graphene plasmonics. Nature photonics, 6(11):749–758, 2012.

[128] Stefan A Maier. Graphene plasmonics: All eyes on flatland. Nature Physics, 8(8):581–582, 2012.

[129] Qiaoliang Bao and Kian Ping Loh. Graphene photonics, plasmonics, and broadband optoelectronic devices. ACS nano, 6(5):3677–3694, 2012.

[130] Philippe Tassin, Thomas Koschny, Maria Kafesaki, and Costas M Soukoulis. A comparison of graphene, superconductors and metals as conductors for metamaterials and plasmonics. Nature Photonics, 6(4):259–264, 2012.

[131] Victor W Brar, Min Seok Jang, Michelle Sherrott, Josue J Lopez, and Harry A Atwater. Highly confined tunable mid-infrared plasmonics in graphene nanoresonators. Nano letters, 13(6):2541–2547, 2013.

[132] Dafei Jin, Anshuman Kumar, Kin Hung Fung, Jun Xu, and Nicholas X Fang. Terahertz plasmonics in ferroelectric-gated graphene. Applied Physics Letters, 102(20):201118, 2013.

[133] Wei Bing Lu, Wei Zhu, Hong Ju Xu, Zhen Hua Ni, Zheng Gao Dong, and Tie Jun Cui. Flexible transformation plasmonics using graphene. Optics express, 21(9):10475–10482, 2013.

[134] Hrvoje Buljan, Marinko Jablan, and Marin Soljačić. Graphene plasmonics: Damping of plasmons in graphene. Nature Photonics, 7(5):346–348, 2013.

[135] P. Avouris and M. Freitag. Graphene photonics, plasmonics, and optoelectronics. Selected Topics in Quantum Electronics, IEEE Journal of, 20(1):72–83, Jan 2014.

[136] Dmitry K Efimkin, Yurii E Lozovik, and Alexey A Sokolik. Collective excitations on a surface of topological insulator. Nanoscale research letters, 7(1):1–10, 2012.

[137] DK Efimkin, Yu E Lozovik, and AA Sokolik. Spin-plasmons in topological insulator. Journal of Magnetism and Magnetic Materials, 324(21):3610–3612, 2012.

[138] O Roslyak, Godfrey Gumbs, and Danhong Huang. Plasmons in single-and double-component helical liquids: Application to two-dimensional topological insulators. Physical Review B, 87(4):045121, 2013.

[139] Robert Schütky, Christian Ertler, Andreas Trügler, and Ulrich Hohenester. Surface plasmons in doped topological insulators. Physical Review B, 88(19):195311, 2013.

[140] P Di Pietro, M Ortolani, O Limaj, A Di Gaspare, V Giliberti, F Giorgianni, M Brahlek, N Bansal, N Koirala, S Oh, et al. Observation of dirac plasmons in a topological insulator. Nature nanotechnology, 8(8):556–560, 2013.

[141] Yoshinori Okada and Vidya Madhavan. Topological insulators: Plasmons at the surface. Nature nanotechnology, 8(8):541–542, 2013.

[142] T Stauber, G Gómez-Santos, and L Brey. Spin-charge separation of plasmonic excitations in thin topological insulators. Physical Review B, 88(20):205427, 2013.

[143] Chaoyu Chen, Zhuojin Xie, Ya Feng, Hemian Yi, Aiji Liang, Shaolong He, Daixiang Mou, Junfeng He, Yingying Peng, Xu Liu, et al. Tunable dirac fermion dynamics in topological insulators. Scientific reports, 3, 2013.

[144] Hugen Yan, Xuesong Li, Bhupesh Chandra, George Tulevski, Yanqing Wu, Marcus Freitag, Wenjuan Zhu, Phaedon Avouris, and Fengnian Xia. Tunable infrared plasmonic devices using graphene/insulator stacks. Nature nanotechnology, 7(5):330–334, 2012.

[145] Yu. O. Averkov, V. M. Yakovenko, V. A. Yampol'skii, and Franco Nori. Oblique surface josephson plasma waves in layered superconductors. Phys. Rev. B, 87:054505, Feb 2013.

[146] Eugene Hecht. Optics 4th edition. Optics, 4th Edition, Addison Wesley Longman Inc, 1998, 1, 1998.

[147] Mingda Li, Wenping Cui, Lijun Wu, Qingping Meng, Yimei Zhu, Yong Zhang, Weishu Liu, and Zhifeng Ren. Topological effect of surface plasmon excitation in gapped isotropic topological insulator nanowires. Canadian Journal of Physics, 0(0):1–8, 0.

[148] N. D. Mermin. Lindhard dielectric function in the relaxation-time approximation. Phys. Rev. B, 1:2362–2363, Mar 1970.

[149] Liang Fu and Charles L Kane. Probing neutral majorana fermion edge modes with charge transport. Physical review letters, 102(21):216403, 2009.